7-3-2014

A Study of Structural and Magnetic Properties of Superconducting FeTeO(x)/Non Superconducting FeTe Film System

Lahiru K. Narangammana
lahirukn@yahoo.com

A Study of Structural and Magnetic Properties of Superconducting $FeTeO_x$/Non superconducting FeTe Film System

Lahiru K Narangammana, Ph.D.

University of Connecticut, 2014

This work describes synthesis methods to optimize the quality and stability of $FeTeO_x$/FeTe thin films and characterization of the low temperature crystal structure and magnetic structure of both the superconducting $FeTeO_x$ and non-superconducting FeTe film system.

Iron based superconductors have reinvigorated studies of high temperature superconductivity since their discovery in 2008. The relationship between the magnetic and superconducting phases is believed to be a key to their physics but remains a puzzle in many ways. Fe chalcogenides or the 11 family of superconductors are the simplest among Fe-based compounds. FeTe, which is non-superconducting and magnetic, is considered the parent compound for this family. FeTe can be made superconducting by incorporating interstitial oxygen.

In this work, an extensive study has been done to explore the effect of growth parameters for the pulsed laser deposition technique on $FeTeO_x$ film growth. A new growth mode has been introduced to produce films with stable oxygen concentration and better crystalline quality.

High-resolution synchrotron x-ray diffraction technique was used to study the low temperature crystal structure of superconducting $FeTeO_x$ films. We found that superconducting $FeTeO_x$ undergoes a structural transition from tetragonal to monoclinic similar to the parent FeTe but no change could be detected in the crystal symmetry of $FeTeO_x$ in the superconducting state

compared to its normal state. An anomaly in the c-axis lattice parameter was observed at the vicinity of the superconducting transition, which we relate to a discontinuity in thermal expansion at T_c. Using the Ehrenfest relation and this discontinuity we predicted a large enhancement of T_c in strained $FeTeO_x$ films.

Low temperature neutron diffraction studies reveal that superconducting $FeTeO_x$ films order aniferromagnetically around 65 K similar to parent FeTe and suggest a suppression of magnetism upon entering the superconducting state. Both conventional and synchrotron Mossbauer spectroscopy techniques were used to determine local magnetic fields around Fe nucleus in superconducting $FeTeO_x$. Results indicate that magnetism sets in below 65 K in $FeTeO_x$ in agreement with neutron diffraction data. Conventional Mossbauer spectroscopy data suggests a reduction in hyperfine magnetic fields in the superconducting state compared to the normal state.

A Study of Structural and Magnetic Properties of Superconducting $FeTeO_x$/Non Superconducting FeTe Film System

Lahiru K. Narangammana

B.Sc. (Phys) Sp., University of Peradeniya, 2007

M.Sc., University of Connecticut, 2012

A Dissertation

Submitted in Partial Fulfillment of the

Requirements for the Degree of

Doctor of Philosophy

at the

University of Connecticut

2014

APPROVAL PAGE

Doctor of Philosophy Dissertation

A Study of Structural and Magnetic Properties of Superconducting $FeTeO_x$/Non Superconducting FeTe Film System

Presented by

Lahiru K. Narangammana, B.Sc. (Phys) Sp., M.Sc.

Major Advisor _____

Barrett O. Wells

Associate Advisor _____

Joseph I. Budnick

Associate Advisor _____

Boris Sinkovic

University of Connecticut

2014

Dedicated to my Dear Parents Appachchi and Amma,
and to my Loving Husband Lochana
for their unconditional love and support

Acknowledgement

I would like to convey my sincere appreciation to my family, advisers, other faculty members, collaborators, staff, lab mates and friends for the input, guidance and support they gave me to pursue this Ph.D. Without them, this work would not have been possible.

First I would like to thank my major adviser Dr. Barrett O. Wells for his support and patience over the past few years. He gave me freedom to choose experiments that I like. I would like to express my deepest gratitude to Dr. Joseph I. Budnick, who without his many hours of conversations, encouragement and deep involvement in my projects I would have never been able to complete my studies. Dr. Budnick's enduring enthusiasm in my work encouraged me to move forward with my projects. I am very thankful to Dr. Hines for his time and effort he provided me on my projects. Dr. Hines worked day and night to function SQUID so that we were able to get good data. His vast knowledge about magnetic experiments and electronics was very helpful with getting successful results in experiments. I would like to thank Dr. Boris Sinkovic for the very helpful conversations I had with him over the past few years. I would also like to thank Dr. Gayanath Fernando, Dr. Menka Jain and Dr. Jason Hancock for their support.

I would like to convey my gratitude to all the collaborators at Argonne national laboratory, Brookhaven national laboratory, Paul Sherrer Institut Switzerland and Oak Ridge national laboratory. My special thanks goes to the staff, lab mates and friends in UCONN physics department.

I would like to thank my parents, Appachchi and Amma for their unconditional love and support. Their faith towards me in all times encouraged me to come this far. Finally I would like to convey my special thanks to my husband, Lochana. I don't have enough words to convey my

gratitude to him. He has always been there for me in the good and bad times. Without his patience, unselfish support and encouragement I would have never succeeded in pursuing this Ph.D.

Table of Contents

List of Figures

List of Tables

1 Introduction

1.1 Superconductivity

A superconductor is characterized by two properties. One is the absence of steady state DC resistance below a temperature T_c, called superconducting transition temperature or critical temperature, and the other is the exclusion of magnetic fields up to a critical field below T_c. Heike Kamerlingh Onnes discovered superconductivity in 1911. In 1956 John Bardeen, Leon Neil Cooper, and John Robert Schrieffer (BCS) constructed a microscopic theory that can qualitatively predict most properties of elemental superconductors. According to BCS theory, by using the electron phonon interaction the estimated maximum superconducting transition temperature was around 30 K.[1] In 1986 J.G. Bednorz and K.A. Muller discovered that Barium doped $LaCuO_4$ shows superconductivity approximately below 35 K. Later, Mercury based cuprates with critical temperatures higher than 130 K were found. After the discovery of this new family of materials called high temperature superconductors, it is no longer clear whether BCS theory is satisfactory for all classes of superconductors. After more than 20 years since its discovery, the mechanism behind high temperature superconductivity is still not clear. Until 2008 there were only few other materials besides cuprates which have shown high superconducting transition temperatures. In 2008, a new family of superconductors, originally Fe-pnictides,[2] later Fe-chalcogenides[3] was discovered. These compounds showed superconducting transition temperatures above 50 K.[4] The presence of superconductivity in a compound based upon Fe, commonly associated with magnetism, suggests a novel mechanism for superconductivity. Hence studying this new family of high temperature superconductors will provide new insights into understanding the mechanism behind high temperature

superconductivity. The similarities and differences between cuprates and iron-based superconductors will be helpful in determining what factors are crucial for high temperature superconductors.

1.2 Iron-based superconductors vs Cuprate Superconductors

The differences and similarities between iron-based superconductors and cuptrates has been a major line of discussion. Both are characterized by a parent compound and upon doping the parent compound a superconductor can be created. The parent compounds of both families are non-superconducting and antiferromagnetic. Both are layered 2-D compounds where superconductivity occurs in a certain conducting plane, for cuprates in Cu-O plane and for iron-based compounds in Fe-As planes or Fe-Ch planes (Ch-Te,Se,S). One minor difference between the two is that As or Se/Te/S anions are located above and below the Fe layers for iron-based compounds and Cu and O ions are located in the same plane for cuprates. Another is the ability to substitute or dope into the active pairing layer in the Fe- based compounds. The parent compounds of cuprates are Mott insulators and doping involves adding electrons or holes as charge carriers to the Cu-O conducting plane. On the other hand the parent compounds of iron-based compounds are conductors, with five bands crossing the fermi level. To create a superconductor from these compounds several methods have been used and it is not clear what doping does to create a superconductor from the parent compound.[5–7] In both cuprates and iron-based compounds the detailed interplay between superconductivity and magnetism appears to be important for understanding the mechanism behind superconductivity. For cuprates there exists a unique phase diagram. As a function of doping a magnetic phase is observed in a lower doping level, a superconducting phase is observed at the optimal doping level and a pseudogap phase is observed at an intermediate level of doping.[8] In contrast, iron-based superconductors have

several different phase diagrams. As a function of doping at least three different types of transitions could be observed between magnetism and superconductivity. For example for $FeTe_{1-x}Se_x$ system as a function of doping first magnetism is completely destroyed and superconductivity emerges at a higher doping level.[9] This is similar to the phase diagram of cuprates. For the $LaO_{1-x}F_xFeAs$ system there is a sharp boundary between magnetic phase and superconducting phase and there does not exist any intermediate phase between the two.[10] For the 122 family, (different families of iron based superconductors will be discussed in next section) as a function of doping antiferromagnetism is suppressed and superconductivity emerges at a higher doping level. But at an intermediate doping level, for a considerable range of doping, superconductivity co-exists with magnetism.[11] The exact relationship between different cases is not currently clear. How the superconductivity and magnetism compete and interact with each other in this family of compounds is a question to be addressed.

1.3 Overview of Iron-based superconductors

The discovery of superconductivity in fluorine doped LaOFeAs at 26 K in 2008 by Hosono et al.[2] caused great excitement in the condensed matter physics community. Superconductivity and magnetism are typically ground states that compete with each other. Since iron is a ferromagnet, superconductivity of any material that contains iron is a great surprise. Later, by applying pressure the superconducting transition of $LaO_{1-x}F_xFeAs$ was increased to 43 K and by substituting rare earth elements for La in LaOFeAs the superconducting transition temperature could be doubled to 55 K.[4] Next another family of superconductors with FeAs layers was found but here the LaO layer was replaced by simple metals such as Ba,Sr or Ca.[12] These compounds were made superconducting by doping K or Na into Ba,Sr or Ca sites or by substituting an

element like Co into Fe sites. Subsequent work led to the discovery of another two types of compounds, LaFeAs[13] and the binary compound FeSe.[3]

After the discovery of these different type of compounds, iron based superconductors were charegorized into four major families depending on the chemical formula of its parent compound. The four major families are 1111 type ; ReFeAsO (Re = rare earth), 111 type ; AFeAs (A = alkali metal), 122 type $AeFe_2As_2$ (Ae = alkaline earths), and 11 type FeX (X = chalcogens).

At room temperature the crystal structure of the parent compounds of iron-based superconductors are tetragonal with space group P4/nmm. Fe and pnictide/chalcogen atoms are packed in edge sharing tetrahedra. The detailed crystal structure of each family is different. A schematic diagram of the crystal structure of each family is shown in figure 1-1.

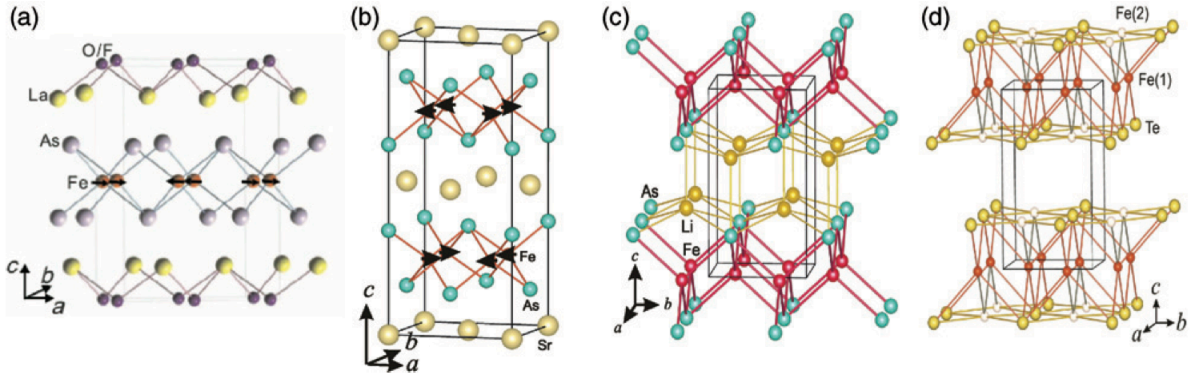

Figure 1-1 Crystal structures of (a) $LaO_{1-x}F_xFeAs$ (b) $SrFe_2As_2$ (c) LiFeAs (d) $Fe_{(1+x)}Te$ (adapted from ref. 7)

Irrespective of the structure type, all compounds contain Fe-As or Fe-Chalcogen layers. It is believed that FeAs or Fe-chalcogen layers play a key role in superconductivity. Unlike cuprates, an insulating layer or a charge reservoir is not a requirement in iron-based superconductors. The LnO (Ln; lanthenides) insulating layer, which provides charge carriers, is only present in the 1111 family. It is replaced by simple metals in the 122 family and completely absent in the 11 family. Another feature of these compounds is the ability to directly dope or

substitute into the FeAs/Fe-chalcogen active pairing layer. For example, superconductivity can be induced by doping Co into Fe in FeAs layers or by substituting Se into Te sites in FeTe layers.[14,15]

The parent compounds of 1111 and 122 family undergo a structural transition from tetragonal to orthorhombic associated with antiferromagnetic order.[10,11] For LaFeAsO the structural transition occurs around 155 K and the antiferromagnetic transition happens around 137 K.[16] For a majority of the compounds the magnetic transition follows the structural transition. Despite this, at least one theory assumes that the magnetic transition initiates the structural transition.[17] Upon doping, the magnetic phase is suppressed and a superconducting phase emerges at a higher doping level. In terms of structure, upon doping the orthorhombic symmetry which favors magnetism get suppressed and a tetragonal symmetry that favors superconductivity emerges. It is believed that upon doping, the ordered magnetism gets destabilized with only spin fluctuations remaining, and these spin fluctuations provide the medium for electron pairing.

For iron-based compounds as a function of doping the way superconductivity develops shows a complicated behavior and this behavior varies with each family. Even for the compounds that belong to the same family different phase diagrams can be observed. For example for $LaO_{1-x}F_xFeAs$ as a function of doping, a sharp boundary could be seen between the superconducting phase and the magnetic phase. The electronic phase diagram of $LaO_{1-x}F_xFeAs$ is shown in figure 1-2.[10] On the other hand for $SmFeAsO_{1-x}F_x$ as a function of doping there exists a region where superconductivity coexists with magnetism as shown in figure 1-3.[18] The 122 family of superconductors show, a similar behavior to that of $SmFeAsO_{1-x}F_x$. The electronic phase diagram of $BaFe_2As_2$ doped with several elements is shown in figure 1-4. For a considerable amount of doping both superconducting and magnetic phases are present in

$BaFe_2As_2$.[5] The electronic phase diagram of 11 family of compounds is different from either of these. The electronic phase diagram of $FeTe_{1-x}Se_x$ is shown in figure 1-5. As Se is substituted into Te sites first the antiferromagnetic phase is completely suppressed and bulk superconductivity emerges at a higher doping level.[9] This is similar to the phase diagram of cuprates. How these phase diagrams relate to each other is not currently clear. One idea is that there is a very subtle difference between the free energy of superconducting phase and the magnetic phase and depending on some physical parameters these compounds can be easily tuned into a superconducting state or to a magnetic state. Understanding how the magnetism and superconductivity interact and compete with is other is significant.

In cuprates, to induce superconductivity, parent compounds are doped to add electrons or holes as charge carriers to the Cu-O plane. In iron-based compounds, in addition to charge doping isovalent doping has been used to induce superconductivity. For example in the case of $BaFe_2As_{2-x}P_x$, As is substituted by isovalent P and in case of $FeTe_{1-x}Se_x$, Te is substituted by Se. Isovalent doping doesn't involve any change in the charge balance of the active pairing layer but changes the lattice spacing and details of the crystal structure. Pressure also plays a significant role in enhancing the superconductivity of iron-based compounds. It is assumed that pressure has a similar effect as isovalent doping and may change parameters such as the Fe-anion bond length or Fe-anion angle. There are several physical parameters that can be used to turn these compounds into a superconducting phase from the magnetic parent phase. It is not exactly clear what physical parameter is crucial and which is not when turning a parent compound to a superconductor. It is believed that simple charge doping it not the only factor that is critical for superconductivity but structure also plays a significant role.

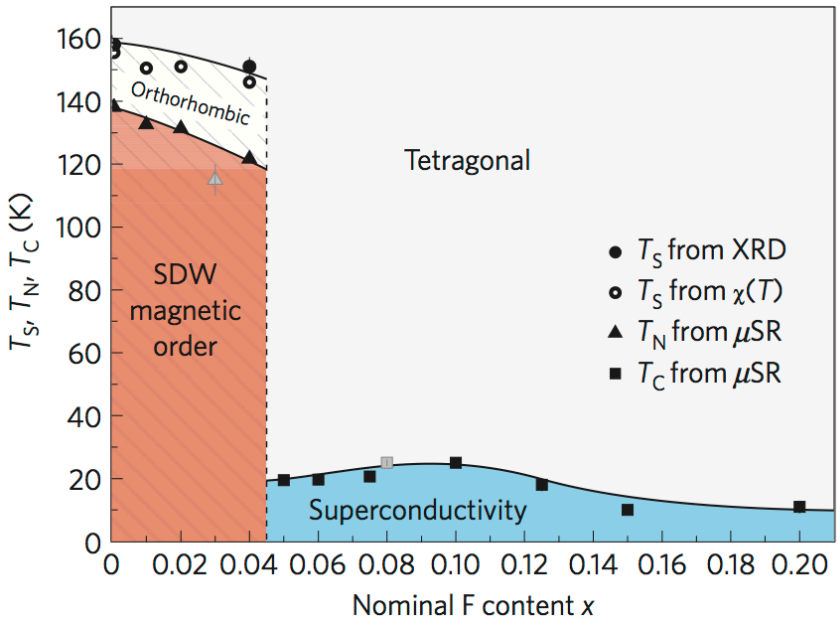

Figure 1-2 Electronic phase diagram of $LaO_{1-x}F_xFeAs$. The superconducting and magnetic transition temperatures as a function of doping are shown (adapted from ref. 10)

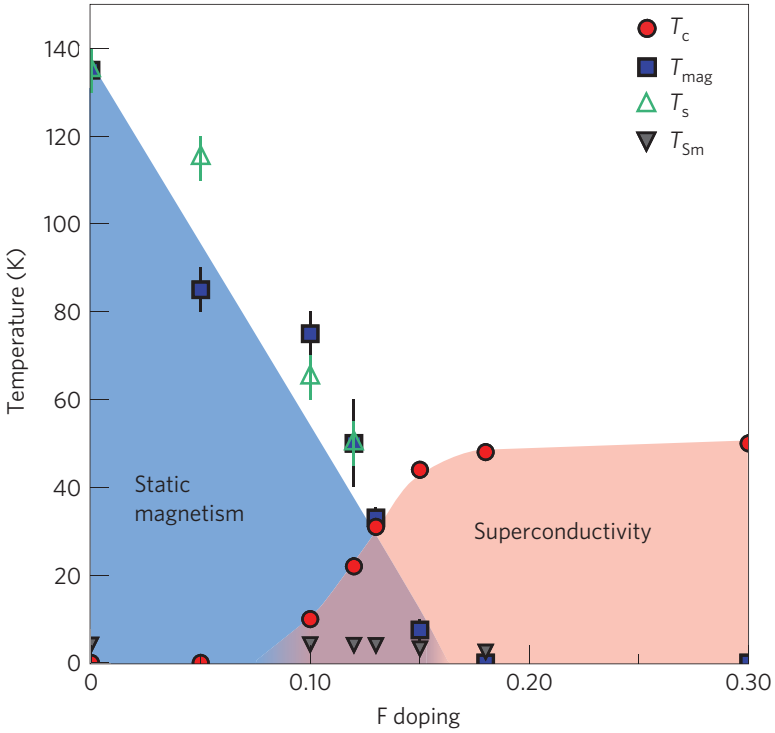

Figure 1-3 Electronic phase diagram of $SmO_{1-x}F_xFeAs$. The superconducting and magnetic transition temperatures as a function of doping are shown (adapted from ref. 18).

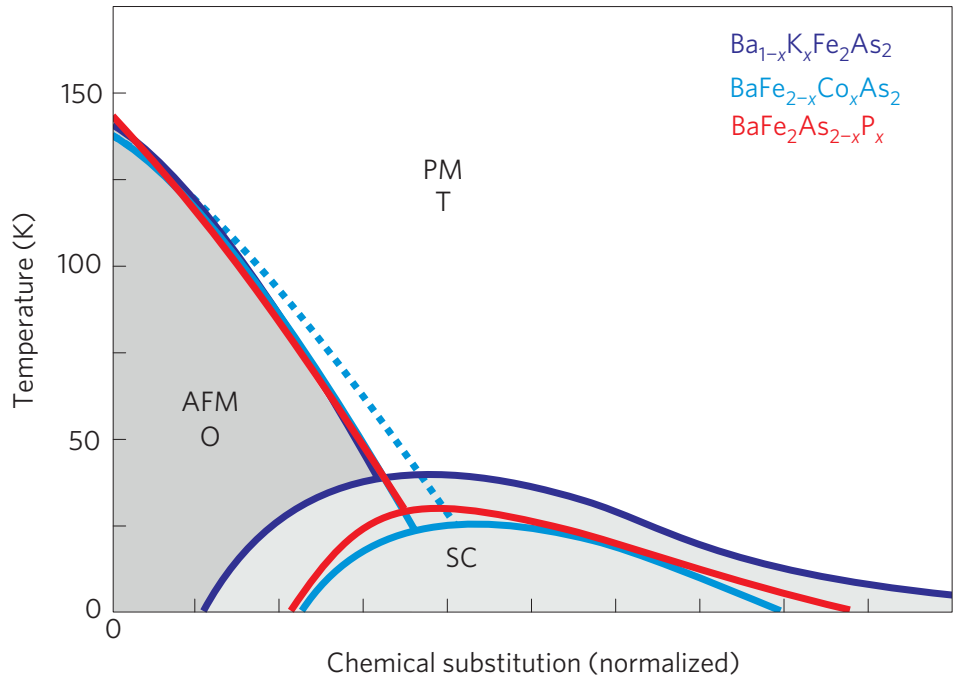

Figure 1-4 Electronic phase diagram of $Ba_{1-x}K_xFe_2As_2$, $BaFe_{2-x}Co_xAs_2$, and $BaFe_2As_{2-x}P_x$. The superconducting and magnetic transition temperatures as a function of doping are shown. The dashed line shows the orthorhombic to tetragonal structural transition (adapted from ref. 5).

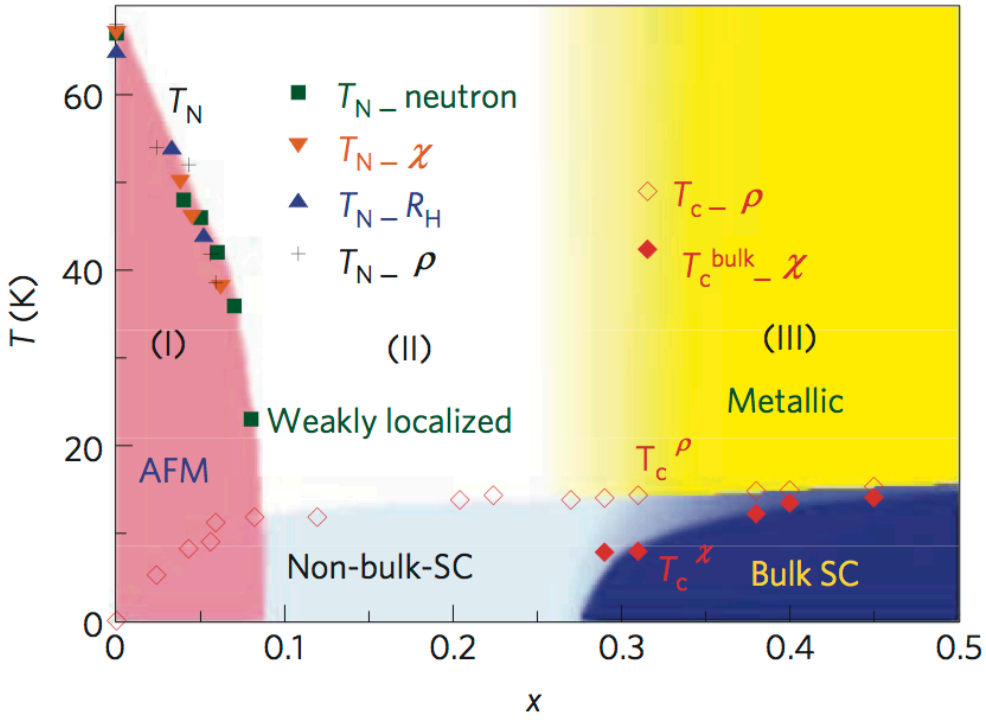

Figure 1-5 Electronic phase diagram of $FeTe_{1-x}Se_x$. The superconducting and magnetic transition temperatures as a function of Se doping are shown (adapted from ref. 9).

1.4 Why study 11 family ?

Recently much attention has been given to the 11 family of iron-based superconductors for several reasons. Two major doping mechanisms have been used in iron chalcogenide system i.e. isovalent doping and charge doping to make a superconductor from the parent compound FeTe. These two doping mechanisms can also be mixed. This will allow one to explore the full two dimensional phase diagram and determine which physical parameters favor superconductivity and which favors magnetism. A second advantage of the Fe chalcogenide system is the chemical simplicity of the compounds. Fe chalcogenides consist of only Fe-anion planes. Since only a few non-active elements are present in the system it may be easier to interpret the results. Also, the Fe chalcogenide system has the potential for application in magnetic storage systems due to the low anisotropy, high critical current density and high critical field of these compounds compared to other high temperature superconductors.[19] Therefore, studying the underlying physics of this system is important.

FeTe is considered the parent compound for the Fe-chalcogenide family. FeTe can be made superconducting via isovalent substitution of Se or S into Te sites[15,20] or by charge doping via incorporating with oxygen.[21,22] The other end member of this family, FeSe, is superconducting with transition temperature 8 K.[3] At room temperature FeTe and FeSe show the tetragonal PbO type crystal structure with space group P4/nmm. A schematic diagram of the crystal structure of FeSe is shown in figure 1-6. Fe and Se atoms are packed in an edge sharing tetrahedra. FeTe undergoes a structural transition around 65 K that is associated with antiferromagnetic order. Depending on the excess iron in the structure, the structural transition will be from tetragonal to monoclinic for a low excess iron concentration and will be from tetragonal to orthorhombic for a higher excess iron concentration.[23,24] Upon doping of Se into Te

sites the antiferromagnetism and the monoclinic/orthorombic phase is suppressed and superconductivity emerges in the tetragonal phase with an optimal doping level of $FeTe_{0.5}Se_{0.5}$.[9] FeSe undergoes a structural transition from tetragonal to orthorhombic around 90 K. Unlike in other parent compounds of iron based superconductors this structural transition is not associated with any antiferromagnetic order. Hence it is believed that orthorhombic symmetry favors superconductivity in FeSe.[25,26]

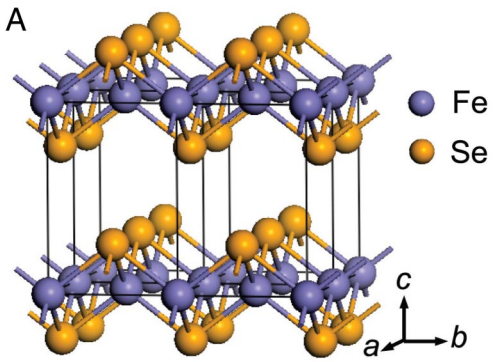

Figure 1-6 Schematic diagram of the room temperature crystal structure of FeSe (adapted from ref. 3)

Among iron-based compounds the most dramatic pressure effect has been shown in FeSe where superconducting transition temperature was increased to 37 K by application of hydrostatic pressure.[27–29] Superconductivity could be also enhanced in $FeTe_{0.5}Se_{0.5}$ system by pressure.[30,31] These pressure effects indicate the high sensitivity of superconductivity to the local structure in iron-based compounds. There has been discussion in the community about the dependence of superconducting transition temperature on Fe-anion height.[7] A study done on FeSe shows there is a direct correlation between the anion height and superconducting transition temperature.[32] Figure 1-7 shows the dependence of pressure on Se height and transition temperature. The pressure effect on the whole $FeTe_{1-x}Se_x$ system shows similar behavior: as the anion height or anion-Fe-anion bond angle decreases the superconducting transition temperature increases. This behavior is analogous to the close relationship between the superconductivity and

the c-axis lattice parameter in iron-based compounds. Fe-anion height can be used as a tuning parameter to create compounds with high superconducting transition temperatures.

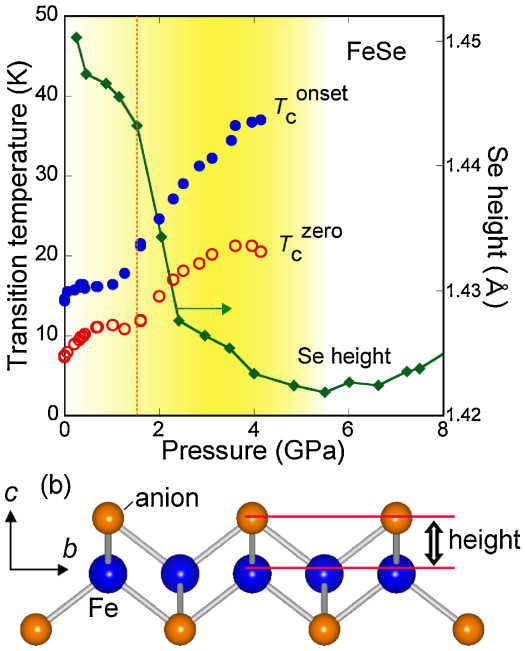

Figure 1-7 (a) Superconducting transition temperature and Se height as a function of pressure for FeSe. (b) Schematic diagram of anion height (adapted from ref. 32)

1.5 $FeTeO_x$/FeTe thin film system

The isovalent doped $FeTe_{1-x}Se_x$ system has been studied extensively in terms of its crystal and magnetic structures, phase diagram, electronic structure etc. A clear understanding about the superconducting properties of charge doped $FeTeO_x$ system is still lacking. Superconductivity in oxygen incorporated FeTe was independently discovered by Yuefeng Nie at the university of Connecticut.[21] At the same time another two groups reported superconductivity in FeTe; Si claims due to incorporation of oxygen[22] and Han claims due to tensile strain.[33] More information about the way superconductivity was discovered in FeTe will be found in Yuefeng Nie's thesis.

Originally, FeTe films were grown in vacuum using pulsed laser deposition and oxygen was incorporated into these films by low temperature oxygen annealing. The films had a porous structure and it was possible to remove oxygen by low temperature anneals in vacuum. Hence superconductivity was reversible. It was difficult to perform experiments on these porous films, which were not stable. For example, an effort was made to determine the low temperature crystal structure of these films using x-rays but the oxygen was driven from the films as they absorbed energy from x-rays in vacuum. Hence producing smooth continuous dense superconducting $FeTeO_x$ films with stable oxygen concentration was critical to investigate the properties of $FeTeO_x$.

At room temperature the x-ray diffraction measurements done perpendicular to the film surface using laboratory sources showed that there is no significant difference between the crystal structure of superconducting $FeTeO_x$ and that of non-superconducting FeTe.[21] The x-ray absorption spectroscopy (XAS) measurements done at room temperature reveal that the valence of iron changes to 3+ in superconducting state.[21,34] A detailed description of XAS measurement can be found in Yuefeng Nie's and Don Telesca's theses.

1.6 Scope of this thesis

Investigating the effect of growth parameters in pulsed laser deposition technique to produce optimal quality superconducting $FeTeO_x$ films and studying crystal and magnetic structure of superconducting $FeTeO_x$/non-superconducting FeTe film system will be the scope of this thesis.

Producing FeTe films with good crystalline quality is critical for experiments like x-ray diffraction and neutron diffraction. Hence an extensive study has been done to explore the effect

of growth parameters of pulsed laser deposition on superconducting $FeTeO_x$ film growth. This work is in described in chapter 2 of this thesis.

A more careful study has been done using the high intensive x-rays at Brookhaven national laboratory to determine the low temperature crystal structure of superconducting $FeTeO_x$. The results of this experiment revealed that at room temperature the crystal structure of superconducting $FeTeO_x$ is tetragonal similar to parent FeTe and there is a small change in lattice constants of $FeTeO_x$ compared to non-superconducting FeTe.[21] The temperature evolution of the c-axis lattice parameter indicates that $FeTeO_x$ undergoes a structural transition from tetragonal to a different structural phase but this low temperature phase was still unknown prior to this work. There was an indication of a small decrease in c-axis of the superconducting film in the vicinity of superconducting transition temperature but the result was not conclusive. After improving the quality of superconducting $FeTeO_x$ films as described in chapter 2 a complete investigation of the low temperature crystal structure of superconducting $FeTeO_x$ was carried out in Brookhaven laboratory using high resolution x-rays. A detailed description of this experiment is given in chapter 3.

For iron-based superconductors, trying to understand the relationship between magnetic and superconducting phases will be the key to understand the underlying physics behind these compounds. Hence it is interesting to explore the temperature dependent magnetic properties of $FeTeO_x$ films. The temperature dependent resistivity of superconducting $FeTeO_x$ shows a peak around 65 K similar to parent FeTe. In parent FeTe, this peak is associated with the structural and magnetic transition. Existence of this peak in superconducting films indicates that the magnetism can co-exits with superconductivity in $FeTeO_x$. In general antiferromagnetism is difficult to study in films because the total magnetic moment is too small to detect the subtle

changes associated with antiferromagnetism. With some difficulties, two approaches, neutron diffraction and Mossbauer spectroscopy, have been used to observe the antiferromagnetic order in $FeTeO_x$/FeTe thin film system. Chapter 4 describes the low temperature magnetic structure of superconducting $FeTeO_x$. Mossabuer spectroscopy has been used as a local probe to investigate the local magnetic moments associated with Fe ions at low temperature in this system. Neutron diffraction has been used as a probe to observe the average ordered magnetic structure of this system. The details of the magnetic phase observed in $FeTeO_x$ obtained using the above techniques will be discussed in chapter 4. The data obtained using neutron diffraction together with two different types of Mossbauer spectroscopy techniques, the conventional method and synchrotron Mossbauer spectroscopy method, will be discussed.

Based on the results reported in above chapters the conclusions arrived on superconducting $FeTeO_x$ film system and the suggestions for future work will be given in chapter 5.

The low temperature crystal structure and magnetic structure of superconducting $FeTeO_x$ will be helpful in understanding which properties are changed and which are not when creating the robust superconductor $FeTeO_x$ from parent FeTe.

2 The effect of Growth Conditions on superconductivity of $FeTeO_x$ films

2.1 Pulsed Laser Deposition

Pulsed laser deposition is a thin film deposition technique. Laser radiation with high power is focused to strike on a target inside a vacuum chamber to ablate material from the target that needed to be deposited. Due to the strong interaction between the laser and the target surface many energetic species including atoms, molecules, electrons, ions, and clusters are ejected into the growth atmosphere in the form of a plasma plume. Then these species are deposited on a substrate that is maintained at the appropriate temperature. The main advantage of this technique is the stoichiometry transfer between the target and substrate. This allows PLD to be used as a system to grow complex systems like high temperature superconductors, piezoelectric and ferroelectric materials. Since the energy source is located outside the chamber ultra-high vacuum or a gas like oxygen or Argon can be used during growth. By depositing a film in an inert atmosphere like Argon the kinetic energy of the deposited particles can be varied. This makes it possible to tune the properties of a film like stress, texture and reflectivity. Another advantage of PLD is the fast evaporation rate or growth rate of the thin film relative to other deposition techniques like Molecular Beam Epitaxy (MBE). In addition the ablation rate can be controlled in a relatively easy way by controlling the parameters in the energy source such as the repetition rate of the laser and the power of the laser. This technique has been used to grow various kinds of materials such as high temperature superconductors, semiconductors, oxides, nitrides, carbides, and advanced materials like ferroelectrics, and materials with super lattice structures. [35–37]

There is a strong correlation between the ablation conditions and the quality of the films. So far there has been a lot of literature on how to grow high quality cuprate high temperature superconductor thin films[38] but the literature about iron-based superconducting thin films,

particularly about iron chalcogenide films, is rare. Therefore the effect of pulsed laser deposition growth parameters on iron chalcogenide thin film growth has been extensively studied. The scope of this chapter is to describe the effect of growth conditions on $FeTeO_x$ film growth. At the end of the chapter the optimized growth parameters identified to grow a high quality $FeTeO_x$ film with stable oxygen concentration are given. The techniques described here can be used not only for $FeTeO_x$/FeTe thin film system but can be extended to any other iron chalcogenide thin film system such as FeSe , $FeTe_{(1-x)}Se_x$, or $FeTe_{(1-x)}S_x$ as well as any likely chalcogenide film.

2.2 Previous film growth and problems

Previously FeTe films were grown in vacuum and oxygen was incorporated by post growth annealing at a low temperature, 100 °C, in order to make superconducting $FeTeO_x$ films. Superconductivity induced by this method was reversible where oxygen could be easily added or removed through low temperature anneals.[21] This process was possible due to the islanding open micro-structure of the films. However these films caused trouble in performing some experiments with high intensity photons at low temperature in vacuum. For example an effort has been made to study the crystal structure of these films at low temperature using x-rays, but due to the open structure, when the film absorbed energy from the x-rays, oxygen was driven out. Hence superconductivity was destroyed, making it difficult to obtain good results from this experiment. In order to perform such experiments successfully, producing dense continuous films with a stable oxygen concentration and better surface morphology was critical. Therefore a careful study was carried out to understand the effect of growth parameters of pulsed laser deposition on thin film growth.

Besides the stable oxygen concentration, better crystalline quality of films is also important particularly when performing experiments like neutron diffraction and x-ray diffraction. In thin

film growth the crystal structure of the film highly depends on the in-plane lattice mismatch between substrate and film. When the lattice mismatch is small, films are grown with better crystalline quality. Hence the effect of substrate on $FeTeO_x$ film growth was studied. So far $FeTeO_x$ with bulk superconducting properties has been only produced in thin film form. A recent report claims superconductivity in $FeTeO_x$ single crystals, but superconductivity could be only achieved in a surface layer.[39] Although an effort has been made to induce superconductivity in bulk single crystalline FeTe at university of Connecticut it was not successful. Hence superconducting properties of this material could be only studied using films. Therefore the study of the growth methods that can produce optimal quality FeTeOx films was critical.

2.3 Thin film growth at UCONN

The $FeTeO_x$ films were grown in a 9" diameter spherical chamber that was designed at University of Connecticut particularly to grow chalcogenide films. At room temperature the chamber can go to a base vacuum of $9.6x10^{-9}$ Torr. A turbo pump and a rough pump have been used to pump down the chamber to this level. Two inlets have been used to transfer nitrogen and oxygen gas into the growth chamber. A needle valve has been used to control the oxygen pressure of the chamber very accurately during growth. The substrates in the chamber can be heated up to 600 ˚C but the maximum temperature is limited by the position of the target holder. When the target is at a minimum distance from the substrate, i.e. 40 mm, the heat provided to the substrate transfers to the target making the target holder very hot. As a result target falls off from the holder. Hence maximum growth temperature has to be limited to 450 ˚C when minimum target to substrate distance is used. In the future, by building up a cooling stage the target can be protected from the radiation coming from heater. Since the target holder can be adjusted easily the target to substrate distance during growth can be adjusted from 65 mm to 40 mm. The laser

pulse cannot be focused on the target surface beyond this range due to the arrangement inside the chamber and the optics used to focus the laser beam.

An excimer laser with 248 nm wavelength has been used to ablate the target. The repetition rate of the laser can be varied from 1 Hz to 8 Hz. The energy density of the laser can be varied between 63 mJ /cm^2 and 138 mJ/cm^2. Several substrates with different lattice constants have been used to grow FeTe thin films, including, $SrTiO_3$ (cubic, a = 3.905 Å), MgO (cubic, a = 4.216 Å), CaF_2 (cubic, a = 5.462 Å), $LaAlO_3$ (=LAO, Rhombohedral, a = 3.79 Å c = 13.11 Å), $(LaAlO_3)_{0.3}(Sr_2AlTaO_6)_{0.7}$ (=LSAT, tetragonal, a = 3.868 Å c = 5.46 Å) and $SrLaAlO_4$ (=SLAO, tetragonal a = 3.754 Å, c = 12.63 Å).

At the beginning, the targets used to grow FeTe films were made at university of Connecticut by mixing Fe and Te powder at the correct stoichiometry and pressing them in a dye using hydrostatic pressure. By this method any type of chalcogenide target, $FeTe_{1-x}Se_x$ (x = 0 to 1) or $FeTe_{1-x}S_x$ (x = 0 to 1) could be made by mixing the necessary powders at the correct ratio. Later a dense polycrystalline conglomerate made using solid state sintering method at Brookhaven laboratory was used as the target. The targets were received from Dr. Genda Gu.

2.4 Outline

In this chapter first the different growth parameters tested in order to grow films with stable oxygen concentration will be described. To grow films with better crystalline quality films were grown on various substrates. The effect of substrate on film growth will be explained next. The films were grown in various partial oxygen pressures to change the amount of oxygen in film. The aim was to check whether superconducting transition temperature could be increased by changing the amount of oxygen doped into the film. The third section of this chapter

describes the effect of partial oxygen pressure during growth on superconducting properties of $FeTeO_x$ films.

2.5 Different Growth Modes

Depending on some pulsed laser deposition growth parameters, particularly the target to substrate distance, the laser power and the target used, the recipes used to grow films were categorized into two growth modes. They are growth mode 1 and growth mode 2 which will be discussed in detail later. Films grown by these growth modes were characterized using several techniques. Orientation of the film with respect to the substrate along the c-axis was checked by a two-circle x-ray diffractometer with a Cu K_α source. In plane orientation of the film with respect to substrate was characterized by 3-circle diffractometer with an area detector with the Cu K_α source. Temperature dependent resistance of the films was measured by a Quantum Design Magnetic Property Measurement System using a four-probe technique. Scanning electron microscope was used to examine the surface morphology and continuity of films. The relative chemical compositions of Fe and Te in films were measured by energy dispersive x rays. Thicknesses of films were measured by optical interferometer.

2.5.1 Growth Mode 1

In first growth mode a porous unreacted home-made target was used. Iron and tellurium powder was mixed together and high pressure was applied on the mixed powder to make a pellet. Due to the low melting point of tellurium, the pellet could not be heated at high temperature in order to make chemical reactions between iron and tellurium. The evaporation rate of tellurium is much higher than that of iron. Therefore, compared to iron a higher composition of tellurium (1:1.4) was used in the target in order to maintain a 1:1 Fe:Te ratio in the films. During growth the substrate was kept at 380 °C. In order to optimize the film quality high growth

temperatures,e.g. 800 °C have been used in general in pulsed laser deposition. Again due to the high evaporation rate of Tellurium, the growth temperature couldn't be increased to a higher value. The effect of growth temperature on thin film growth will be discussed in detail later.

In growth mode 1, substrates were kept at a distance of 65 mm from the target. The growth chamber was pumped down to obtain a vacuum of approximately $4x10^{-8}$ Torr at room temperature. At growth temperature FeTe films were grown in a vacuum better than $2*10^{-7}$ Torr using a laser power of 220 mJ with 4 Hz repetition rate. After deposition, films were cooled to room temperature at a rate of 4 °C/min. As grown FeTe thin films were then annealed at 100 °C in low oxygen partial pressure of 100 mTorr in order to make superconducting $FeTeO_x$ films. Films were grown on (0 0 1) oriented $SrTiO_3$ substrate.

Figures 2-1 to 2-4 show the characteristics of films grown on $SrTiO_3$ substrate using these growth parameters. An X-ray diffraction pattern taken perpendicular to the film surface is shown in figure 2-1. Only (00L) Bragg peaks corresponding to the FeTe tetragonal phase is seen besides the (00L) peaks corresponding to $SrTiO_3$ cubic phase, indicating the epitaxial growth of the film along the c-axis. Figure 2-2 shows the scanning electron microscope image of an FeTe film grown on a $SrTiO_3$ substrate. The lighter, square-like patterns represent the film and the black background represents the substrate indicating that the FeTe films had an island-like structure. Due to this discontinuous open micro-structure, oxygen could be easily added or removed from FeTe films. Interestingly the islands were grown in square-like pattern. The temperature dependent resistance of as grown FeTe film is shown in figure 2-3. This is similar to that of bulk FeTe.[15,20] The broad peak observed around 65 K can be an effect due to the structural transition associated with antiferromagnetic order as seen in bulk. In order to make superconducting $FeTeO_x$, the as grown FeTe films were annealed in 100 °C in 100 mTorr oxygen

pressure. After annealing in oxygen, a superconducting transition can be observed around 12.5 K but the zero resistance state could not be achieved even at 2.0 K. The temperature dependent resistance of a superconducting $FeTeO_x$ thin film is shown in figure 2-4. The anomaly around 65 K indicates that the structural and magnetic transition can still exist in superconducting $FeTeO_x$.

From above growth mode strong c-axis textured films with superconducting transitions could be created. Due to the open islanding micro-structure of the films oxygen could be easily added or removed making the oxygen concentration of the films very unstable. It was difficult to perform experiments like x-ray diffraction in low temperature in vacuum using these films. Due to the open islanding structure oxygen was driven out absorbing the energy from photons destroying superconductivity. In order to perform such experiments successfully producing dense continuous films with a stable oxygen concentration and better surface morphology was critical. Therefore we carefully studied growth parameters to optimize the quality of films.

To check the effect of growth temperature on film growth, FeTe films were grown at several growth temperatures and high repetition rates of laser pulse were used at higher temperatures. Figure 2-5 to 2-7 show the x-ray diffraction patterns taken perpendicular to the film surface on FeTe films grown at different temperatures.

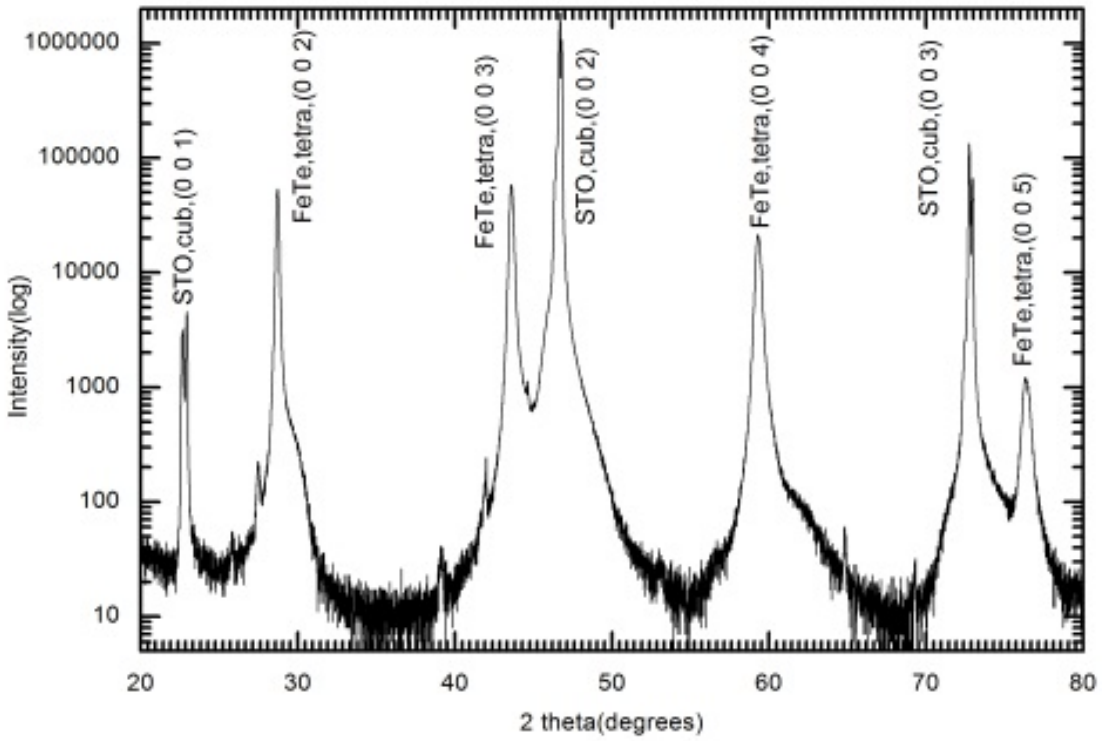

Figure 2-1 X-ray diffraction pattern perpendicular to the ab-plane of a FeTe film grown on $SrTiO_3$ substrate using growth mode 1.

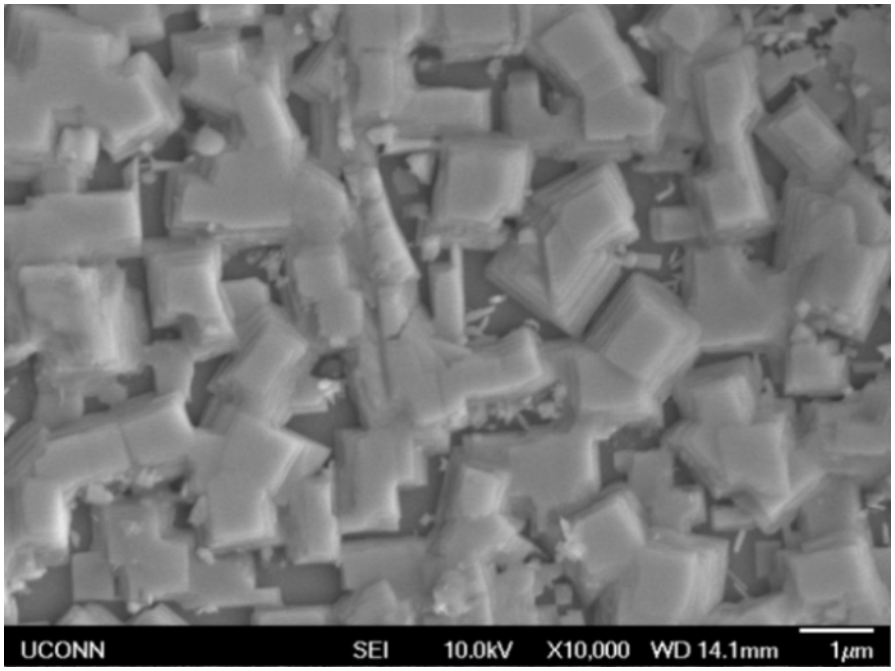

Figure 2-2 Scanning electron microscope image of a FeTe film grown on $SrTiO_3$ substrate using growth mode 1.

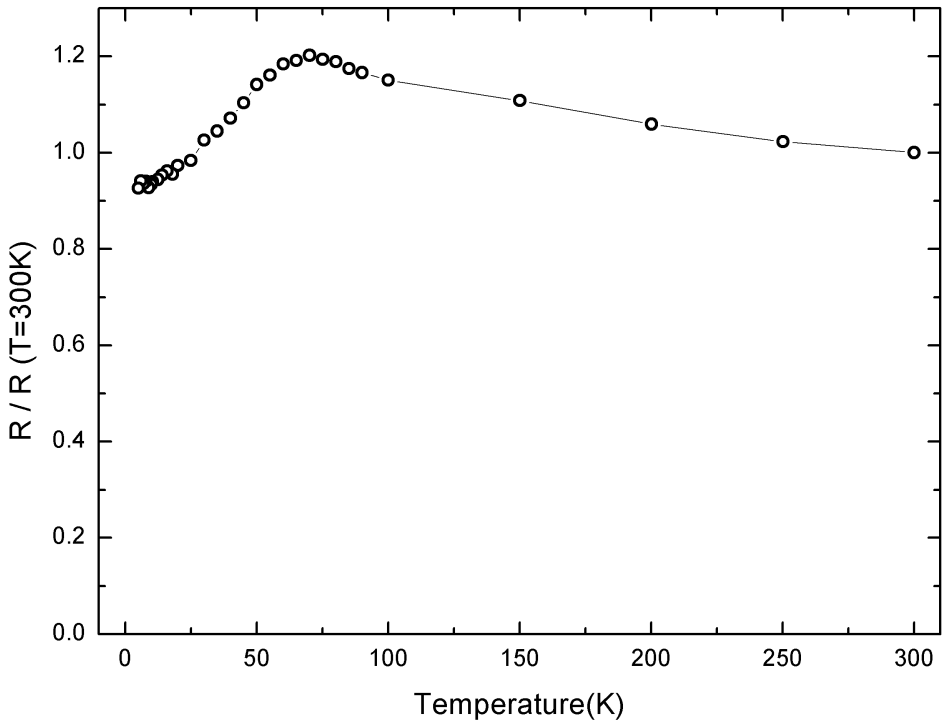

Figure 2-3 Temperature dependent resistance of a FeTe film grown in vacuum on a $SrTiO_3$ substrate using growth mode1. Resistance is normalized to the value at 300 K.

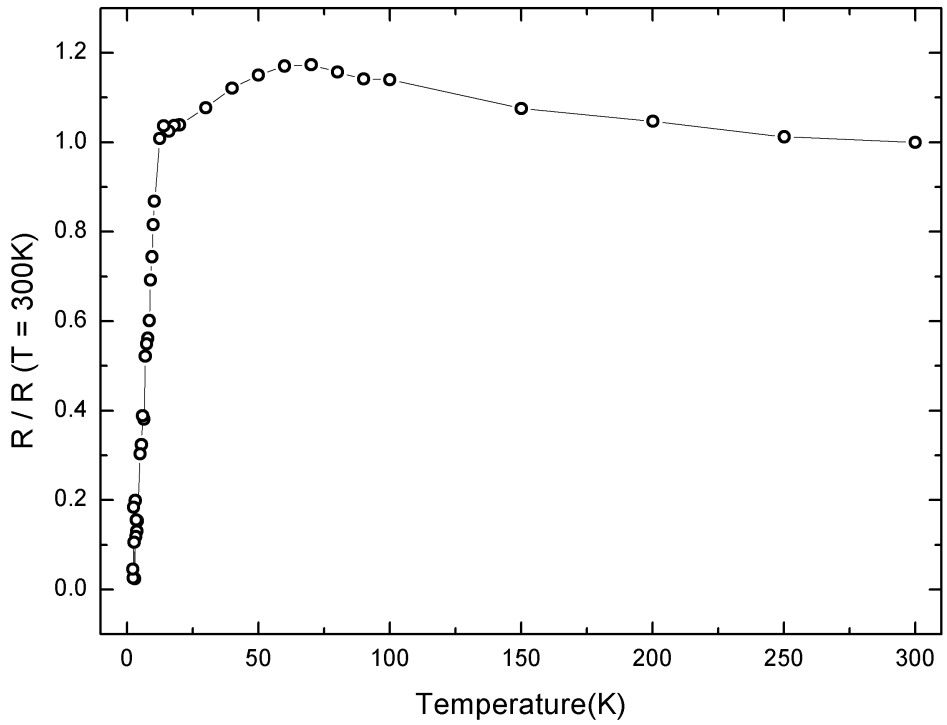

Figure 2-4 Temperature dependent resistance of a FeTe film grown using growth mode 1 and annealed in oxygen. Resistance is normalized to the value at 300 K.

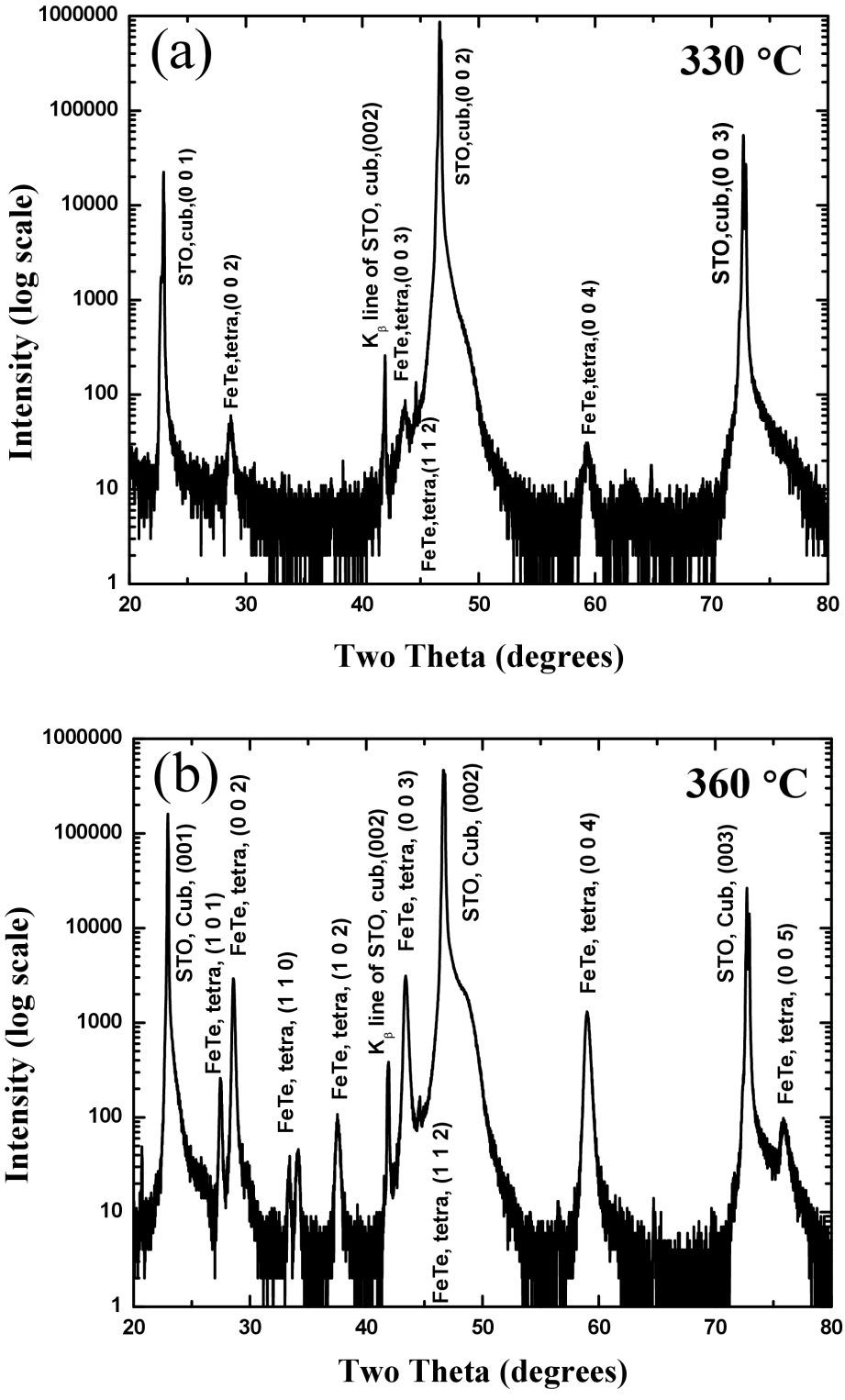

Figure 2-5 X-ray diffraction pattern taken perpendicular to the film surface for a superconducting $FeTeO_x$ film on $SrTiO_3$ substrate grown at (a) 330 ˚C (b) 360 ˚C.

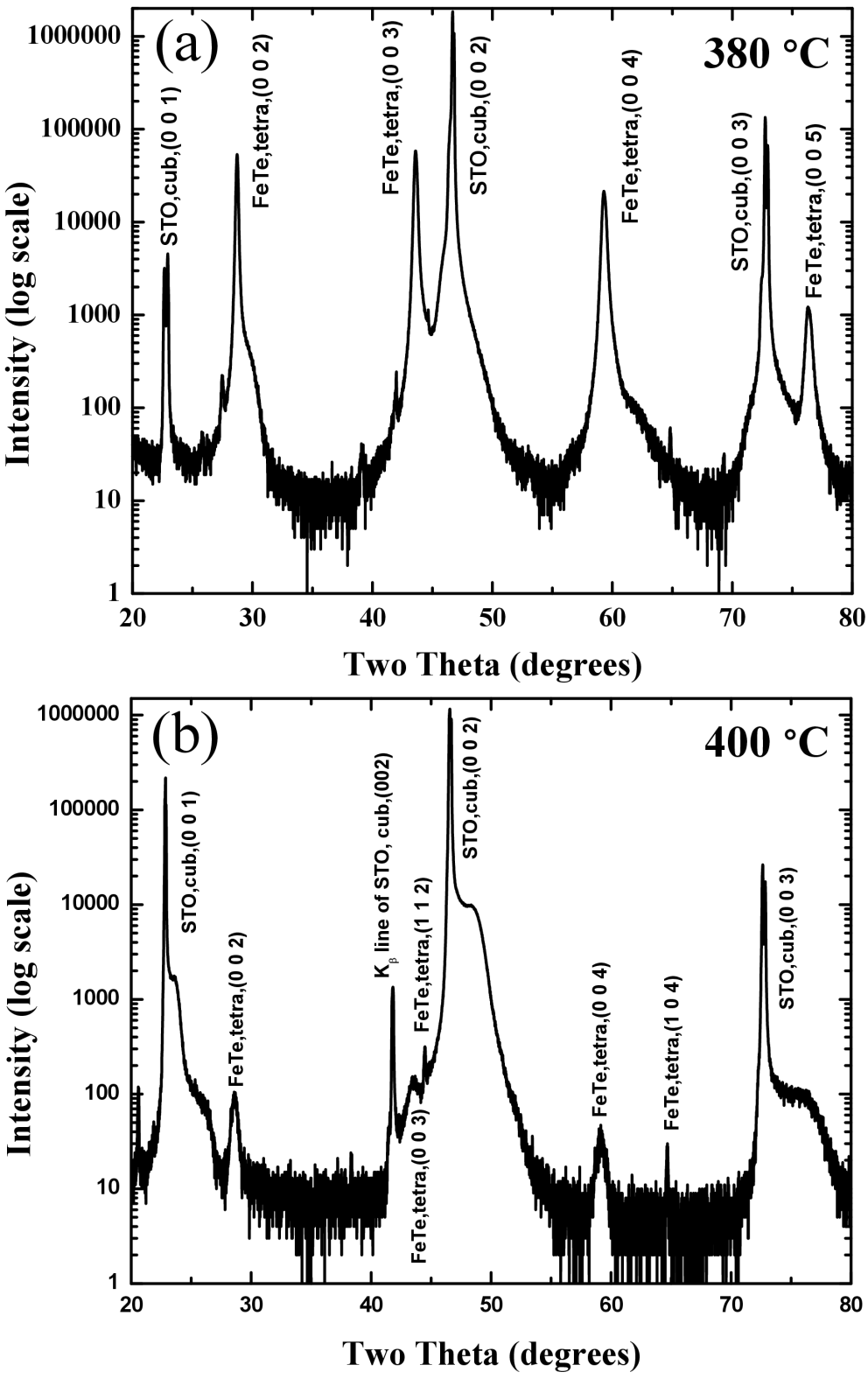

Figure 2-6 X-ray diffraction pattern taken perpendicular to the film surface for a superconducting $FeTeO_x$ film on $SrTiO_3$ substrate grown at (a) 380 ˚C (b) 400 ˚C.

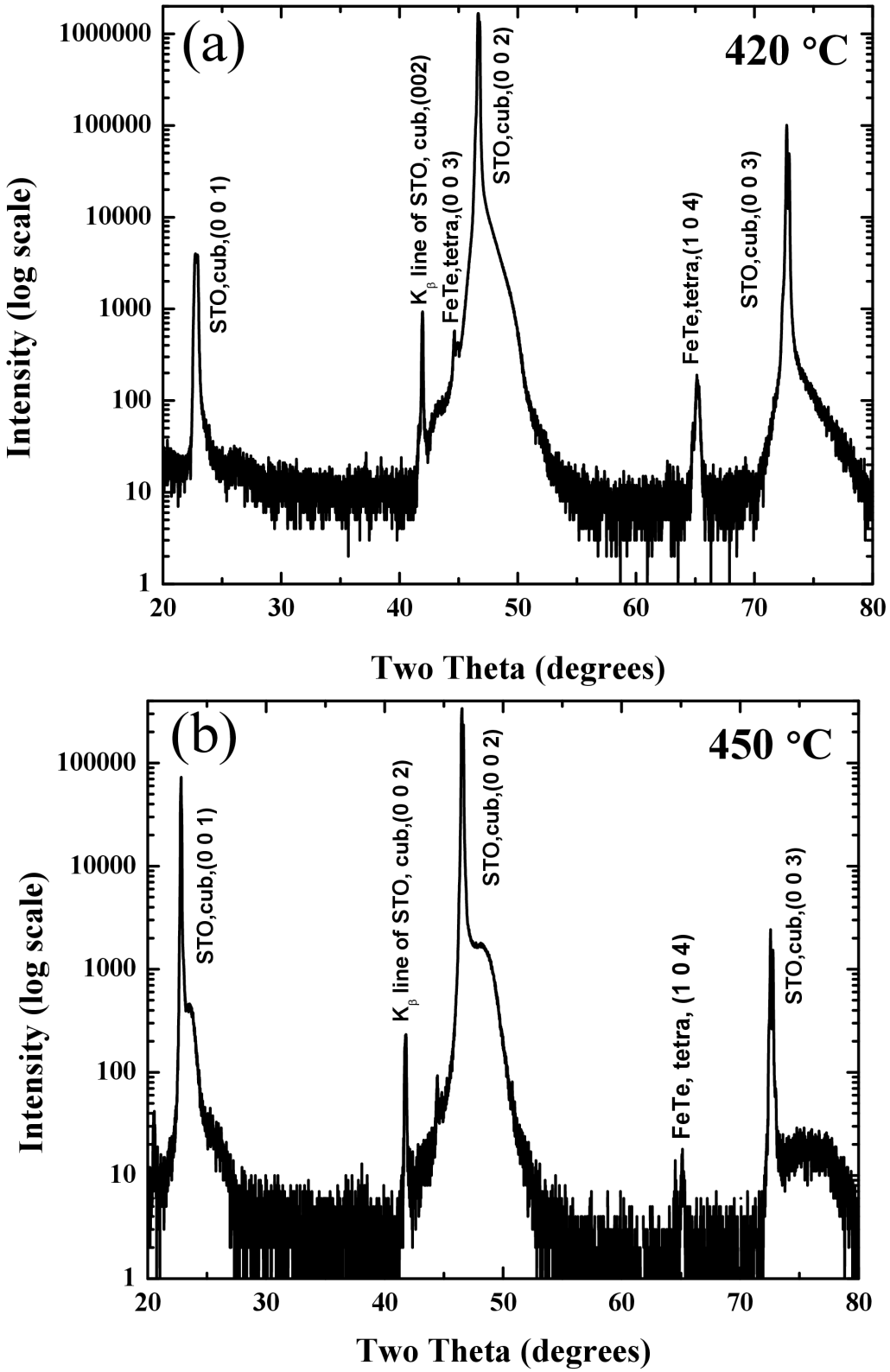

Figure 2-7 X-ray diffraction pattern taken perpendicular to the film surface for a superconducting $FeTeO_x$ film on $SrTiO_3$ substrate grown at (a) 420 ˚C (b) 450 ˚C.

At very low and very high temperatures like 330 ˚C and above 400 ˚C FeTe film peaks were less intense indicating that at those temperatures films didn't grow well on the substrate. At higher temperatures the reason can be the evaporation of Tellurium from the film. In order to keep an appropriate tellurium concentration, the growth temperature cannot be increased beyond 380 ºC. At a temperature, 360 ˚C fairly intense film peaks could be observed but also a lot of off-axis peaks could be seen indicating the mis-alignment of the film with the substrate. At 380 ˚C intense film peaks only in the (00L) direction could be observed indicating the epitaxial growth of FeTe films along c-axis. Hence it appears that growth temperature is a critical parameter for iron chalcogenide film growth and the optimal temperature to grow FeTe films is 380 ˚C.

Another important parameter in thin film growth is the cooling rate. Once films are grown at a certain temperature the rate at which film cools down to room temperature highly affects the crystal structure of film. So far a slow cooling rate, 4 ˚C per minute has been used to cool down the as grown films to room temperature. The x-ray diffraction pattern taken perpendicular to the film surface of a FeTe film grown at 380 ˚C and cooled down using a higher cooling rate, 20 ˚C per minute, is shown in figure 2-8. Compared to figure 2-6 (a) off-axis FeTe film peaks could be observed in this figure indicating the poor c-axis texture. Hence we concluded that a slower cooling rate is critical to maintain a good crystalline structure in the film.

To recap in growth mode 1 FeTe films were grown using a home-made unreacted porous target. A low laser power of 0.110 mJ/cm^2 was used to grow the films. The target to substrate distance was maintained at 65 mm. The films showed islanding structure. First FeTe films were grown in vacuum and later annealed in oxygen to make superconducting $FeTeO_x$ films. Oxygen could be easily removed by low temperature anneals in vacuum making the superconductivity

reversible. The superconducting transition could be observed in these films around 13 K but the zero resistance state could not be observed even at 2 K.

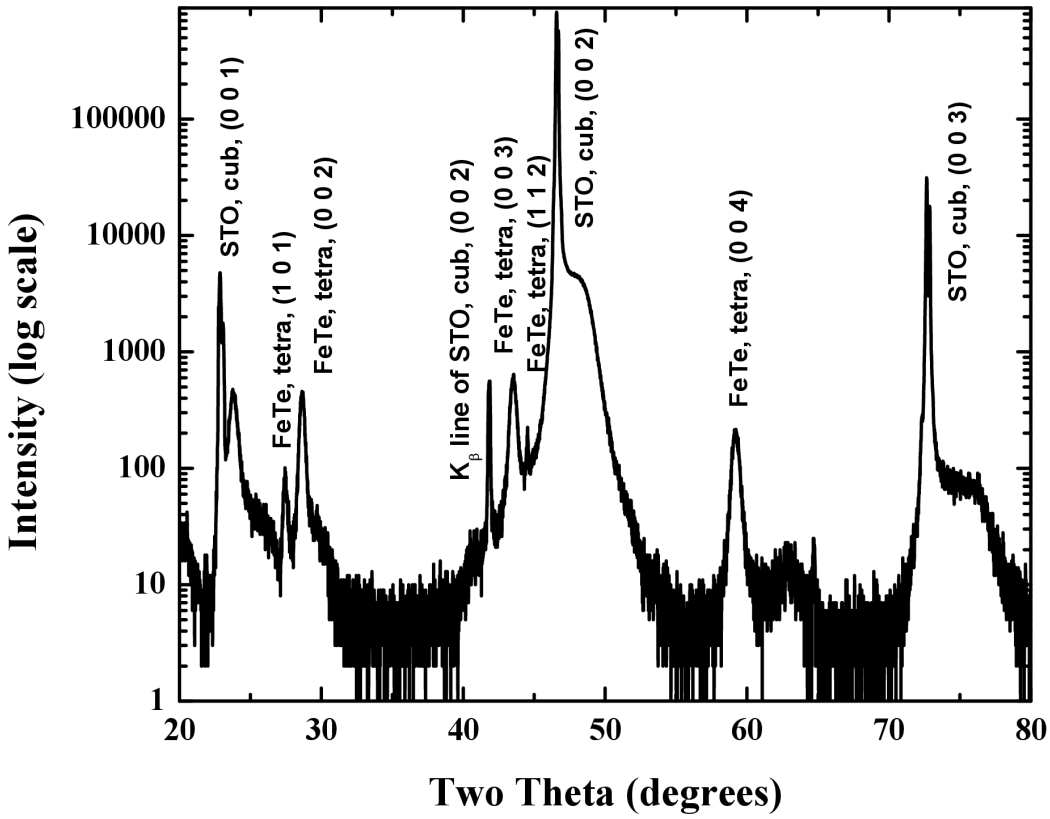

Figure 2-8 X-ray diffraction pattern taken perpendicular to the film surface of a FeTe film on $SrTiO_3$ substrate grown at 380 ˚C and cooled down in 20 ˚C per minute rate.

2.5.2 Growth Mode 2

In order to keep a stable oxygen concentration in films instead of post growth annealing, oxygen was incorporated during growth using the growth parameters described above in growth mode 1. In this growth mode, whenever a new gas was introduced during growth, very thin films were acheived. Due to the large target to substrate distance and the low laser power the atomic species which emit from the target may not have enough kinetic energy to reach the substrate when scattering off gas molecules. Therefore in order to overcome this problem the films were

grown in oxygen atmosphere using a shorter target to substrate distance compared to the previous one and higher laser power to provide higher kinetic energy to the atomic species. Using above growth parameters thick $FeTeO_x$ films could be grown even in oxygen atmosphere. As the target to substrate distance was decreased and the laser power was increased, the better quality films could be grown. Hence 40 mm, the minimum target to substrate distance possible in the growth chamber and the highest laser power possible, 0.138 mJ/cm^2 were used as the optimal growth parameters. To avoid the islanding growth and to improve the micro-structure of FeTe films, instead of using a porous unreacted Fe/Te target a dense, polycrystalline conglomerate with composition $Fe_{1.04}Te$ was used. Using this target, dense continuous film with better surface morphology could be produced. Using above growth parameters FeTe films could be grown in vacuum better than $2x10^{-7}$Torr as well as $FeTeO_x$ films in low oxygen partial pressures in the range from $9.0x10^{-7}$ Torr to $1.0x10^{-4}$ Torr. By changing the growth time the film thickness could be varied from 50 nm to 600 nm.

Figure 2-9 to 2-12 describes the characteristics of a $FeTeO_x$ film grown by growth mode 2. X-ray diffraction pattern taken perpendicular to the film surface of a 600 nm thick $FeTeO_x$ film grown on $SrTiO_3$ is shown in figure 3-9. FeTe (00L) peaks with high intensity indicate the epitaxial growth of film along c-axis. Figure 3-10 shows scanning electron microscope image taken on the same film. The film is dense, continuous and smooth and doesn't show any islanding growth like in figure 3-2. The surface morphology of this film is much better compared to that of the films grown using growth mode 1.

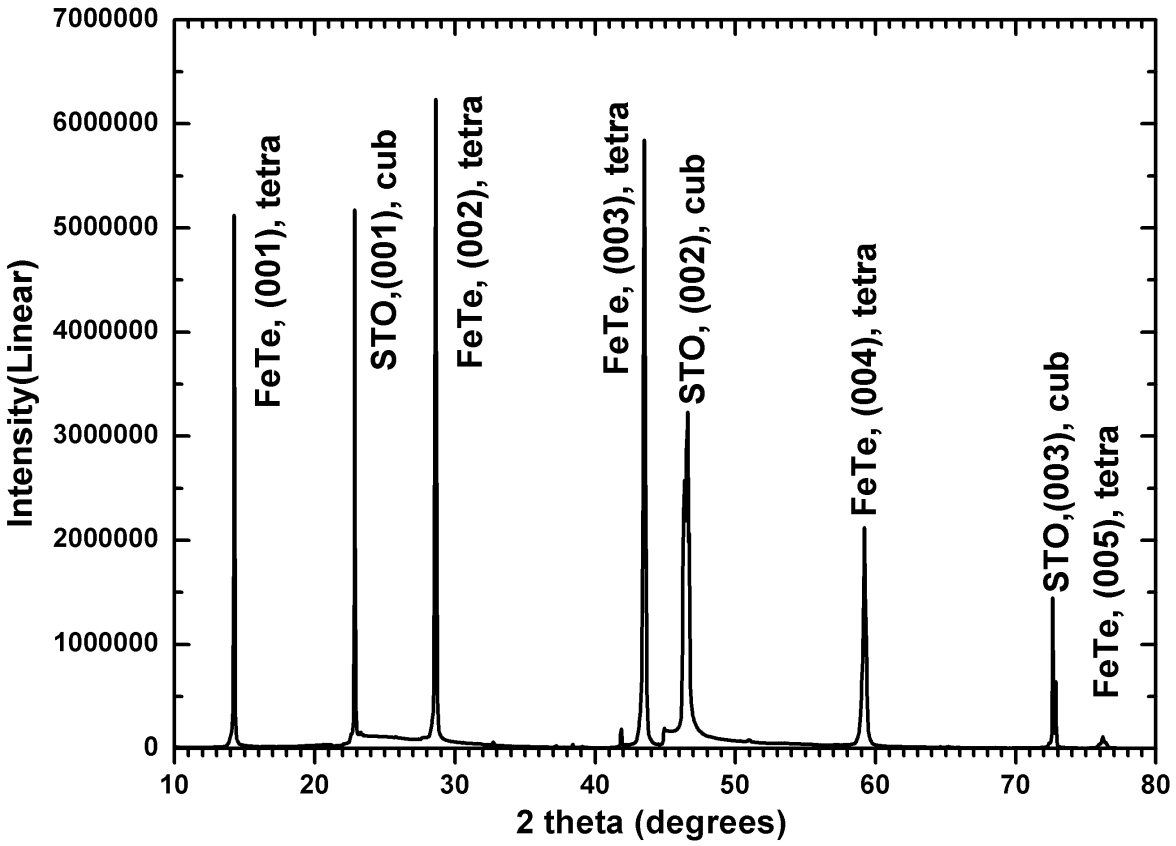

Figure 2-9 X-ray diffraction pattern taken perpendicular to the film surface of a $FeTeO_x$ film grown on $SrTiO_3$ substrate by growth mode 2.

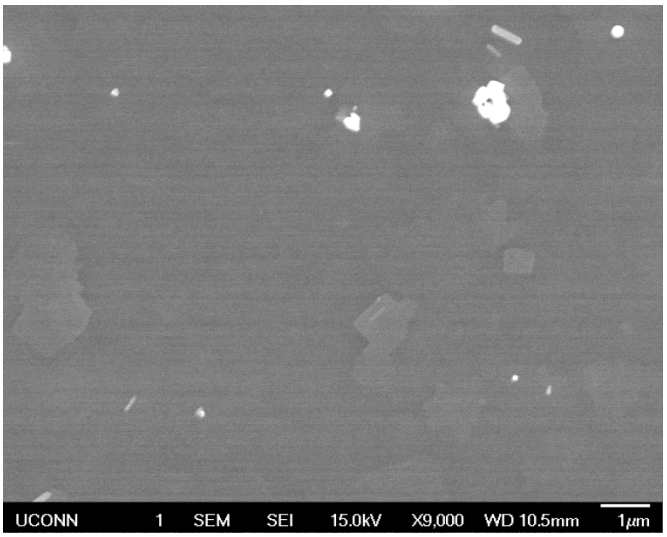

Figure 2-10 Scanning electron microscope image of a $FeTeO_x$ film grown on a $SrTiO_3$ substrate using growth mode 2.

Figure 2-11 shows the temperature dependent resistivity of the films grown using the optimized approach but different oxygen treatments. First FeTe films were grown in vacuum using growth mode 2. The curve with black circles in figure 2-11 represents the temperature dependent resistivity of a FeTe film grown in vacuum. This film shows a similar resistivity curve to the bulk. Compared to figure 2-3 a narrower peak could be observed around 65 K indicating better quality of film. Non-superconducting FeTe films grown by growth mode 2 were annealed in oxygen at 100 ℃ and 100 mTorr to check whether they can be made superconducting after growth. The curve with blue circles in figure 2-11 represent the temperature dependent resistivity of a post growth annealed film. A superconducting transition could be observed but it was hard to make the film superconducting by post growth oxygen annealing. Due to the closed dense structure of these films it was hard to incorporate oxygen into films after growth. Therefore the only way to make these films superconducting is by introducing oxygen during growth. $FeTeO_x$ films grown on $SrTiO_3$ substrate at oxygen partial pressure of $4.2*10^{-6}$ Torr showed a superconducting transition at 12.5 K approaching zero resistance state at 8 K. The temperature dependent resistance of a film grown in oxygen is shown in figure 2-11 by red circles. $FeTeO_x$ films by growth mode 2 showed much better superconducting properties compared to the films grown by growth mode 1 where zero resistance state couldn't be observed even at 2 K as shown in figure 2-3.

To test the stability of films grown by growth mode 2 a superconducting $FeTeO_x$ film was annealed in vacuum at 100 ˚C for 30min. A comparison of the temperature dependent resistance of FeTe film grown in oxygen atmosphere and the same film annealed in vacuum at 100 ˚C for 30 minutes is shown in figure 2-12. After the vacuum anneal, superconducting properties could be still seen in the film though there was a decrease in temperature of zero

resistance state. In growth mode 1, oxygen could be easily moved in and out from the film at 100 ˚C. But for dense smooth films grown using growth mode 2 it was difficult to move oxygen in or out. Therefore these films with stable oxygen concentration will be good candidates to perform experiments at low temperature in vacuum.

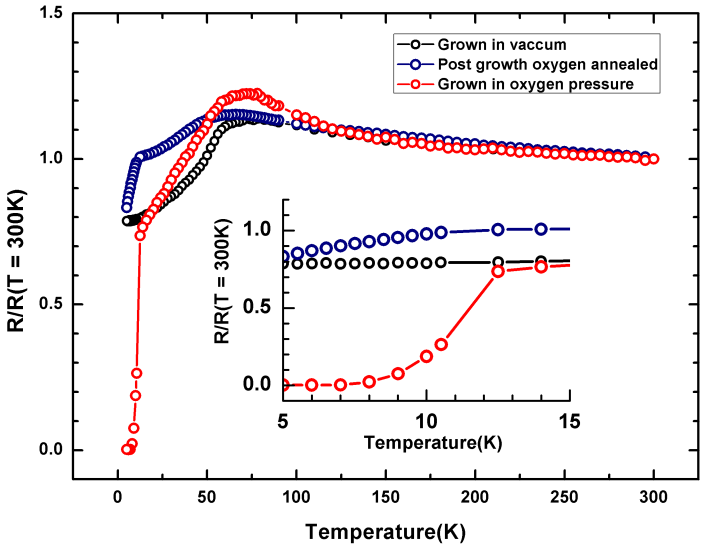

Figure 2-11 Comparison of temperature dependent resistance of films grown on $SrTiO_3$ substrate using growth mode 2 under three conditions. Resistance is normalized to the value at 300 K.

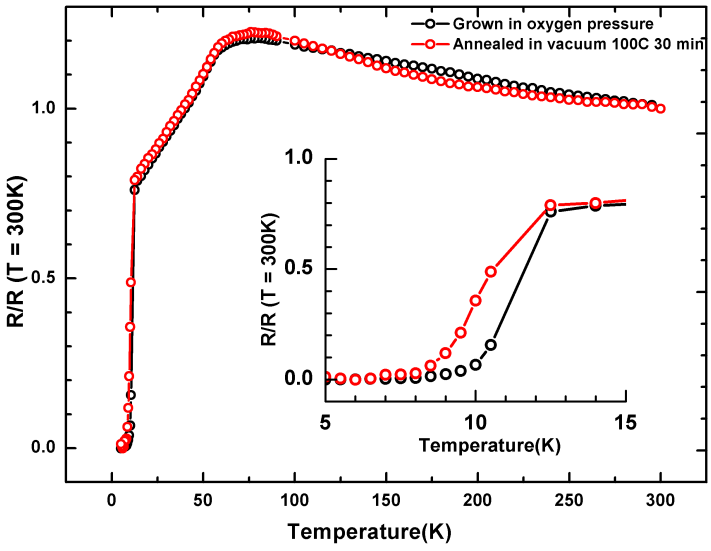

Figure 2-12 Comparison of temperature dependent resistance of a FeTe film grown in oxygen atmosphere and the same film annealed in vacuum at 100 ˚C for 30 min.

Films grown by growth mode 2 show a big improvement in epitaxy, surface morphology, superconducting properties and stability compared to the films grown by growth mode 1. In growth mode 2, by using a higher laser power more kinetic energy was provided to the atomic species emitted from the target. By using a small target to substrate distance the path the emitted particles needed to travel to reach the substrate was minimized. A dense target was helpful in growing a uniform dense film. The changes described above are the major reasons behind the improvement.

We compared the low temperature crystal structure of superconducting $FeTeO_x$ with non-superconducting bulk single crystals using the higher resolution x-ray diffraction technique in Brookhaven national laboratory. A detailed description of this experiment will be given in chapter 3 of this thesis. Some results obtained from this experiment were very helpful in verifying the fact that thick $FeTeO_x$ films were grown well aligned along the c-axis of the substrate and are free from strain effects of the substrate. The temperature evolution of the c-axis lattice parameter for a superconducting $FeTeO_x$ film and a non-superconducting single crystal FeTe bulk sample for the temperature range 20 K to 120 K is shown in figure 2-13. The c-axis lattice parameter of the film behaves very similarly to that of bulk FeTe. A decrease in the c-axis observed around 65 K indicates that the structural transition from tetragonal to monoclinic may still exist in superconducting $FeTeO_x$ films similar to bulk FeTe. This is evidence that $FeTeO_x$ films undergo a structural transition that is independent from the substrate. It appears that $FeTeO_x$ were grown well on the substrate while keeping the properties of bulk FeTe. Anyway the change in the c-axis of the film is not sharp compared to that of single crystalline bulk samples indicating the crystalline quality of films is not good as of single crystals.

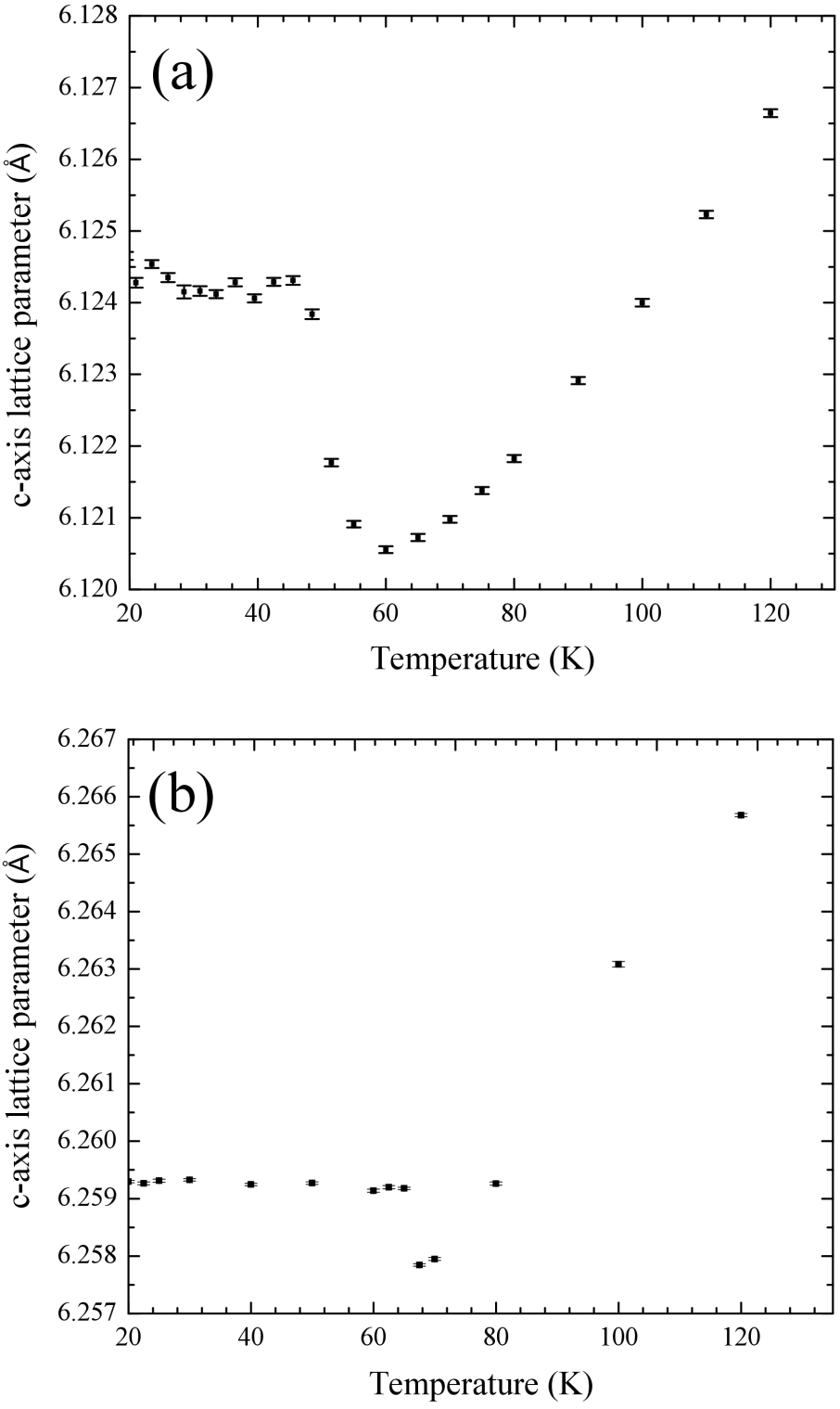

Figure 2-13 Temperature evolution of c-axis lattice parameter (a) for superconducting $FeTeO_x$ film grown on $SrTiO_3$ substrate (b) for FeTe single crystal bulk sample.

2.6 Effect of Substrate on $FeTeO_x$ film growth

2.6.1 Crystal Orientation of the films

So far FeTe films were grown only on $SrTiO_3$ substrate. In order to perform experiments like x-ray diffraction and neutron diffraction, films with better crystalline quality are required. Therefore in addition to c axis texture the overall crystal structure of FeTe thin film grown on $SrTiO_3$ substrate was tested by 3-circle x-ray diffractometer with an area detector. The beam dispersion images obtained from area detector for a FeTe thin film grown on $SrTiO_3$ substrate are shown in figure 2-14. The horizontal direction shows the dispersion in two-theta and vertical direction shows the dispersion in chi. As shown in figure 2-14 (a), for (003) $FeTeO_x$ peak only a small dispersion in two-theta and chi directions can be seen indicating the better c-axis texture of the film. This is consistent with the x-ray diffraction pattern taken perpendicular to the film surface of a $FeTeO_x$ grown on $SrTiO_3$ substrate as shown in figure 2-9. As shown in figure 2-14 (b) and 3-14 (c) (1 0 4) and (1 1 5) peaks of $FeTeO_x$ grown on $SrTiO_3$ show a much larger dispersion along chi direction indicating the poor in-plane mosaic of the films. Hence improving the in-plane orientation of the film with respect to the substrate is important.

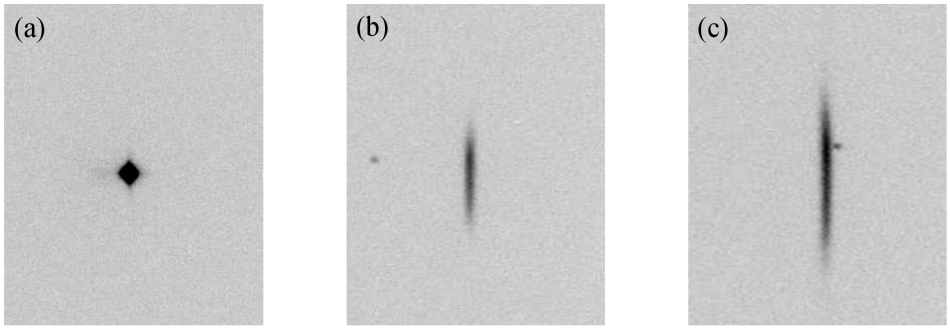

Figure 2-14 Beam dispersion images of the area detector of the 3-circle x-ray diffractometer obtained for Bragg reflections of a $FeTeO_x$ film grown on $SrTiO_3$ substrate. The horizontal direction shows the dispersion in two-theta and vertical direction shows the dispersion in chi (a) (0 0 3) Bragg reflection (b) (1 0 4) Bragg reflection (c) (1 1 5) Bragg reflection.

In thin film growth the crystal structure of the film highly depends on the in-plane lattice mismatch between substrate and film. It is believed that when the lattice mismatch is small, films are grown with better crystalline quality. For $SrTiO_3$ with the in-plane lattice constant of 3.905 Å, the lattice mismatch between $FeTeO_x$ film and substrate is 2.04 %. In order to improve the in-plane orientation of the film with substrate $FeTeO_x$ films were grown on various substrates with different in-plane lattice constants. The in-plane lattice constant of each substrate used and the lattice mismatch between substrate and film are given in the table 3-1 below.

Substrate	Room temperature crystal structure	In-plane lattice constant (Å)	Out of plane lattice constant (Å)	In-plane lattice mismatch between FeTe and substrate (%)
$SrTiO_3$	cubic	3.905	3.905	2.04
MgO	cubic	4.216	4.216	11.23
$LaAlO_3$ (LAO)	rhombohedral	3.79	13.11	1.35
$(LaAlO_3)(Sr_2AlTaO_6)_{0.7}$ (LSAT)	tetragonal	3.868	5.46	0.95
$SrLaAlO_4$	tetragonal	3.754	12.63	2.42
CaF_2	cubic	5.462	5.462	48.03

Table 2-1 In-plane lattice mismatch between substrate and film used to grow FeTe thin films. In plane lattice constant of FeTe is 3.836 Å.

First the alignment of $FeTeO_x$ films along c-axis on various substrates was tested. Figures 2-15 through 2-20 show the x-ray diffraction pattern taken perpendicular to the film surface of $FeTeO_x$ films grown on above substrates. The x-ray diffraction data shown on figures, 2-5 through 3-8 was taken using a point detector. By the time of this experiment there had been a change in the x-ray diffracrometer used to measure x-ray diffraction pattern of films. Instead of a point detector, a line detector had been used. Hence additional x-ray diffraction peaks and asymmetric background could be observed in figures 2-15 through 2-20 compared to figures 2-5 through 2-8. Some of these peaks cannot be recognized as film peaks or substrate peaks. To

distinguish these additional x-ray diffraction peaks from film peaks a comparison between a x-ray diffraction pattern of a $FeTeO_x$ film on a known substrate and a x-ray diffraction pattern of a blank substrate was done. The black solid line represents the film with substrate and the red solid line represents the blank substrate. When the red line is subtracted from black line the resulting pattern contains only $FeTeO_x$ film peaks. As seen in figures 2-15 through 2-20, the intense (0 0 L) $FeTeO_x$ film peaks that appear in the x-ray diffraction patterns taken on films of each substrate indicate the good alignment of film along c-axis with respect to each substrate. There are additional peaks, which cannot be recognized as film peaks, or substrate peaks. These extra peaks appear to be from a contamination of the Cu anode. The line detector leads to an asymmetric background in the x-ray diffraction pattern.

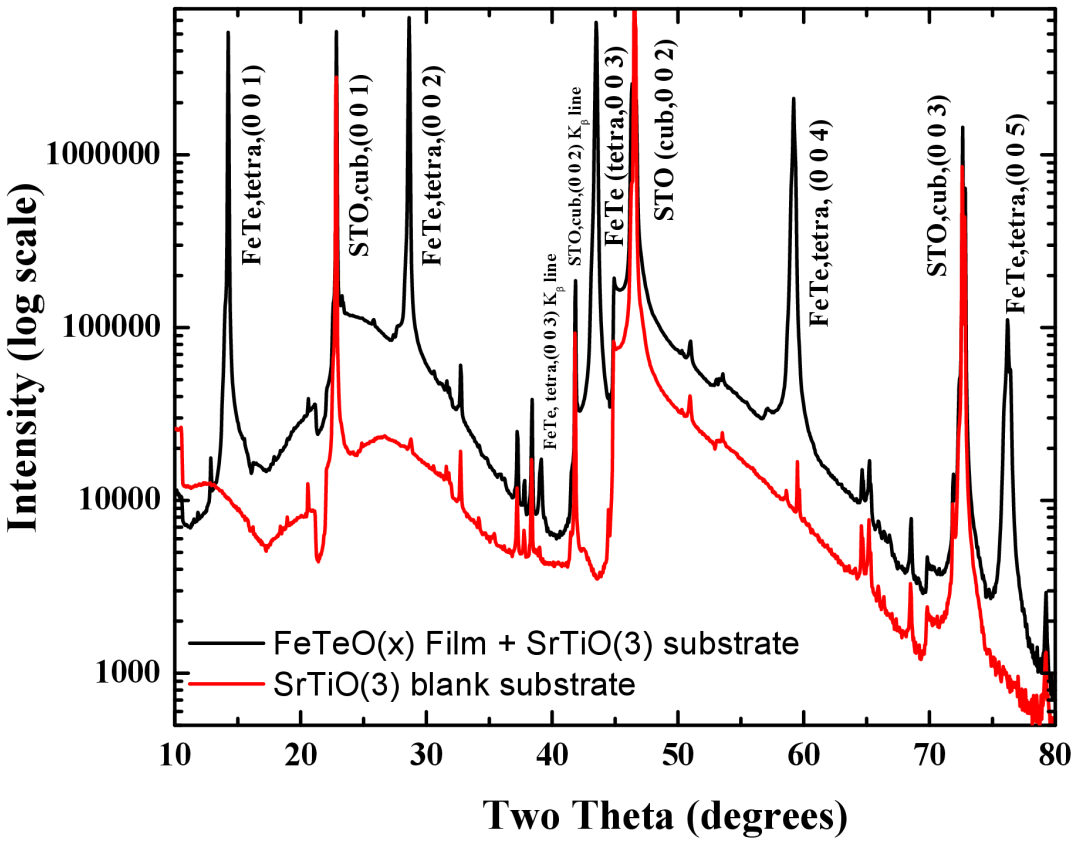

Figure 2-15 X-ray diffraction pattern taken perpendicular to the film surface of a $FeTeO_x$ film grown on $SrTiO_3$ substrate using a linear detector. The black solid line represents the XRD pattern of the film with substrate and the red solid line represents that of blank substrate

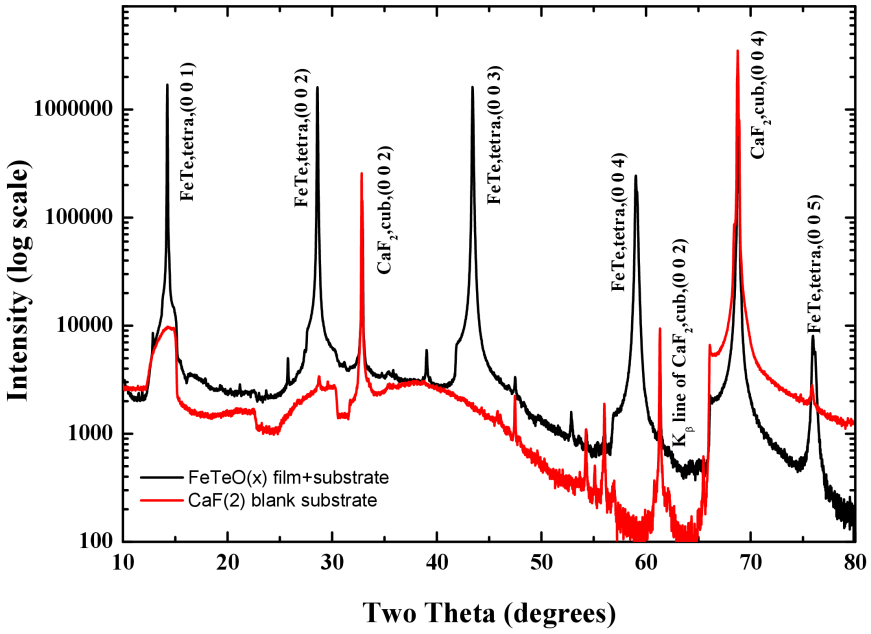

Figure 2-16 X-ray diffraction pattern taken perpendicular to the film surface of a $FeTeO_x$ film grown on CaF_2 substrate using a linear detector. The black solid line represents the XRD pattern of the film with substrate and the red solid line represents that of blank substrate.

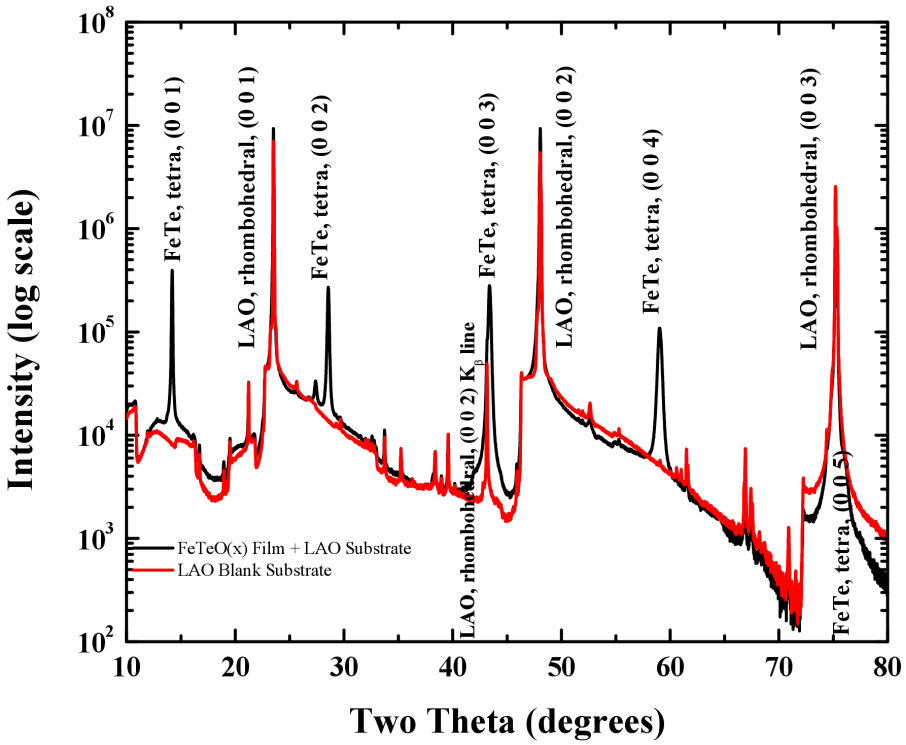

Figure 2-17 X-ray diffraction pattern taken perpendicular to the film surface of a $FeTeO_x$ film grown on LAO substrate using a linear detector. The black solid line represents the XRD pattern of the film with substrate and the red solid line represents that of blank substrate.

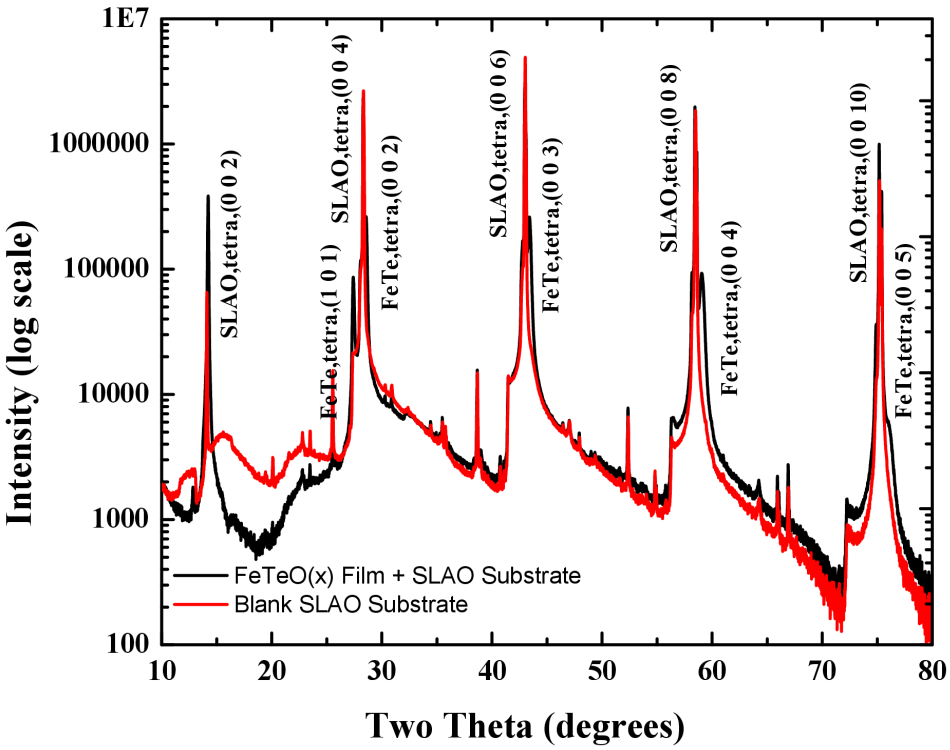

Figure 2-18 X-ray diffraction pattern taken perpendicular to the film surface of a $FeTeO_x$ film grown on SLAO substrate using a linear detector. The black solid line represents the XRD pattern of the film with substrate and the red solid line represents that of blank substrate.

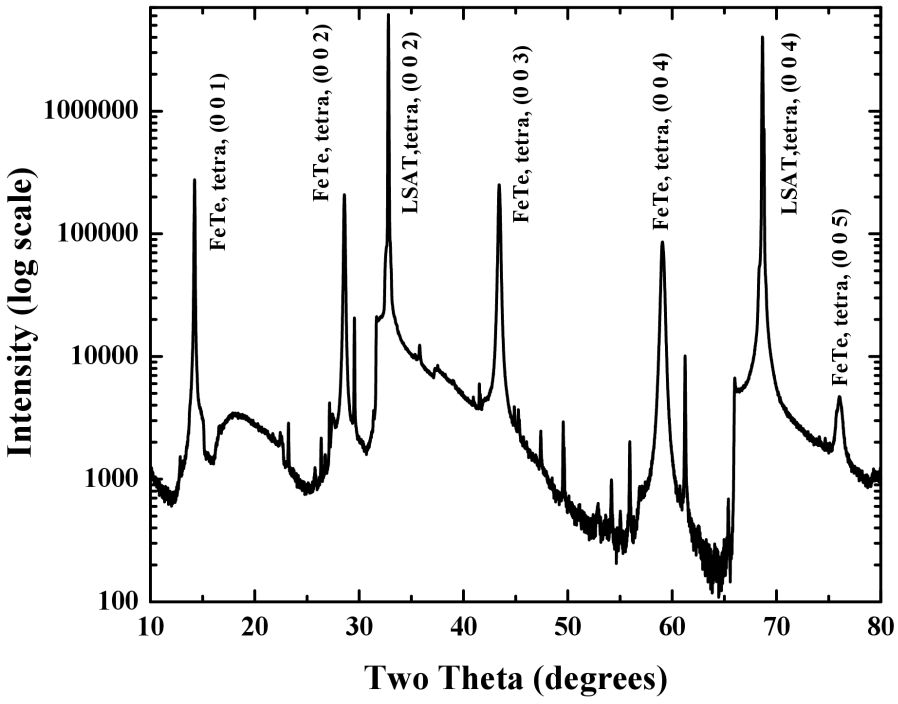

Figure 2-19 X-ray diffraction pattern taken perpendicular to the film surface of a $FeTeO_x$ film grown on LSAT substrate using a linear detector.

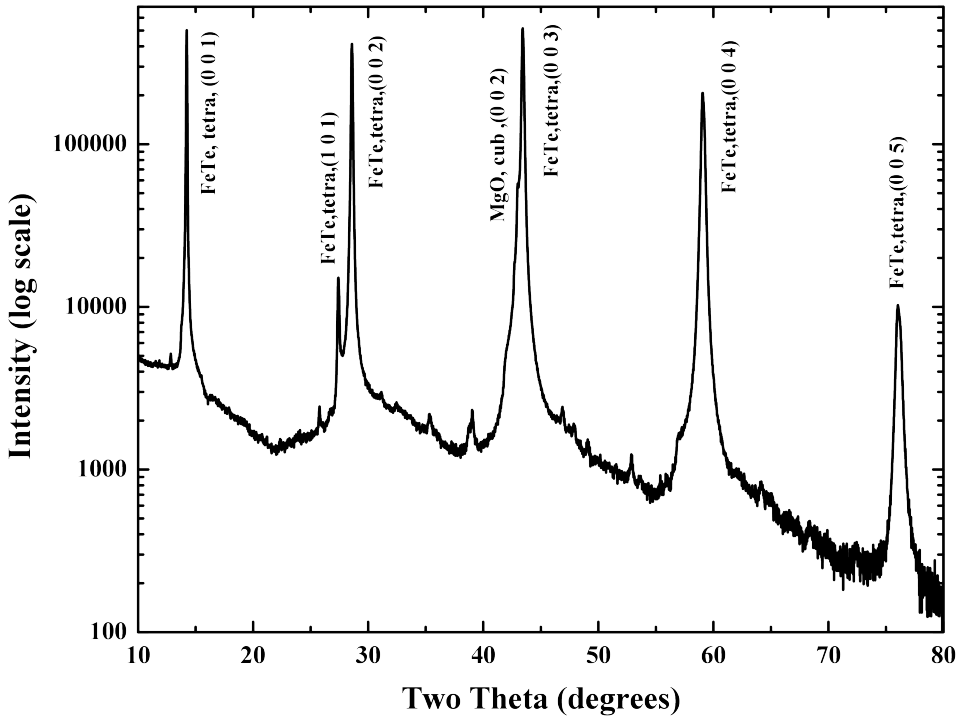

Figure 2-20 X-ray diffraction pattern taken perpendicular to the film surface of a $FeTeO_x$ film grown on MgO substrate using a point detector.

To examine the in-plane orientation of the film with respect to the substrate for films grown on MgO and CaF_2, off c-axis $FeTeO_x$ film peaks (1 0 4) and (1 1 5) were observed on an area detector of a 3-circle x-ray diffractometer. The beam dispersion images of (0 0 3), (1 0 4) and (1 1 5) film peaks for a $FeTeO_x$ thin film grown on MgO and CaF_2 substrates are shown in figures 2-21 and 2-22 respectively. The horizontal direction shows the dispersion in two-theta and vertical direction shows the dispersion in chi. The (0 0 3) peak for films on both substrates show a very small dispersion verifying the strong c-axis texture of films. For the film grown on MgO, the (1 0 4) and (1 1 5) peaks show some dispersion along chi direction but the dispersion is much smaller compared to that of films grown on $SrTiO_3$ substrate as shown in figure 2-14. Very interestingly the (1 0 4) and (1 1 5) peaks for the film grown on CaF_2 substrate showed a very small dispersion in both two-theta and chi directions indicating the much better in-plane orientation of the film with respect to substrate. When figures 2-14, 2-18 and 2-19 are compared

with each other it appears that the films grown on CaF_2 have the best in-plane orientation, the films grown on MgO substrate have relatively better in-plane orientation and the films grown on $SrTiO_3$ have the worst in-plane orientation. But when the lattice mismatch is considered, $SrTiO_3$ has the smallest in-plane lattice mismatch with FeTe (2 %), MgO has a somewhat larger lattice mismatch (11.23 %) and CaF_2 has the largest lattice mismatch (48.03 %). But it was believed that smaller lattice mismatch gives a better in-plane orientation. Hence the in-plane orientation of $FeTeO_x$ films on various substrates is surprising.

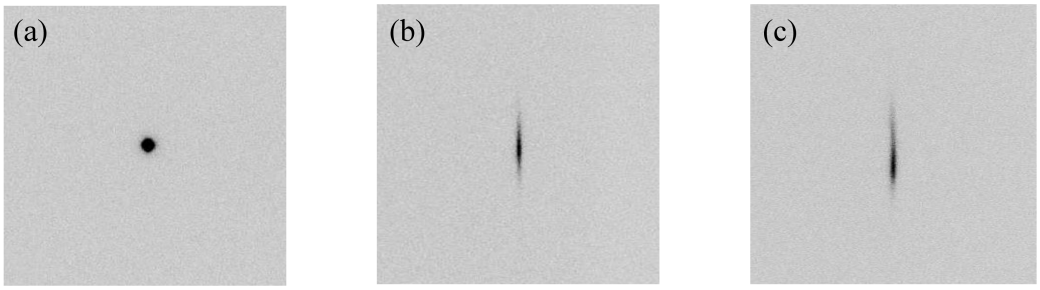

Figure 2-21 Beam dispersion images of the area detector of the 3-circle x-ray diffractometer obtained for Bragg reflections of a $FeTeO_x$ film grown on MgO substrate. The horizontal direction shows the dispersion in two-theta and vertical direction shows the dispersion in chi (a) (0 0 3) Bragg reflection (b) (1 0 4) Bragg reflection (c) (1 1 5) Bragg reflection.

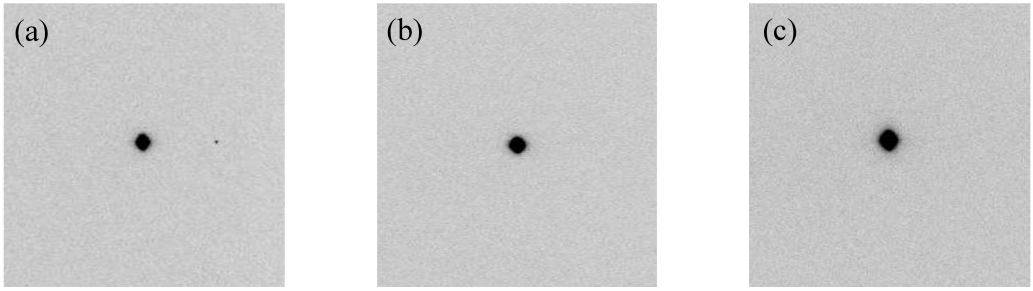

Figure 2-22 Beam dispersion images of the area detector of the 3-circle x-ray diffractometer obtained for Bragg reflections of a $FeTeO_x$ film grown on CaF_2 substrate. The horizontal direction shows the dispersion in two-theta and vertical direction shows the dispersion in chi (a) (0 0 3) Bragg reflection (b) (1 0 4) Bragg reflection (c) (1 1 5) Bragg reflection.

Some of the results observed during the low temperature x-ray diffraction experiment done at Brookhaven National Laboratory (BNL) using high resolution x-rays revealed very interesting information about the in-plane orientation of $FeTeO_x$ films on certain substrates. At BNL a 4-circle x-ray diffractometer was used to study the low temperature crystal structure of superconducting $FeTeO_x$. In this x-ray diffractometer, in order to obtain a Bragg reflection along a certain crystallographic direction of the sample a computer program can be used to rotate the sample. In order to do that an orientation matrix should be defined so that the instrument can identify crystallographic directions of the sample. In order to define an orientation matrix two independent crystallographic directions of the sample should be introduced to the instrument. In general (0 0 L) direction of the film is introduced to the instrument first. Then to define (H 0 0) direction w.r.t. (0 0 L) direction a data scan called "HK circle scan" is performed. In an HK circle scan, the sample in oriented at an appropriate angle to the (0 0 L) direction to catch a particular (H, K, L) peak and is then rotated around the (0 0 L) axis. For samples with (0 0 L) perpendicular to the sample surface, such a scan maps the in-plane mosaic. A phi scan is identical to an "HK circle scan" if the sample is oriented so that (0 0 L) is along the phi rotation axis.

The HK circle scan done to identify the (H 0 0) direction of $FeTeO_x$ film grown on a MgO substrate is shown in figure 3-23. The y-axis represents intensity and x-axis represents the angle of rotation along film surface. If the (H 0 0) direction of the film is aligned well along the (H 0 0) direction of MgO, in a full range of angle of rotation from 0˚ to 360˚ peaks should be present at every 90˚. In figure 3-23 instead of 90˚ intervals, well-defined peaks could be observed at 30˚ intervals. This is a clear evidence to support the fact that the $FeTeO_x$ lattice is rotated by 30˚ when growing on MgO substrate. The relationship between the in-plane lattice

constant of $FeTeO_x$ and MgO (4.21 Å) also supports the above fact since a_{MgO} x Cos 30°≈ $a_{FeTeO(x)}$. To account for the HK circle pattern we propose there are domains of $FeTeO_x$ with the in-plane orientation shown in figure 2-24 plus domains with the inverse rotation as well as domains with the axes aligned.

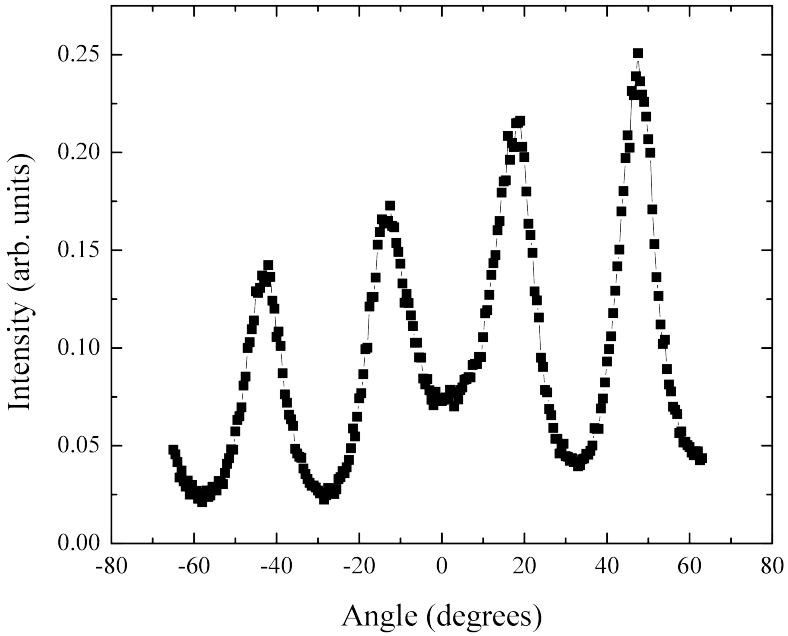

Figure 2-23 HK circle scan done on a $FeTeO_x$ film grown on MgO substrate. Y-axis represents the intensity of the plane and x-axis represents the angle along (L = 0) plane.

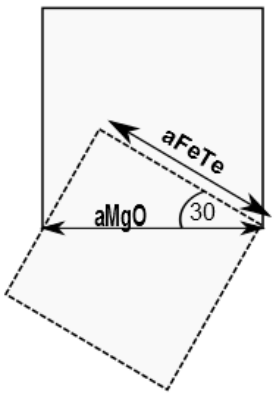

Figure 2-24 In-plane orientation of a $FeTeO_x$ unit cell on a MgO unit cell. The solid line represents MgO unit cell and dash line represents FeTe unit cell.

It appears that when the lattice mismatch is large between the film and substrate the $FeTeO_x$ lattice rotates until a favorable condition for atoms as well as a minimum lattice mismatch is satisfied. The same argument can be applied to the in-plane orientation of $FeTeO_x$ film on CaF_2 substrate. In this case $FeTeO_x$ lattice is rotated by 45˚ since the relationship between the in-plane lattice constants of $FeTeO_x$ and CaF_2 satisfies the condition, $a_{CaF(2)}$ x Cos 45˚ ≈ $a_{FeTeO(x)}$. The proposed in-plane orientation of the $FeTeO_x$ film with respect to the CaF_2 substrate is demonstrated in figure 2-25.

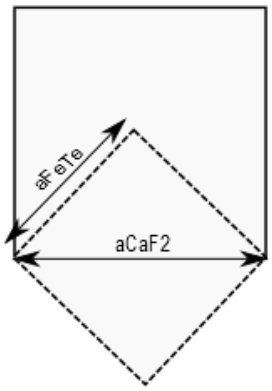

Figure 2-25 In-plane orientation of a $FeTeO_x$ unit cell on a CaF_2 unit cell. The solid line represents CaF_2 unit cell and dash line represents FeTe unit cell.

This is consistent with the results reported by Tsukada.[40] A similar result was observed in a neutron diffraction experiment done at Paul Scherrer Institute in Switzerland. This experiment will be explained in detail in chapter 5 of this thesis. When aligning an $FeTeO_x$ film grown on CaF_2 substrate in a triple axis spectrometer in order obtain structural Bragg reflections, it was discovered that [1 0 0] crystallographic direction of $FeTeO_x$ is parallel with [1 1 0] crystallographic direction of CaF_2 substrate. It was also noted that the edge of the CaF_2 substrate

is parallel to [1 1 0] crystallographic direction of CaF_2. This observation verifies that $FeTeO_x$ lattice rotates by 45˚ with respect to the CaF_2 substrate during growth.

X-ray diffraction measurements done at Rigaku using a 6-circle x-ray diffractometer on thick and thin films of $FeTeO_x$ grown on CaF_2 substrate were also helpful in characterizing the crystalline quality of films. On this system sample could be aligned at grazing incidence so that Bragg reflections could be measured that lie in the plane of the film. The phi scans done along (4 4 0) Bragg reflection of CaF_2 substrate and along (4 0 0) Bragg reflection of $FeTeO_x$ film are shown in figure 2-26. Both Bragg reflections could be seen in the same values of phi revealing that [1 1 0] of CaF_2 is parallel with [1 0 0] of $FeTeO_x$. The narrow peaks seen at each 90˚ interval in 3-26 (b) indicates the epitaxial growth of the film on CaF_2 substrate.

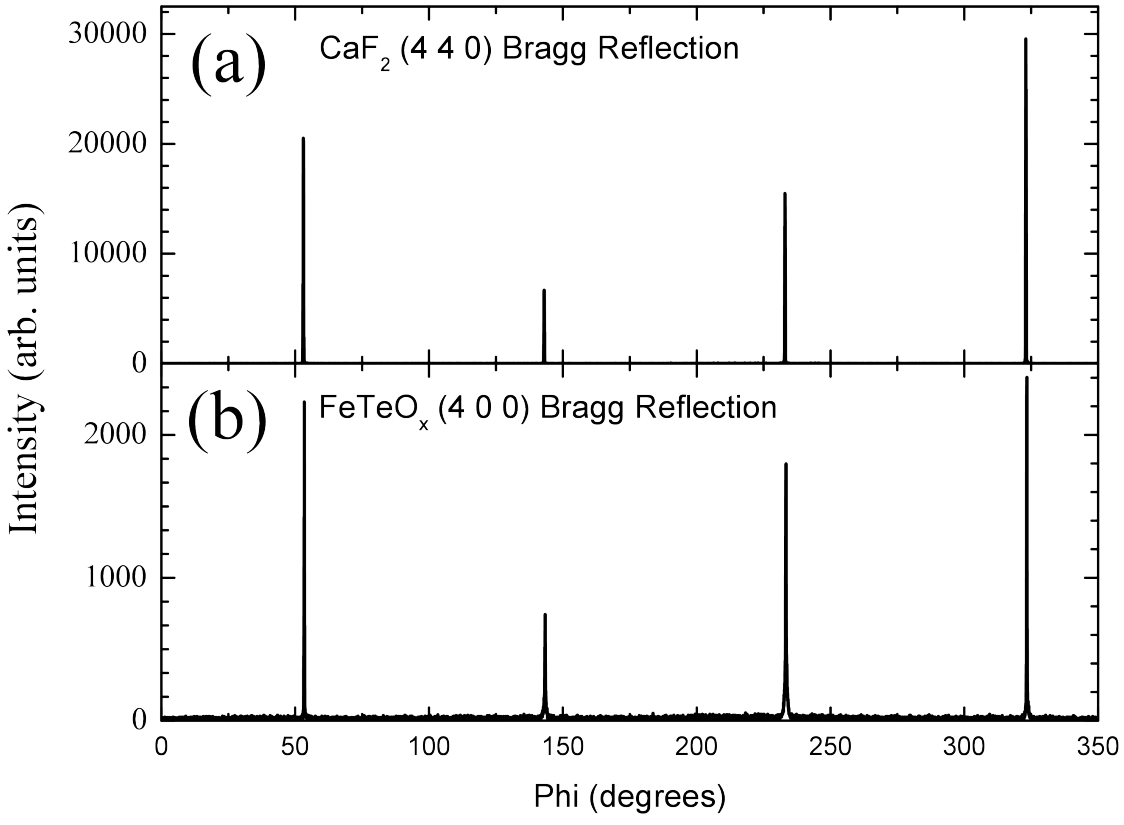

Figure 2-26 Phi scans done along (a) CaF_2 (4 4 0) Bragg reflection (b) $FeTeO_x$ Bragg reflection

An expanded view of a phi scan done on an in-plane Bragg reflection (3 3 0) of $FeTeO_x$ for a thin film and thick film is shown in figure 2-27. As a reference the same measurement done on a CaF_2 substrate on a Bragg reflection along the same direction is shown in the same figure. It can be seen that the thin film as shown in figure 2-27(b) has a much better in-plane mosaic compared to the thick film as shown in figure 2-27(c).

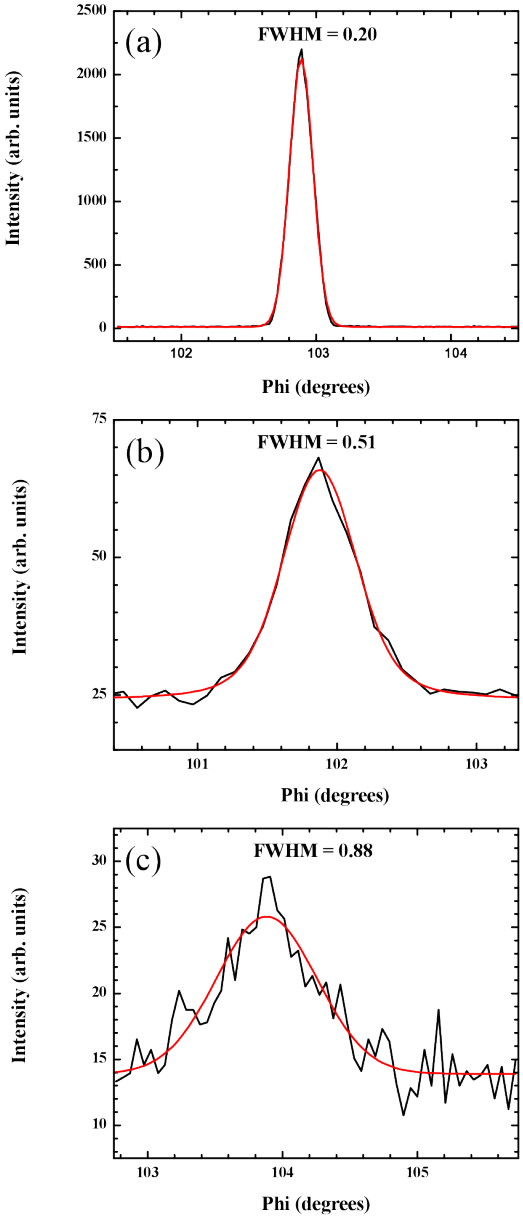

Figure 2-27 Phi scan of (a) (0 0 6) Bragg reflection of CaF_2 substrate (b) (3 3 0) Bragg reflection of a thin $FeTeO_x$ film (c) (3 3 0) Bragg reflection of a thick $FeTeO_x$ film.

The HK-circle scan done to identify the (H 0 0) direction of $FeTeO_x$ film grown on a $SrTiO_3$ substrate is shown in figure 2-28. A small peak could be seen around 0˚ but this sits on a large background unlike the well-separated peaks seen in figure 3-23 for a film grown on a MgO substrate. This reflects the poor in-plane orientation of the $FeTeO_x$ film on $SrTiO_3$ substrate. It can be considered almost as a powder diffraction pattern. This is consistent with the wide beam dispersion images along chi direction obtained from the area detector in a 3-circle diffractometer as shown in figure 3-14.

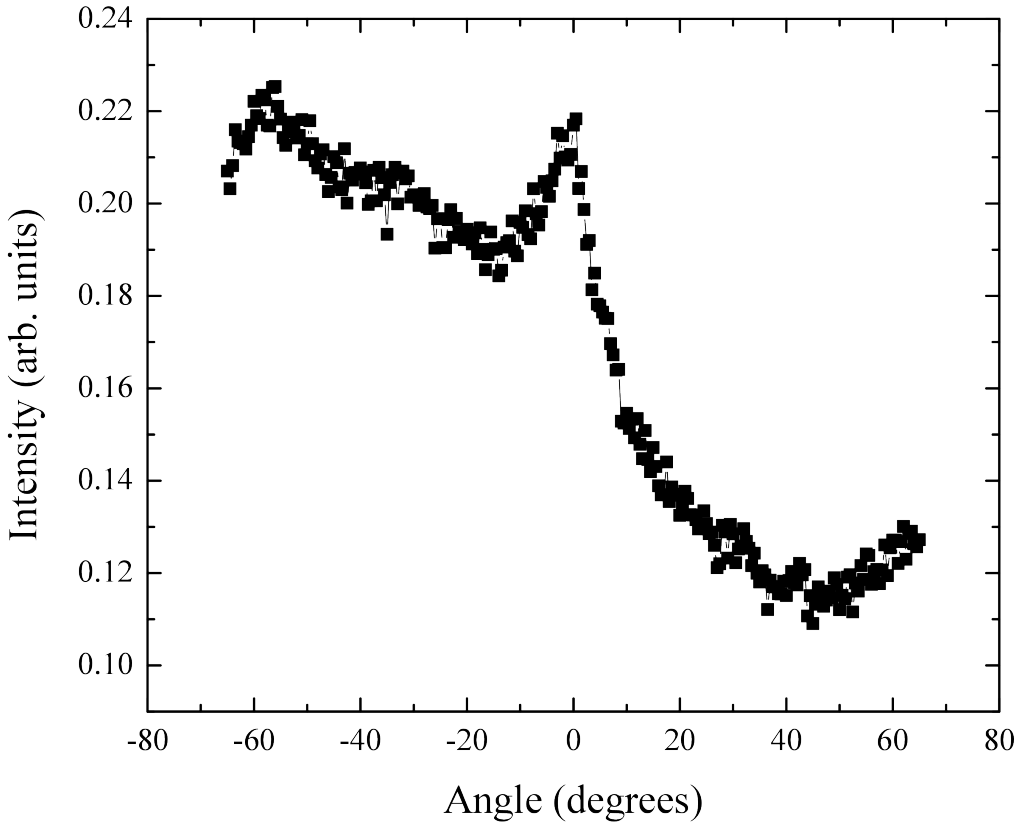

Figure 2-28 HK-circle scan done on a $FeTeO_x$ film grown on $SrTiO_3$ substrate. Y-axis represents the intensity of the plane and x-axis represents the angle along (H = 0, K = 0) plane.

In summary $FeTeO_x$ films were grown on various substrates with different in-plane lattice constants. On all substrates the $FeTeO_x$ films were grown well along the c-axis with respect to the substrate. On the substrates which have a larger lattice mismatch like MgO and

CaF_2 the in-plane orientation of the film was much better compared to that of a film grown on a substrate which has a smaller lattice mismatch. It appears that when the lattice mismatch is large the $FeTeO_x$ lattice tends to rotate with respect to the substrate such that the lattice mismatch is minimized. So far the best epitaxial growth could be observed in $FeTeO_x$ films grown on CaF_2 substrate.

2.6.2 Effect of oxygen Pressure on superconductivity of $FeTeO_x$ films grown on Different substrates.

As described in section 2.52 in order to make superconducting $FeTeO_x$ films with stable oxygen concentration oxygen was incorporated into FeTe films during growth. The oxygen concentration could be controlled by changing the partial oxygen pressure inside the chamber during growth. In order to induce superconductivity in films grown on $SrTiO_3$ at least 4.0×10^{-6} Torr partial oxygen pressure was required.

In general, there is a close relationship between the concentration of dopants and the superconducting transition temperature. Hence a careful study was carried out to check whether there is any change in superconducting transition temperature with the change in amount of oxygen in $FeTeO_x$. Superconducting $FeTeO_x$ films were grown on the substrates mentioned in the previous section using various oxygen partial pressures.

The temperature dependent resistances of $FeTeO_x$ films grown on various substrates using various pressures are shown in figures 2-29 through 2-34. Films grown on all the oxide substrates except LSAT showed superconducting transitions at oxygen pressures higher than $4*10^{-6}$ Torr. There was no significant change in superconducting transition temperature with the change in oxygen pressure. The superconducting transition remained around 13 K for all $FeTeO_x$

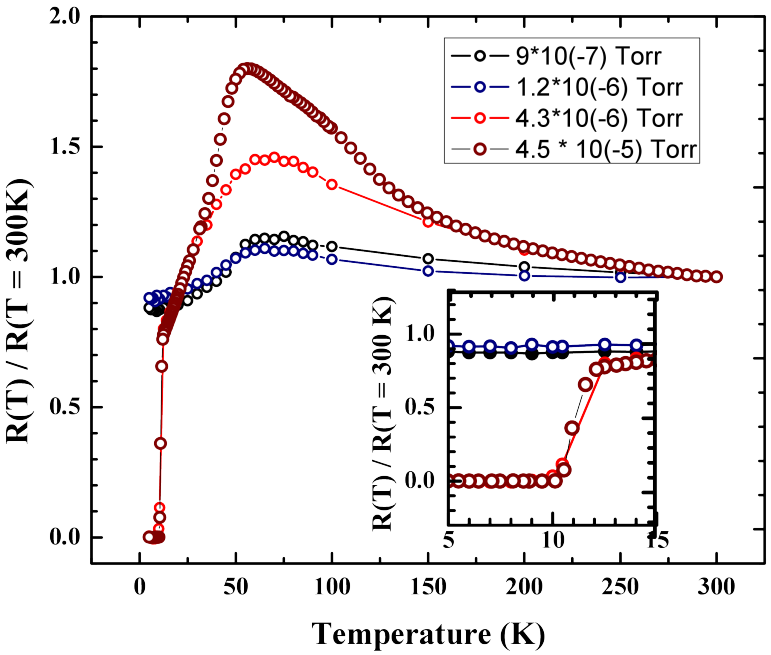

Figure 2-29 Temperature dependent resistance of $FeTeO_x$ films grown on $SrTiO_3$ substrates at several oxygen partial pressures. Resistance is normalized to the value at 300 K. Inset shows the onset of superconductivity around 13 K with zero resistance around 10 K.

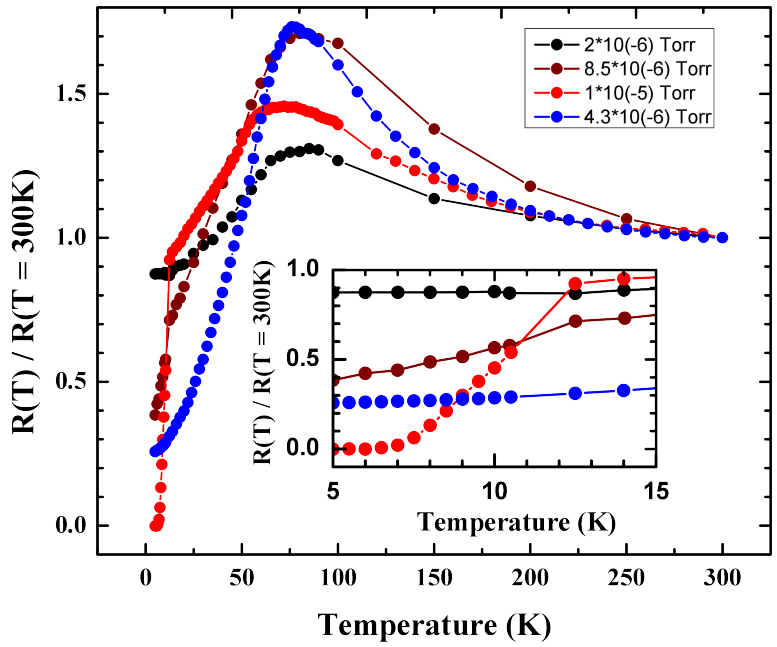

Figure 2-30 Temperature dependent resistance of $FeTeO_x$ films grown on $SrLaAlO_4$ substrates at several oxygen partial pressures. Resistance is normalized to the value at 300 K. Inset shows the onset of superconductivity around 12 K with zero resistance around 7 K.

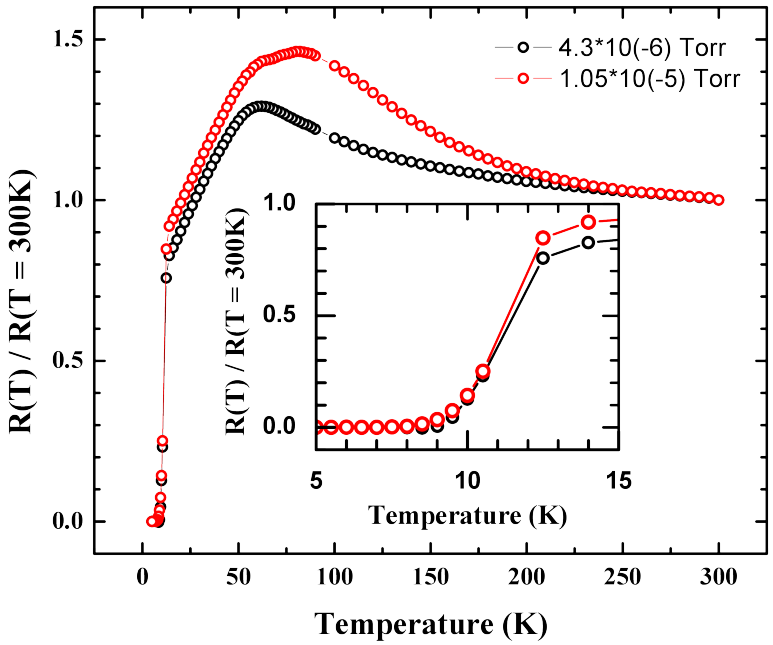

Figure 2-31 Temperature dependent resistance of $FeTeO_x$ films grown on $LaAlO_3$ substrates at several oxygen partial pressures. Resistance is normalized to the value at 300 K. Inset shows the onset of superconductivity around 12 K with zero resistance around 9 K.

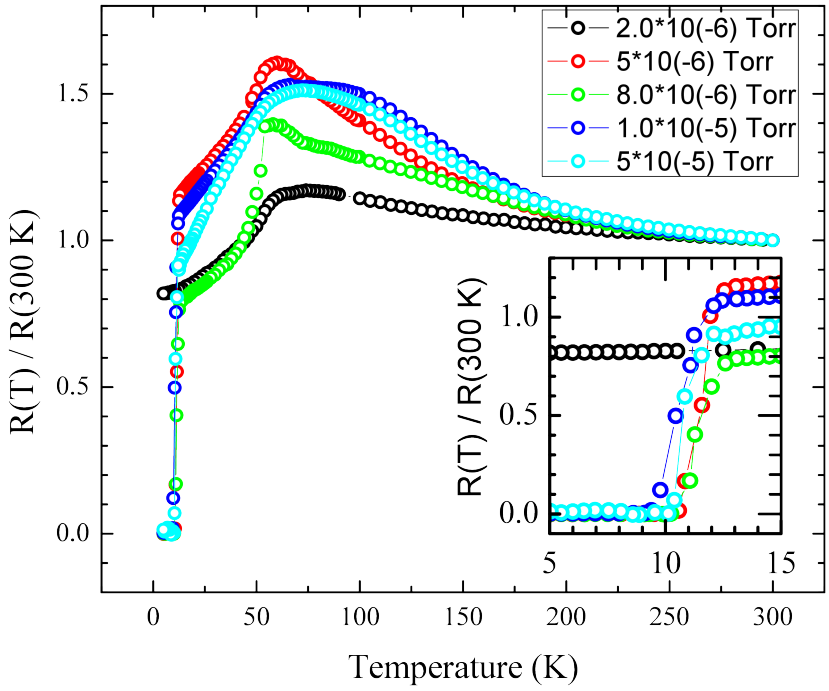

Figure 2-32 Temperature dependent resistance of $FeTeO_x$ films grown on MgO substrates at several oxygen partial pressures. Resistance is normalized to the value at 300 K. Inset shows the onset of superconductivity around 13 K with zero resistance at 10.5 K. The resistivity curve in green color shows a clear transition around 65 K corresponding to magnetic and structural transition.

films. However, on different substrates there were some changes in the temperature where zero resistance state was achieved and some changes in the temperature where a peak in resistivity was seen.

Films grown on MgO showed the sharpest superconducting transitions, with zero resistance achieved around 10.5 K as shown in figure 2-32. Compared to all other resistivity curves the green color curve in fig. 2-32 shows a sharper transition around 50 K corresponding to the structural and magnetic transition seen in bulk FeTe. This indicates that much better crystalline properties in $FeTeO_x$ films on MgO compared to the films grown on other oxide substrates.

An extraordinary behavior could be seen in the temperature dependent resistivity of films grown on LSAT substrate as shown in figure 3-33. In these films a superconducting transition could be seen around 12 K similar to others. Here the resistance became a constant value below the superconducting transition temperature and never decreased to zero. It seems like the films undergo the superconducting transition but there exists some chemical inhomogeneity in the sample that prevents it achieving zero resistance. This result was reproducible for several oxygen pressures indicating that this was not inherent to a particular film but for films grown on LSAT substrate. Interestingly LSAT has the best in-plane lattice match with $FeTeO_x$ (0.95 %) compared to the other substrates studied. It appears that some chemical impurities are deposited during film growth when $FeTeO_x$ lattice tries to grow matching up with the LSAT lattice. The x-ray diffraction pattern taken perpendicular to the ab plane of $FeTeO_x$ film grown on LSAT substrate doesn't show any anomaly compared to the films grown on other substrates. Therefore it can be speculated that any chemical inhomogeneity associated with this film is too subtle to detect by a technique like x-ray diffraction.

Surprisingly the FeTe films grown on CaF_2 substrate couldn't be made superconducting by incorporating oxygen during growth. The temperature dependent resistivity of $FeTeO_x$ films grown on CaF_2 substrates at various temperatures in a range of higher oxygen pressures are shown in figure 3-34. When a higher oxygen pressure like 10^{-4} Torr was used the resistance of $FeTeO_x$ grown on CaF_2 at low temperatures showed an insulating behavior as shown in figure 3-35. It seems that at higher oxygen pressures iron oxides and Tellurium oxides were the dominant species formed.

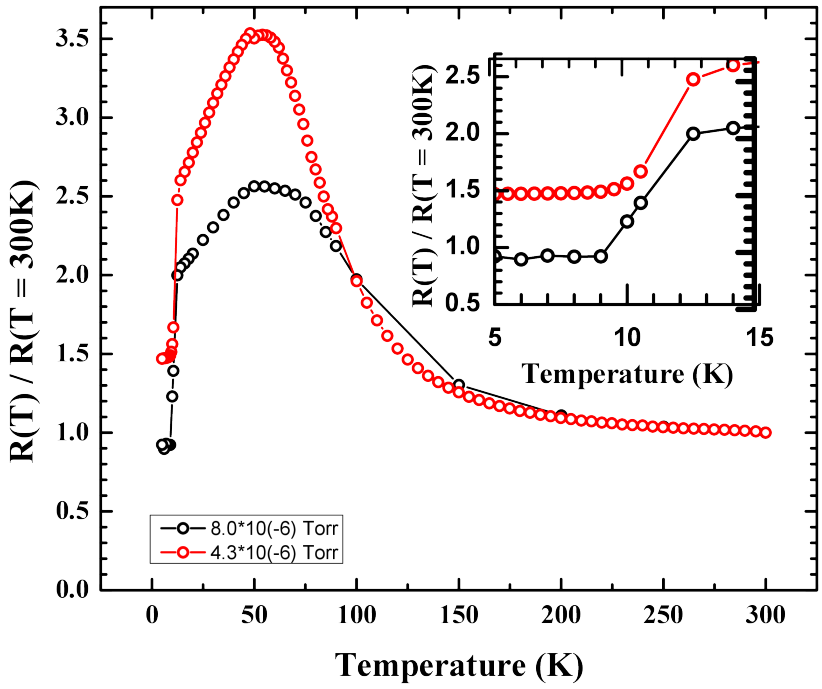

Figure 2-33 Temperature dependent resistance of $FeTeO_x$ films grown on LSAT substrates at different oxygen partial pressures. Resistance is normalized to the value at 300 K. Inset shows the superconducting transition around 12 K and an unusual constant resistance state at lower temperatures.

Several other attempts have been made to make these films superconducting. One was to anneal in oxygen after growth. Another method was to grow the film at 380 ˚C in a regular oxygen pressure like $1x10^{-5}$ Torr and once the film was at a temperature of 200 ˚C increasing the oxygen pressure to 100 mTorr while cooling the film. Another attempt was taken to introduce an

oxygen layer between substrate surface and film before film growth. None of these efforts were successful in incorporating oxygen into the film. This non-superconducting behavior of $FeTeO_x$ grown on CaF_2 substrate is a puzzle to be addressed.

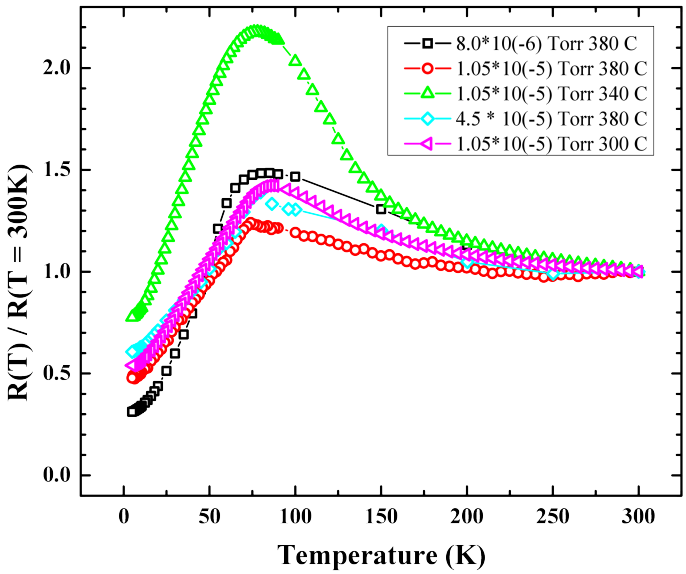

Figure 2-34 Temperature dependent resistance of $FeTeO_x$ films grown on CaF_2 substrates at several oxygen partial pressures and at several growth temperatures. Resistance is normalized to the value at 300 K. No superconducting transition could be observed around 13 K.

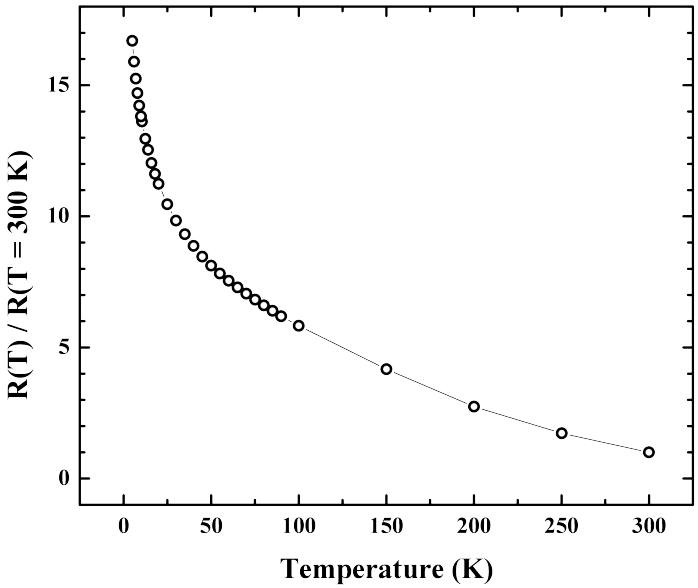

Figure 2-35 Temperature dependent resistance of $FeTeO_x$ films grown on CaF_2 substrate at 380 ˚C at $1x10^{-4}$ Torr oxygen partial pressure. An insulator behavior can be seen at low temperatures.

The micro-structure of $FeTeO_x$ grown on various substrates and the in-plane orientation of $FeTeO_x$ films on various substrates shed some light in understanding the above issue with films grown on CaF_2 substrate. The scanning electron microscope images taken on films grown on $SrTiO_3$, MgO and CaF_2 are shown in figure 3-36.

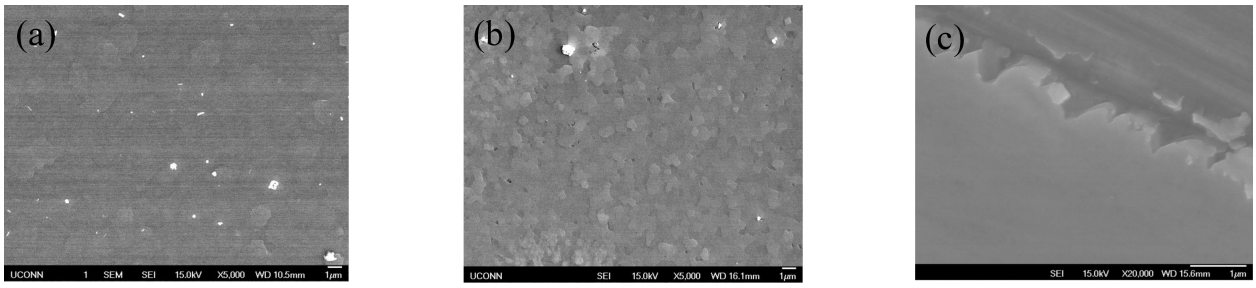

Figure 2-36 The scanning electron images of $FeTeO_x$ films grown on (a) $SrTiO_3$ substrate (b) MgO substrate (c) CaF_2 substrate, edge has been used to focus the image, white color represents film and ash color represents substrate.

The surface morphology of films grown on CaF_2 is much smoother than that of films grown on $SrTiO_3$ and MgO. As explained in the previous section, the $FeTeO_x$ films grow on CaF_2 with better epitaxy and these films are very smooth. It appears that it is hard to incorporate oxygen into these epitaxially grown smooth films on CaF_2 compared to the films grown on oxide substrates with somewhat porous micro structure. So far it has been very difficult to incorporate oxygen into FeTe bulk single crystals. It can be assumed that FeTe films grown on CaF_2 substrate behaves very similar to single crystalline bulk FeTe in micro structure and crystal structure. Hence non-superconducting FeTe films grown on CaF_2 substrates serve good reference samples.

2.7 Magnetization measurements of $FeTeO_x$ films

In order to verify the bulk superconductivity of $FeTeO_x$ films grown in oxygen atmosphere the temperature dependent magnetic moment was measured by applying a small magnetic field perpendicular to the ab-plane of the film. The aim of the experiment was to achieve a diamagnetic signal below the superconducting transition temperature. For a 100 nm thick $FeTeO_x$ film the result is shown in figure 3-37. First the sample was mounted in SQUID magnetometer such that a magnetic field could be applied perpendicular to the ab-plane of the film. Then the sample was cooled in zero field and 50 Oe magnetic field was applied at 2 K. The magnetic moment was measured in two cycles, while warming up the sample (Zero field cool) and secondly cooling down the sample in magnetic field (field cool). In the zero field cool procedure as the temperature reaches 7 K there is a sharp increase in magnetic moment indicating that some portion of the sample shows some magnetic order. This can be due to several reasons. One possibility is that some magnetic impurities accumulated in the sample such as iron oxide or unreacted iron can be responsible for the magnetic signal.

To overcome the paramagnetic signal arises at low temperature due to magnetic impurities a much thicker film around 400 nm is used. The resulting graph is shown in figure 3-38. For this sample a diamagnetic response could be observed below 3 K. For superconductors in general one tends to see T_c onset for magnetic transition about same or a little lower to the onset of zero resistance. But for superconducting $FeTeO_x$ the temperature dependent resistivity shows a zero resistance state around 10 K but the magnetic transition is observed around 3 K.

This result is consistent with the magnetization measurement reported by Si for superconducting $FeTeO_x$ films. This indicates that the observation of magnetic transition at a low

temperature is a puzzle to be addressed and it is common for $FeTeO_x$ system in general and not a particular issue associated with growth conditions.

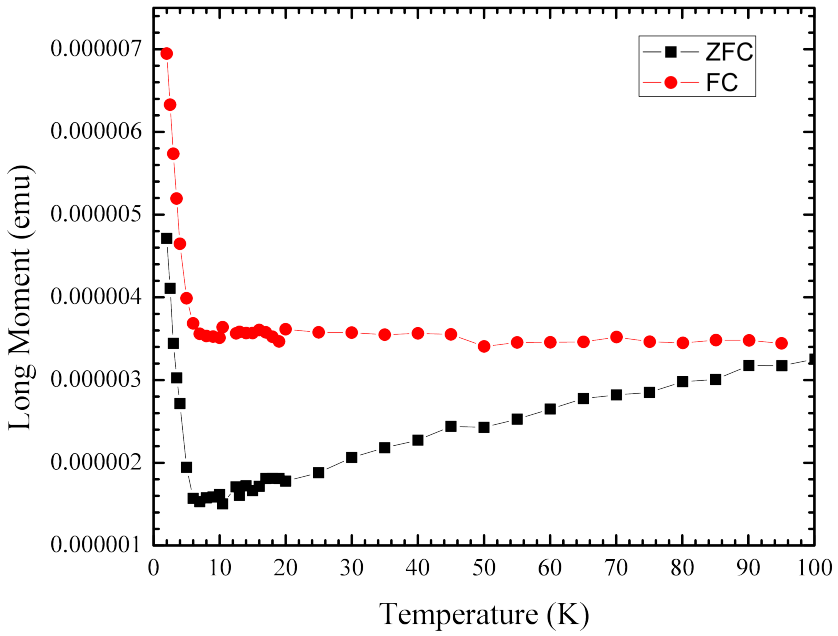

Figure 2-37 Temperature dependent magnet moment of a 100 nm thick superconducting $FeTeO_x$ film grown on $SrTiO_3$ substrate. Magnetic field of 50 Oe is applied perpendicular to the ab-plane of the film.

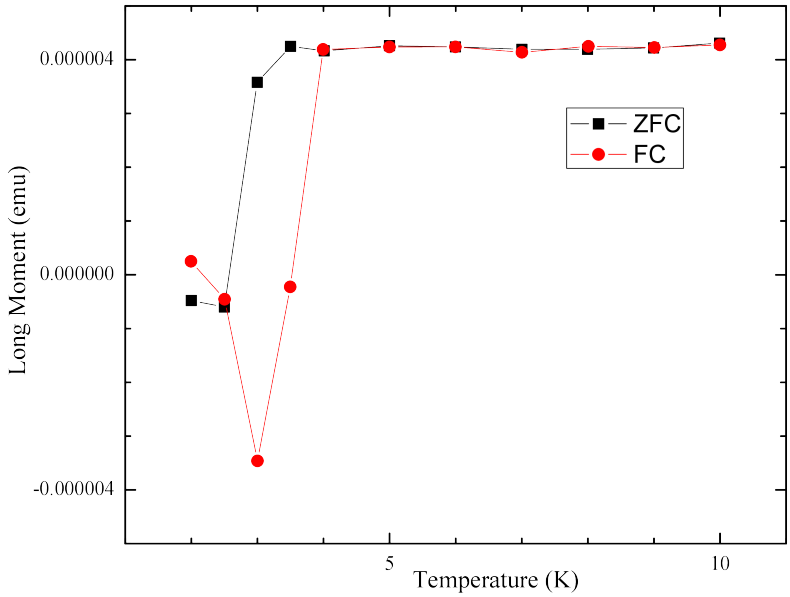

Figure 2-38 The diamagnetic response of a 400 nm thick superconducting $FeTeO_x$ film grown on $SrTiO_3$ substarte. The magnetic field 50 Oe is applied perpendicular to the ab plane of film.

2.8 Conclusion

Previously FeTe films were grown in vacuum and oxygen was incorporated by post growth annealing. This was possible due to the porous micro structure of films. Oxygen could be easily removed from the film by low temperature anneals in vacuum making the superconductivity of $FeTeO_x$ reversible. The oxygen in these films was unstable preventing doing the experiments at low temperature in vacuum that involved higher intensity phonons. Therefore a new growth mode was introduced to make $FeTeO_x$ films with stable oxygen concentration, much better micro structure and crystalline structure. In this growth mode three major growth parameters were changed compared to the previous growth mode. Target to substrate distance was minimized, a higher laser power was used and a dense polycrystalline conglomerate was used as the target. Films grown using this new growth mode were dense, smooth and it was hard to incorporate oxygen into these films by post growth annealing. Therefore oxygen has to be incorporated during growth into these films. The oxygen concentration of these films were stable.

$FeTeO_x$ film growth on various substrates with different lattice constants were tested. On all substrates films were grown with good c-axis texture but the quality of the in plane orientation of the film was highly dependent on the substrate. The best epitaxial $FeTeO_x$ films were grown on CaF_2 substrate. The FeTe lattice was rotated by 45˚ with respect to the substrate axes when growing on CaF_2. It appears that when the lattice mismatch is large between substrate and film the FeTe lattice tends to rotate such that a favorable atomic position and minimum lattice mismatch is satisfied.

The amount of oxygen in $FeTeO_x$ films was varied by changing the partial oxygen pressure in the growth chamber. The experiment was performed to look for any changes in the superconducting transition temperature associated with the change in amount of oxygen of the

films. For films grown on oxide substrates superconductivity was achieved when the partial oxygen pressure inside the growth chamber was between 4 x 10^{-6} Torr and 5 x 10^{-5} Torr. With the change of amount of oxygen, no significant change in the superconducting transition temperature was observed. The superconducting transition temperature remained near 13 K and there were some changes in the temperature where the zero resistance state was achieved. This result is consistent with the temperature dependent resistivity of $FeTeO_x$ reported by others.[22,33,41] It seems like $FeTeO_x$ comes to an energetically favorable state around 13 K and remains in this state even though the amount of oxygen is changed by a significant amount or $FeTeO_x$ only forms for a given value of x.

It was difficult to incorporate oxygen into films grown in CaF_2 due to the dense micro structure and smooth surface morphology of the films. FeTe films grow on CaF_2 are very similar to bulk single crystals. A recent report claims to find superconductivity at the surface of $FeTeO_x$ single crystals after exposing them to air for six months.[39] Based on this result it may be possible to induce oxygen in the surface layer of FeTe films grown on CaF_2 substrate.

3 Low temperature Crystal Structure of Superconducting $FeTeO_x$ films

3.1 Background and Motivation

In iron-based superconductors, the relationship between structure, magnetism and superconductivity has been always a puzzle.[5,7,42] The parent compounds of iron-based superconductors show structural transitions associated with magnetic transitions. When a superconductor is created from a parent compound, how the crystal structure changes due to the appearance of superconductivity is a question of interest. Iron pnictides show a structural transition from tetragonal to orthorhombic associated with antiferromagnetic order[43–46]. In $LaO_{1-x}F_xFeAs$ (one member of the 1111 family) as a function of doping, antiferromagnetism and orthorhombic distortion disappear before the appearance of superconductivity[10]. In contrast, in 122 family of iron pnictides, orthorhombic symmetry survives in superconducting state and suppresses at a higher doping level.[11,47–50] Unlike $LaO_{1-x}F_xFeAs$, another member of 1111 family $SmO_{1-x}F_xFeAs$, behaves similar to 122 family.[51] Even within a certain family in iron-based superconductors, it is not clear how the crystal structure is affected due to the appearance of superconductivity. Hence, what is the exact role of crystal structure in creating a superconductor from a parent compound is a question to be addressed.

Iron chalcogenides have a simpler crystal structure compared to other iron-based superconductors.[3] FeTe is considered as the parent compound for this family. It shows antiferromagnetic order around 65 K and undergoes a structural transition depending on the excess iron in the structure.[23,24] For a high excess iron concentration ($x = 0.141$) $Fe_{1+x}Te$ shows a structural transition from tetragonal to orthorhombic associated with incommensurate antiferromagnetic order and for a low excess iron concentration ($x = 0.076$) the transition is from tetragonal to monoclinic associated with commensurate antiferromagnetic order.[23] The typical

route to make FeTe superconducting is by substituting Se or S into Te sites.[15,20] This method is a charge neutral substitution which involves a large change in the lattice. Upon doping of Se into Te sites the long range antiferromagnetic order and the associated structural transition get suppressed and superconductivity appears. At the optimal doping level of $FeTe_{0.5}Se_{0.5}$ the highest superconducting transition temperature obtained for this compound is 15 K.[9,52] The less well known route to make FeTe superconducting is by incorporation of oxygen.[21,22] By this method superconductivity could be only achieved in thin film form but not yet in bulk. This is a charge doping mechanism where the valence of ion changes to 3+ in superconducting state.[21,34] Density functional calculations[53] and a recent report[41] shows that oxygen occupies interstitial sites of FeTe lattice. At room temperature the crystal structure of superconducting $FeTeO_x$ is quite similar to parent FeTe[21] but the low temperature crystal structure of $FeTeO_x$ is still unknown. Other end member of iron chalcogenide family FeSe, which has a similar crystal structure to that of FeTe at room temperature is superconducting with transition temperature of 8 K[3] and undergoes a structural transition from tetragonal to orthorhombic around 90 K.[25,26] Unlike the structural transitions observed in other iron-based superconductors, this is not associated with any magnetic order and it is assumed that tetragonal to orthorhombic structural transition occurs favoring superconductivity in FeSe.[25,26] One possibility is that similar to FeSe, $FeTeO_x$ undergoes a structural transition from tetragonal to a crystal structure, which favors superconductivity. A temperature dependent study of the crystal structure of superconducting $FeTeO_x$ will reveal whether there exists any crystal structure at low temperature, which favors superconductivity in $FeTeO_x$. In addition this investigation will provide new insights into understanding what properties are changed, which are not when creating the superconductor $FeTeO_x$ from parent FeTe.

In addition to doping application of pressure became significant in enhancing or inducing superconductivity of iron-based superconductors. FeSe shows the most dramatic pressure effect where the superconducting transition temperature increases from 8 K to 37 K by application of hydrostatic pressure.[27–29] A large enhancement in superconducting transition temperature was also shown in $FeTe_{0.5}Se_{0.5}$ under high pressure.[30,31] A strong dependence of superconductivity on pressure in iron-based superconductors was revealed by a thermal discontinuity at superconducting transition temperature. Sensitive dialatometry measurements has been used to detect the changes in lattice parameters at the vicinity of superconducting transition temperature in $FeTe_{0.5}Se_{0.5}$[54] as well as Co doped $BaFe_2As_2$[55–57] and KFe_2As_2.[58] This thermal discontinuity can be related to a uniaxial pressure dependence of superconducting transition temperature through the Ehrenfest relation.[59]

Ehrenfest equations describe the thermodynamic relations between specific heat and derivatives of specific volume in second order phase transitions. These equations can be adopted to describe a relationship between the uniaxial pressure dependence of superconducting transition temperature, $\frac{dT_c}{dP_i}$, the discontinuity in specific heat at the phase transition ΔC_p and the discontinuity in thermal expansion at the phase transition $\Delta\alpha_i$ for a second order normal to superconducting phase transition as follows.

$$\frac{dT_c}{dP_i} = V_m \frac{\Delta\alpha_i \, T_c}{\Delta C_p}$$

Where V_m is the molar volume. By applying the measured thermodynamic quantities to the right hand side of the above equation uniaxial pressure dependence on superconducting transition can be calculated. However due to the anisotropy related with hydrostatic pressure the reported

enhancements in superconducting transition temperatures are not in well agreement with the predicted values by Ehrenfest relation.

3.2 Experimental Details

The aim of the experiment was to check whether superconducting $FeTeO_x$ films undergo any structural transition before the appearance of superconductivity and to check whether there exists any new phase in $FeTeO_x$ below the superconducting transition temperature which favors superconductivity. We were interested in tracking down two possible structural transitions. Hence the first experiment was to check whether the non-superconducting FeTe and superconducting $FeTeO_x$ films show the structural transition from tetragonal to monoclinic similar to bulk FeTe. Second experiment was to check whether superconducting $FeTeO_x$ shows an orthorhombic distortion in its superconducting state similar to superconducting FeSe. Measuring the temperature dependent lattice constants of superconducting $FeTeO_x$ and non-superconducting FeTe films was another aim of this experiment.

In order to get structural information of the above system x-ray diffraction technique has been used. Since $FeTeO_x$ is only produced in thin films yet, the appropriate techniques to study thin films were required. In this experiment particularly we were looking for splitting of certain Bragg peaks at lower symmetry, low temperature vs the higher symmetry, high temperature phase. In addition we were interested in tracking down the changes in lattice constants with respect to temperature. Intensity associated with such diffraction in thin films was not sufficient to do the experiment using laboratory sources. Therefore higher resolution synchrotron x-ray diffraction technique has been used in order to achieve above goals.

The low temperature crystal structure of superconducting $FeTeO_x$ was studied using higher resolution x-ray diffraction technique in Brookhaven National Laboratory, National Synchrotron

Light Source, X-22C beam line. Diffraction profiles for $FeTeO_x$ films and $Fe_{1.02}Te$ single crystals were obtained by incident x-rays with wavelength 1.1271 Å. X-ray diffraction data were taken in reflection geometry on a four circle diffractometer with a beam spot of 1.8 mm x 0.6 mm. Before the detector a Si (111) analyzer was mounted to achieve high angular resolution. The samples were cooled down to 1.5 K base temperature using a cryostat and data were taken while warming the sample. In order to protect the samples from high energy x-rays at low temperature in vacuum several Al foils were used between the incoming x-ray beam and sample.

The room temperature crystal structure of superconducting $FeTeO_x$ was well established as tetragonal.[21] Particularly we were interested in tracking down two low temperature structures, which we predicted can be possible in superconducting $FeTeO_x$. They were monoclinic or orthorhombic. In the following we index peaks using the high temperature tetragonal phase (P4/*nmm*) which is common in similar materials.[23,24] The Bragg reflection (1 1 6) and (1 0 6) are used to identify the above two structural transitions. Both high temperature tetragonal (1 0 6) peak and (1 1 6) peak splits into two peaks when the low temperature phase is monoclinic. When the low temperature phase is orthorhombic only the high temperature (1 0 6) peak splits into two but (1 1 6) peak doesn't. Therefore for superconducting samples temperature evolution of (1 1 6) peak and (1 0 6) peak were studied. In order to obtain the temperature dependent changes in c-axis lattice parameter (0 0 4) Bragg reflection and (0 0 7) Bragg reflection were studied.

In this experiment four samples were tested. The sample description, the structural peaks tested and the temperature range they were tested are shown in the table below.

Sample Name	The structural peaks tested	Temperature Range
1 st $FeTeO_x$ film on $SrTiO_3$ substrate	(-1 0 6)	20 K, 30 K, 40 K, 50 K, 60 K, 80 K, 100 K,120 K
	(-1 -1 6)	20 K, 30 K, 40 K, 50 K, 60 K, 80 K, 100 K,120 K
	(0 0 7)	1.5 K to 120 K
2nd $FeTeO_x$ film on $SrTiO_3$ substrate	(0 0 7)	1.5 K to 30 K
$FeTeO_x$ film on MgO substrate	(1 0 6)	1.5 K, 5 K, 10 K, 15 K, 20 K, 70 K
	(1 1 6)	1.5 K, 5 K, 10 K, 15 K, 20 K, 70 K
	(0 0 4)	1.5 K to 70 K
Bulk single crystal $Fe_{1.05}Te$	(0 0 4)	1.5 K to 120 K

Table 3-1 Summary of the structural peaks and temperature range the samples were tested at BNL, NSLS, X-22 C

3.3 Results

In this chapter the results will be given in the chronological order the samples were tested. The conclusions arrived from each data set and issues associated with the data sets will be discussed. The solutions taken to overcome the issues will be explained and the resulting data sets observed eliminating the previous mentioned issues will be presented. The results observed after resolving above-mentioned issues can be categorized into two sections. If the reader is interested in directly going to through those results, please refer from page 74 to 80 to read about the change in crystal symmetry observed for superconducting $FeTeO_x$ films at low temperature and from page 88 to 94 to read about the changes in lattice constants observed for superconducting $FeTeO_x$ films and bulk single crystals of non-superconducting FeTe.

For first superconducting sample grown on $SrTiO_3$ substrate x-ray diffraction data were taken for (0 0 7) Bragg reflection varying the temperature from 1.5 K to 120 K. The sample was aligned at 1.5 K to observe $FeTeO_x$ (0 0 7) peak and the (0 0 7) Bragg peaks in the longitudinal theta/2theta direction was observed in the temperature range from 1.5 K to 120 K. The two-theta values obtained from fitted theta/2theta scans at each temperature were applied in the Bragg

equation to calculate the c-axis lattice parameter at each temperature. A theta/two theta data scan of a $FeTeO_x$ (0 0 7) Bragg reflection obtained at 1.5 K is shown in figure 4.1. The data is fitted by a Gaussian.

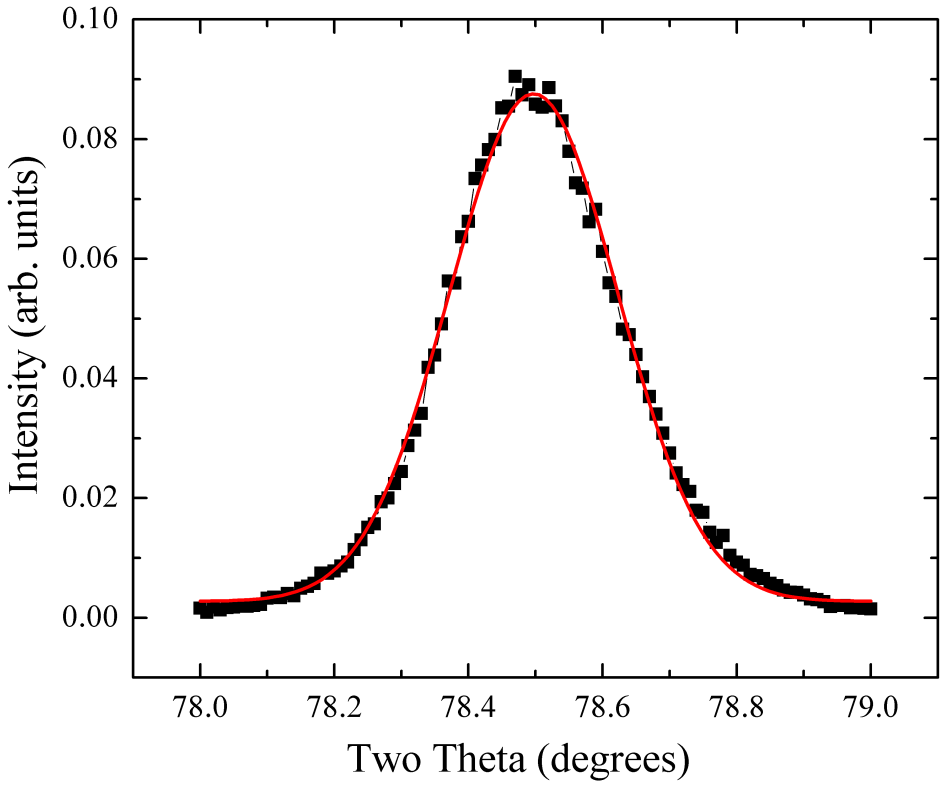

Figure 3-1 $FeTeO_x$ (007) Bragg Reflection in the longitudinal theta/two-theta direction obtained at 1.5 K. The red solid line represents a Gaussian.

The temperature evolution of the c-axis lattice parameter obtained using $FeTeO_x$ (0 0 7) Bragg reflection is shown in figure 4.2. The change in the c-axis lattice parameter observed around 60 K indicates that a structural transition can exist in superconducting $FeTeO_x$ around 60 K. Below the superconducting transition temperature 12.5 K, any significant change in c-axis lattice parameter could not be observed.

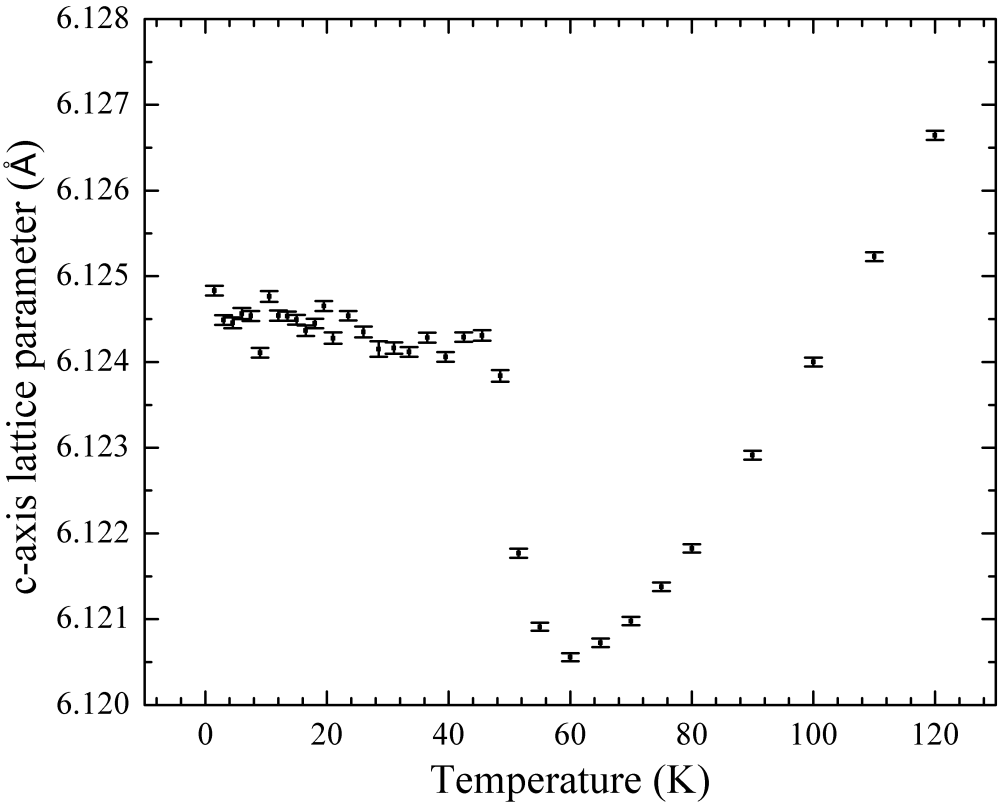

Figure 3-2 Temperature evolution of the c-axis lattice parameter observed using $FeTeO_x$ (007) Bragg Reflection

To find out exact details about any structural transition, which can exist in, the above sample around 60 K the Bragg reflections (-1 -1 6) and (-1 0 6) were studied by varying the temperature. For above two Bragg reflections data scans were taken in longitudinal theta/two theta direction for temperatures 20 K, 30 K, 40 K, 50 K, 60 K, 80 K, 100 K and 120 K.

The theta/2theta data scan of (-1 -1 6) $FeTeO_x$ peak observed at 20 K, 50 K and 60 K is shown in figure 4-3. At 60 K a single peak can be seen representing the tetragonal phase at high temperature. At a low temperature, 20.0 K, the data shows two peaks representing (-1 -1 6) and (-1 -1 -6) peaks in accordance of the monoclinic structure of the parent FeTe compound.

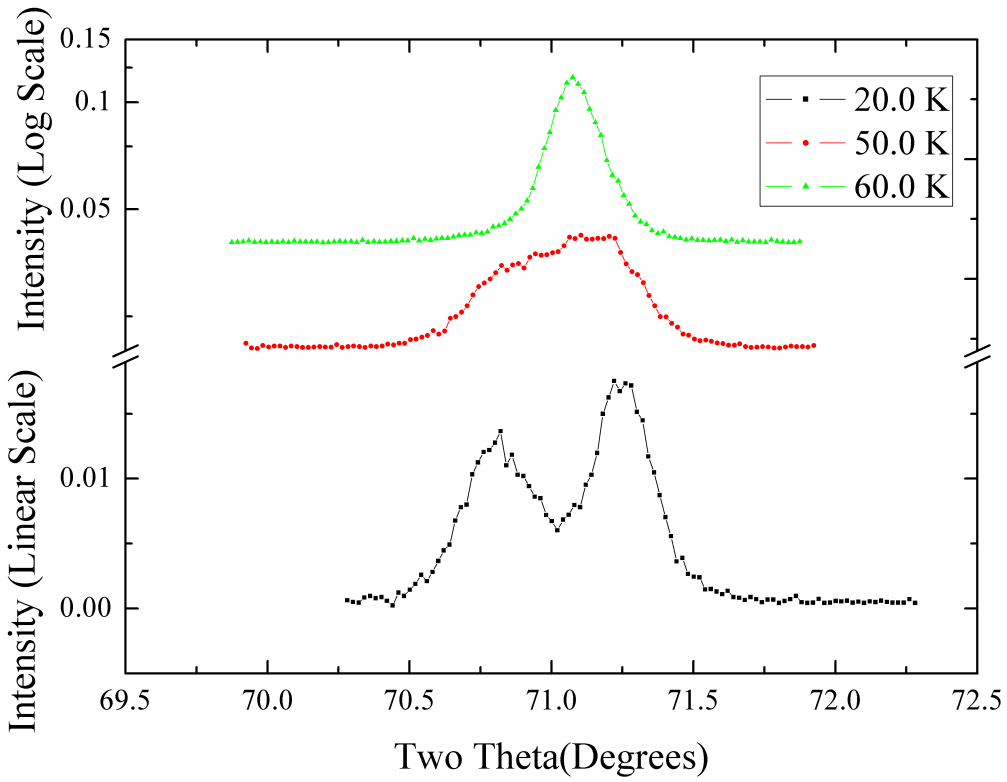

Figure 3-3 Temperature evolution of the tetragonal (-1 -1 6) Bragg peak. Upon cooling, the sample becomes monoclinic as shown by splitting of the (-1 -1 6) peak.

The theta/2theta data scan of (-1 0 6) peak observed at 60 K, 50 K and 20 K is shown in figure 4-4. This data scan shows a similar temperature evolution to that of (-1 -1 6) peak. Since both (-1 -1 6) and (1 0 6) peaks split into two peaks below 60 K we concluded that the superconducting $FeTeO_x$ undergoes a structural transition from tetragonal to monoclinic around 60 K.

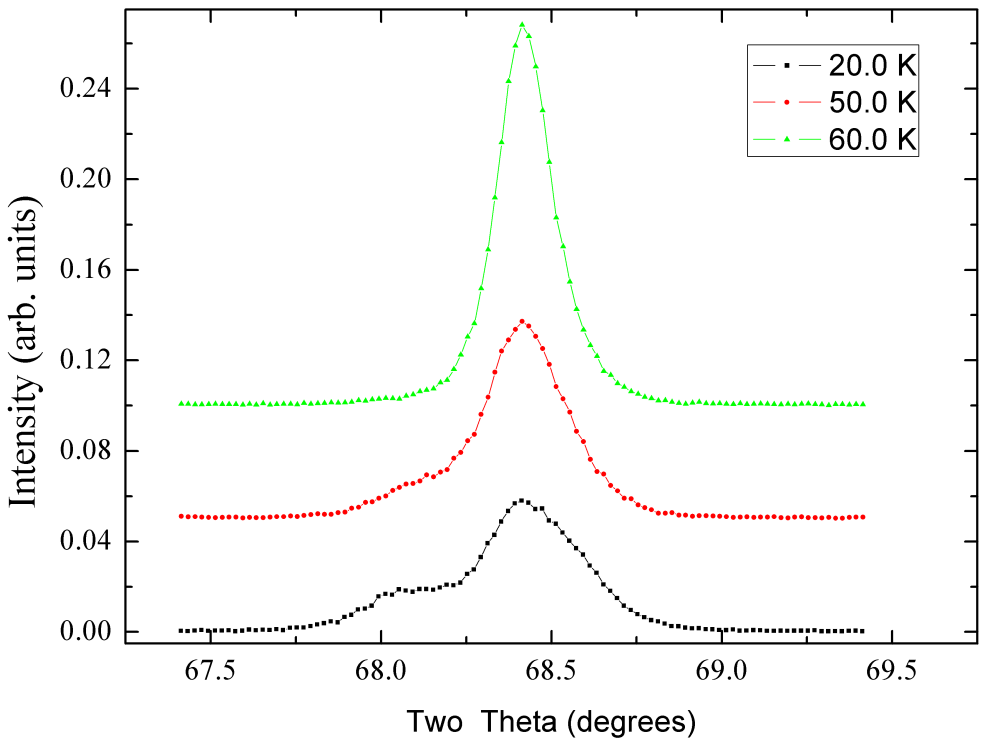

Figure 3-4 Temperature evolution of the tetragonal (-1 0 6) Bragg peak. The single peak, which represents the high temperature tetragonal phase at 60 K, splits into two peaks at a low temperature of 20 K.

For this sample below the superconducting transition temperature, no significant change in c-axis lattice constant could be observed. To check whether the sample shows the same superconducting properties after the exposure to the high energy x-ray beam the resistance of the sample was measured using a cryostat of a quantum design magnetic property measurement system by the four probe method. The temperature dependent resistance of the sample before and after the exposure to x-ray beam is shown in the figure 4-5. Before the exposure to the x-ray beam sample showed a superconducting transition around 12.5 K and the zero resistance state was achieved around 9.5 K. But after the exposure to x-ray beam sample still showed a superconducting transition but the zero resistance couldn't be achieved. It is possible that due to the interaction of the high energy x-ray beam with the sample oxygen in the sample absorbed

energy from photons and driven out from the sample destroying the superconductivity of sample. Next time extra precaution was taken when exposing the sample to higher energy x-ray beam.

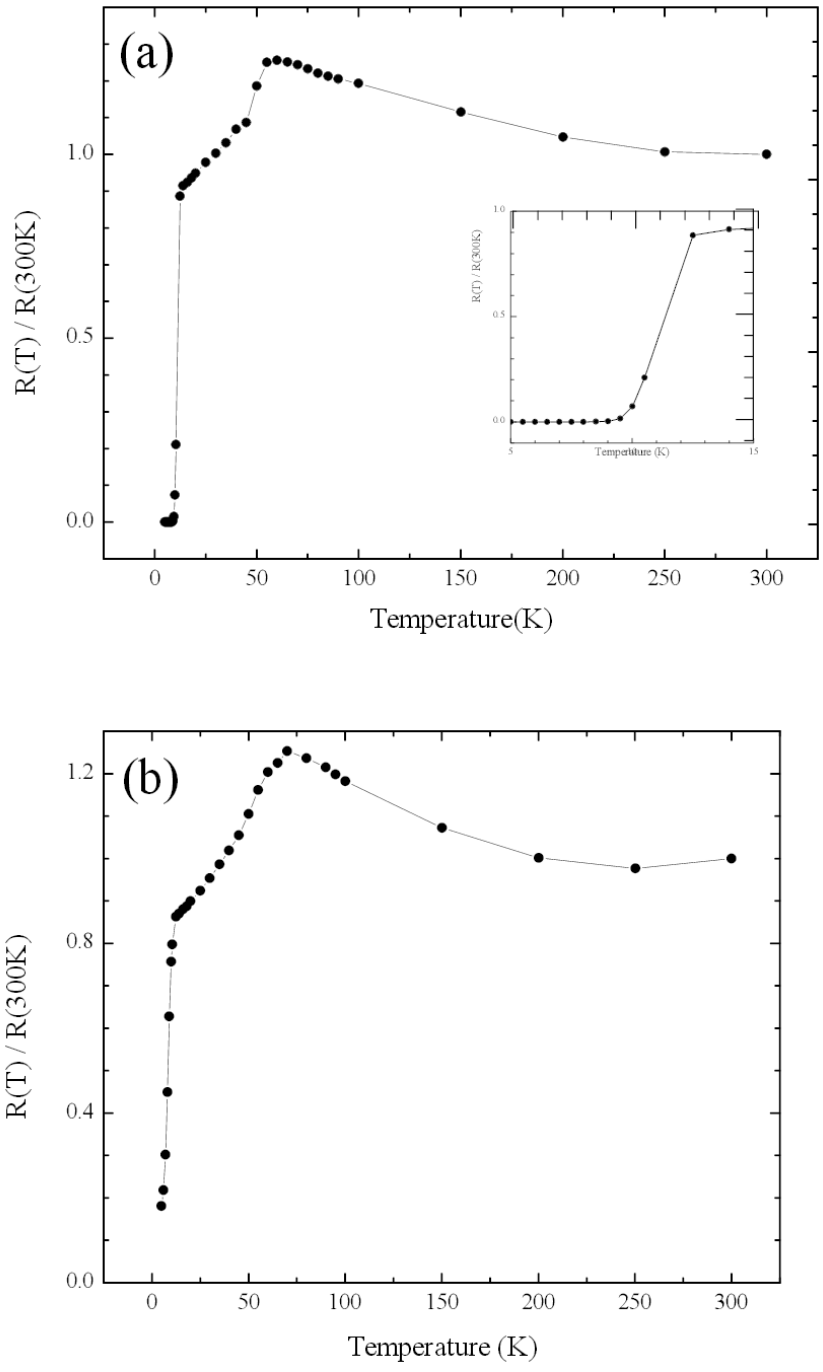

Figure 3-5 Temperature dependent resistance of the first superconducting sample, $FeTeO_x$ film grown on $SrTiO_3$ substrate, (a) Before the exposure to the higher energy x-ray beam. (b) After the exposure to the higher energy x-ray beam.

To check whether there exists any significant change in the c-axis lattice parameter below the superconducting transition temperature another sample grown on $SrTiO_3$ substrate was studied. First the sample was aligned to observe the (0 0 7) $FeTeO_x$ film peak at 1.5 K and the (0 0 7) Bragg peaks in the longitudinal theta/2theta direction was observed in the temperature range from 1.5 K to 80 K. One layer of Aluminum foil were used in between the incoming x-ray beam and the sample to protect the sample from high energy x-ray beam. The two theta values obtained from fitted theta/two-theta scans at each temperature were applied in the Bragg equation to calculate the c-axis lattice parameter at each temperature. A theta/twotheta data scan of a $FeTeO_x$ (0 0 7) Bragg reflection obtained at 52.5 K is shown in figure 4.6. The data is fitted by a Voigt function.

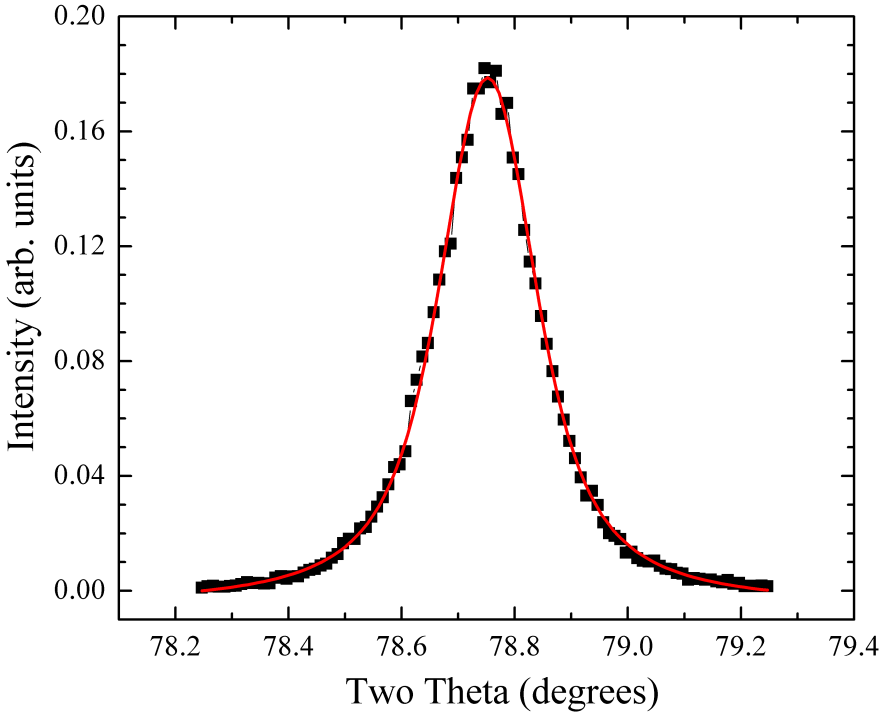

Figure 3-6 $FeTeO_x$ (007) Bragg Reflection in the longitudinal theta/two-theta direction obtained at 52.5 K. The red solid line represents a Voigt function.

The temperature evolution of the c-axis lattice parameter obtained using $FeTeO_x$ (0 0 7) Bragg reflection is shown in figure 4-7.

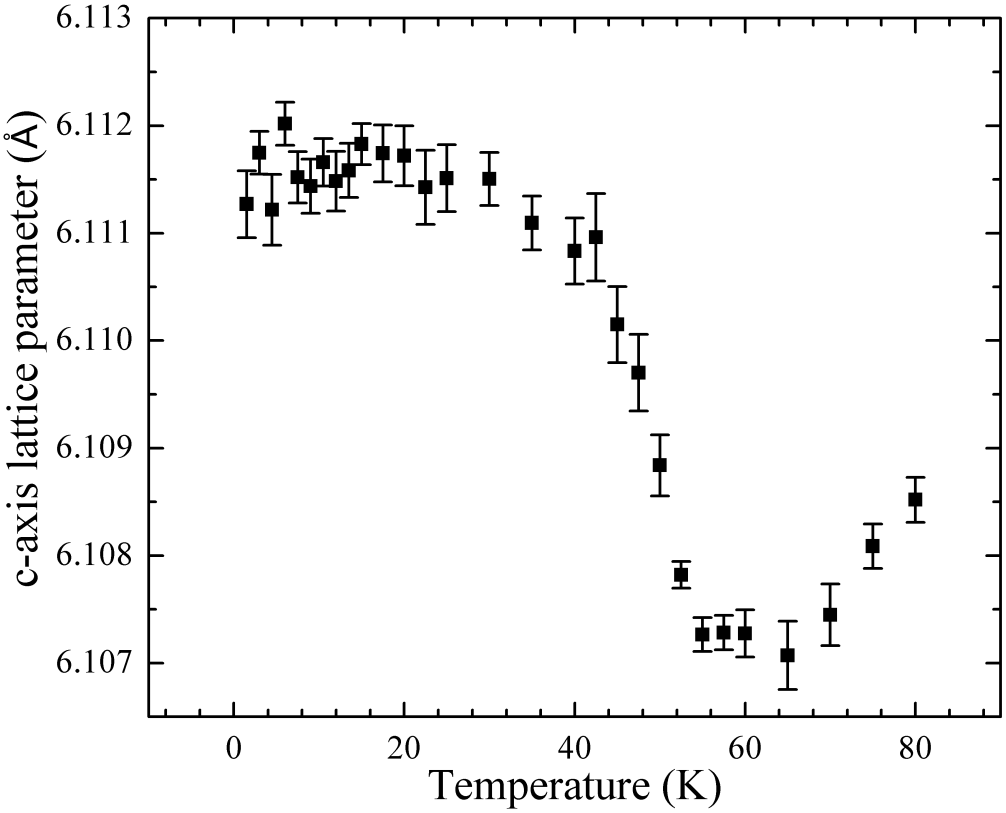

Figure 3-7 Temperature evolution of the c-axis lattice parameter observed using $FeTeO_x$ (007) Bragg Reflection

The change in the c-axis lattice parameter around 60 K could be visible similar to the previous sample indicating that this sample also undergoes a structural transition from tetragonal o monoclinic around 60 K. In addition a decrease in the c-axis lattice parameter could be observed at the vicinity of superconductivity but the data were noisy so we couldn't come to a firm conclusion.

Then the x-ray beam was exposed to a different place in the same sample and the above procedure was repeated. First the sample was aligned to observe $FeTeO_x$ (007) peak at 1.5 K and the diffraction profiles in longitudinal theta/2theta direction were observed varying the

temperature up to 30 K. The temperature dependent c-axis lattice parameter calculated using the fitted theta/2theta scans of FeTeOx (007) peak is shown in the figure 4.8. Data scans were fitted with voigt function.

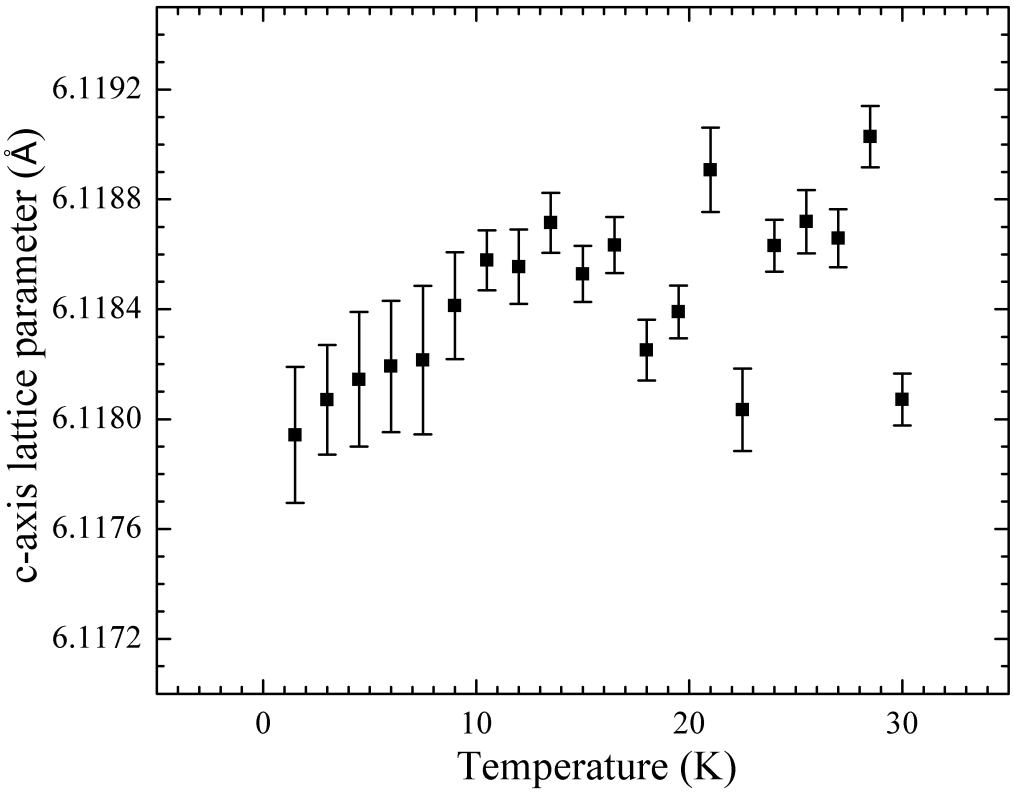

Figure 3-8 Temperature evolution of the c-axis lattice parameter observed using $FeTeO_x$ (007) Bragg Reflection

In this graph a clear decrease in the c-axis lattice parameter at the vicinity of superconducting transition could be observed but the absolute change in c-axis lattice parameter ($C_{10.5\ K}$-$C_{1.5\ K}$) was smaller than the error bars calculated for each data point. So we couldn't come to a firm conclusion.

So far we were able to detect that superconducting $FeTeO_x$ undergoes a structural transition from tetragonal to monoclinic similar to the parent compound FeTe. A change in the c-axis lattice parameter could be observed at the vicinity of superconducting transition but the data

quality was not enough to come to a conclusion. So far superconducting films grown on $SrTiO_3$ were tested. As mentioned in chapter 2, $FeTeO_x$ films grown on MgO substrate show much better superconducting properties compared to the films grown on other oxide substrates. Therefore next a superconducting sample grown on MgO substrate was studied.

Here in addition to protecting samples from higher energy x-ray beam extra precaution was taken to prevent the overheating of the sample. In between the incoming x-ray beam and the sample several layers of Aluminum foil were used. To minimize the time x-ray beam interacted with the sample, the x-ray beam was allowed to interact with the sample only when taking the data. While the sample was warming the x-ray beam was not allowed to interact with the sample. In the cryostat a small heating rate was used to heat the sample to prevent overheating of the sample.

First the sample was aligned to observe (1 1 6) peak and (1 0 6) peak at 1.5 K. Then data scans were taken for above Bragg reflections in longitudinal theta/2 theta direction, L direction and H direction at the temperatures, 1.5 K, 5.0 K, 10.0 K, 15.0 K, 20.0 K and 70 K. The aim of this experiment was to track down any structural transitions associated with superconductivity below the superconducting transition temperature.

The temperature evolution of the (1 0 6) Bragg reflection in the longitudinal theta/two-theta direction is shown in figure 4-9.

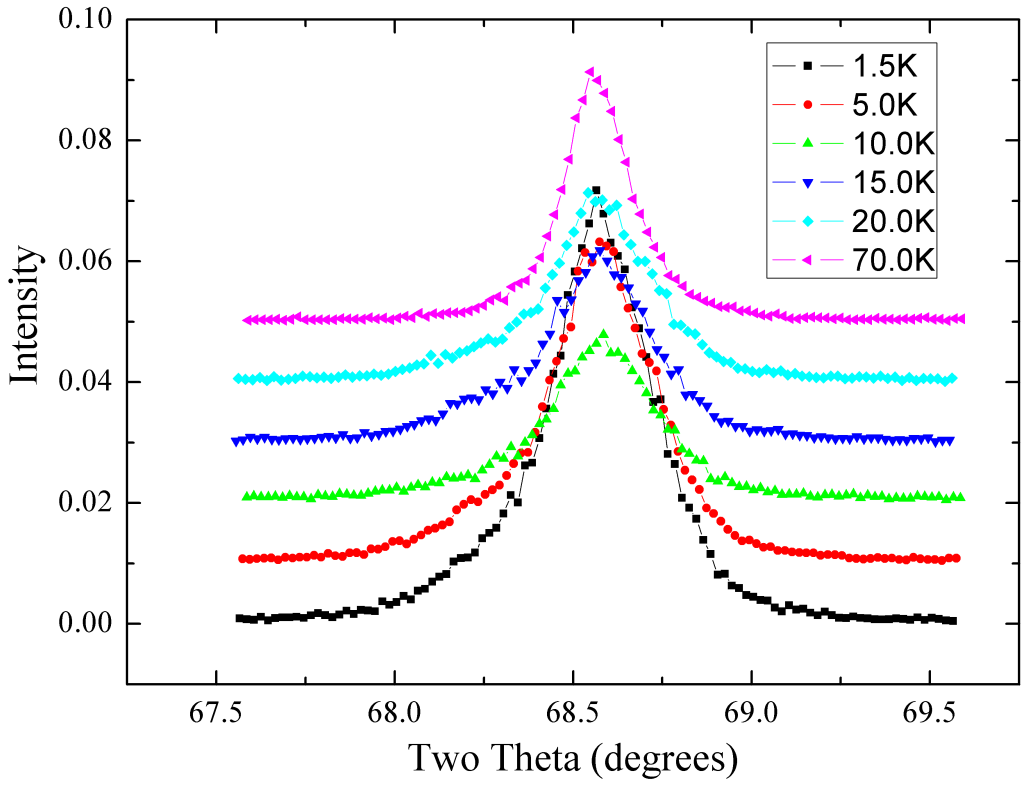

Figure 3-9 Temperature evolution of the tetragonal (1 0 6) Bragg peak in longitudinal theta/two-theta direction. The single peak, which represents the high temperature tetragonal phase at 70 K, splits into two peaks at lower temperatures.

The data scans of (1 0 6) Bragg reflection in theta/two-theta direction at temperatures below 20 K seem like single peaks by first appearance as shown in figure 4-10(a). But when the data scan is fitted, as a single peak the fitted curve is not accurate as shown by figure 4-10(b). More accurate fitting results can be obtained when the data scan is fitted as an overlap of two peaks as shown in figure 4-10(c).

At 70 K, (1 0 6) theta/two-theta data scan shows a single peak representing the tetragonal phase. At temperatures 20 K and 15 K (1 0 6) peak in theta/two-theta direction splits into two peaks. At 1.5 K, a temperature well below the superconducting transition temperature no further

splitting of peaks could be observed. A similar temperature evolution could be seen for (1 0 6) peak in H direction as shown in figure 4-11.

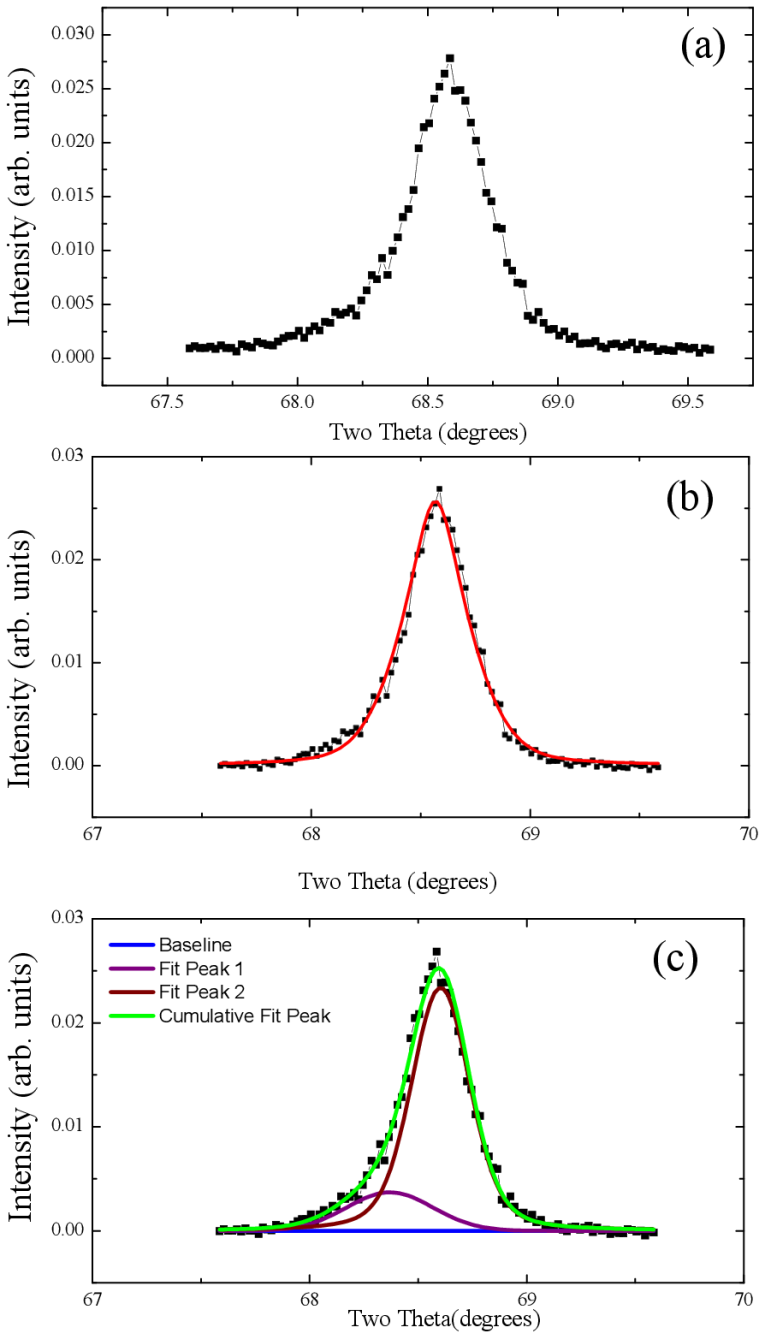

Figure 3-10 The (1 0 6) Bragg reflection in the theta/two-theta direction observed at 10 K. Fig. (a) The raw data scan. (b) The data scan is fitted as a single peak by a Voigt function (c) Data scan is fitted as an overlap of two peaks, a Gaussian(left peak) and a Voigt function(right peak).

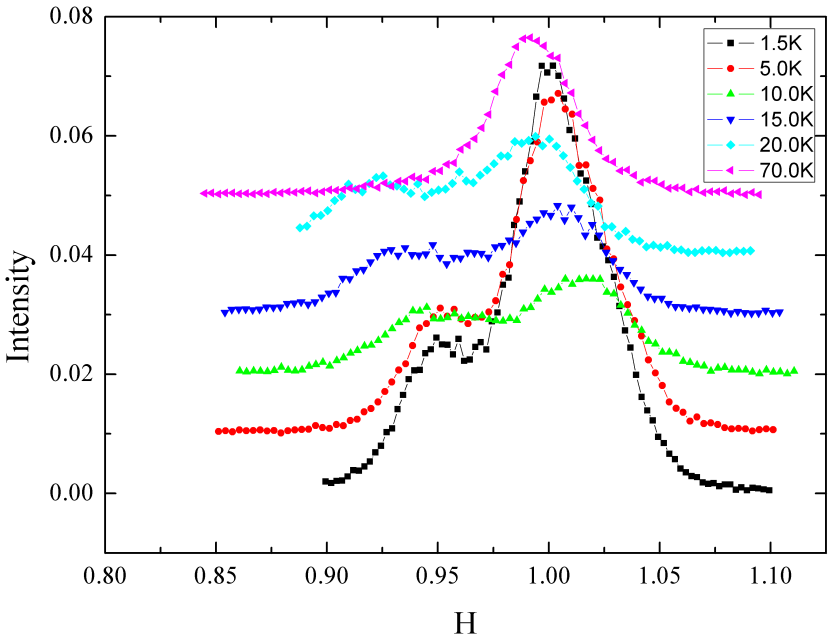

Figure 3-11 Temperature evolution of the tetragonal (1 0 6) Bragg peak in H direction. The single peak, which represents the high temperature tetragonal phase at 70 K, splits into two peaks at a lower temperature.

The temperature evolution of (1 0 6) Bragg reflection in L direction is shown in figure 4-12. For all temperatures the data scans could be fitted accurately by a Voigt function as a single peak as shown in figure 4-13. The temperature evolution of the (1 0 6) peak in theta/two-theta direction and H direction shows that the single peak which represents the high temperature tetragonal phase at 70 K splits into two peaks below 65 K . At a temperature well below the superconducting transition temperature no further splitting is observed. This indicates that the phase below the superconducting transition temperature can be either orthorombic or monoclic.

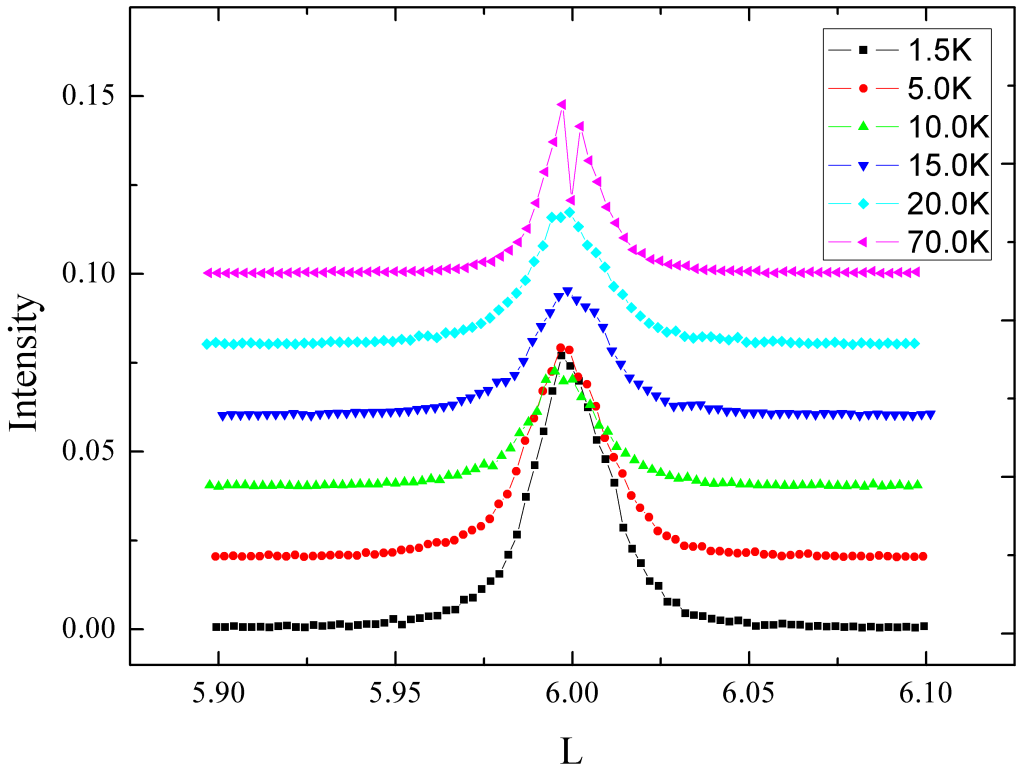

Figure 3-12 Temperature evolution of the tetragonal (1 0 6) Bragg peak in L direction. No peak splitting could be observed at lower temperatures.

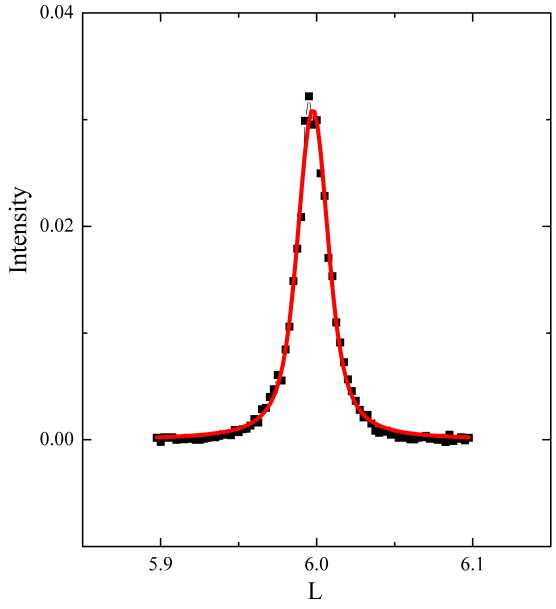

Figure 3-13 The (1 0 6) Bragg reflection in the L direction observed at 10 K. The data scan is fitted by a Voigt function as a single peak

Since it is possible for the low temperature crystal structure of superconducting $FeTeO_x$ to be orthorombic or monoclinic the temperature evolution of (1 1 6) peak was studied to identify the exact phase $FeTeO_x$ in supercondcting state. For an orthorombic structure the (1 1 6) peak does not split into two peaks but for a monoclinic structure it does.

The temperature evolution of the (1 1 6) peak in the longitudanal theta/two-theta direction, H direction and L direction are shown in figure 4.14. In all three figures at 70 K a single peak could be seen which represents the high temperature tetragonal phase. At a temperature below 65 K, peak splits into two and at a temperature well below the supeconducting transition temperature no further splitting could be observed. The two peaks can be labeled as (1 1 6) and (1 1 -6) in accordance with the low temperature monoclinic structure of the parent FeTe compound.

Since both (1 0 6) peak and (1 1 6) peak split into two peaks at a temperature below the superconducting transition temperature we concluded that the phase of $FeTeO_x$ at superconducting state is monoclinic.

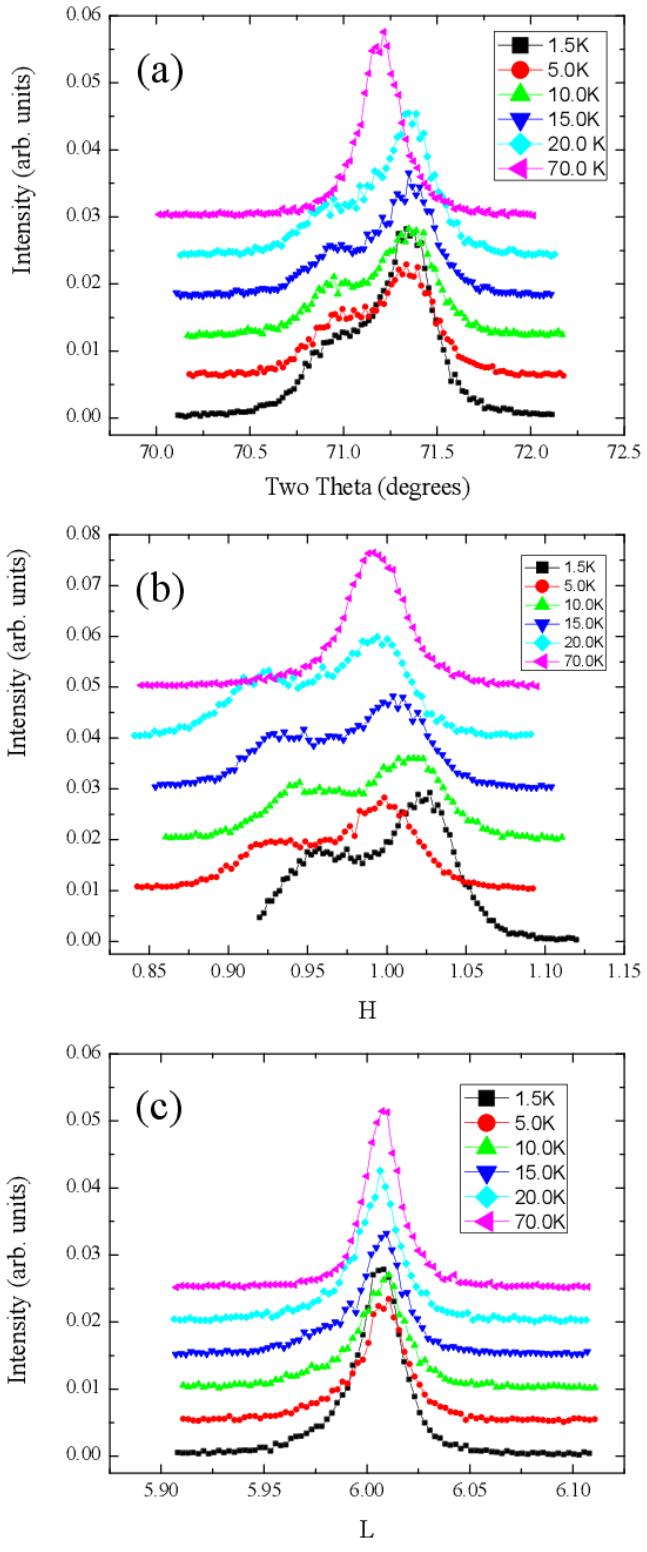

Figure 3-14 The temperature evolution of the (1 1 6) Bragg reflection in (a) longitudinal theta/two-theta direction (b) H direction (c) L direction .The single peak which represents the tetragonal phase at 70 K splits into two peaks at lower temperatures.

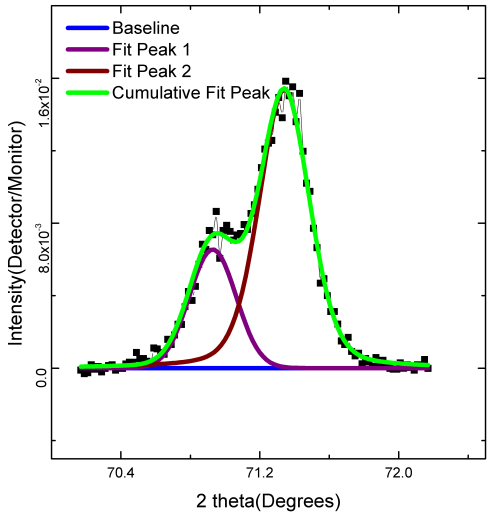

Figure 3-15 (1 1 6) Bragg reflection in longitudinal theta/two-theta direction observed at 10 K. The data scan is fitted as an overlap of two peaks, left hand side peak by a Gaussian and right hand side peak by a Voigt function. The blue solid line represents the background.

To check whether there are any subtle changes in the split peaks in the superconducting state compared to the monoclinic phase below 65 K a careful study was carried out. For each data scan the peaks were fitted with Gaussian and Voigt functions as shown in figure 4-15, such that the error associated with fitting is minimized. Then for each fitted peak, the intensity, the position of the peak, the full width at half maximum of the peak (FWHM) and area under the peak were calculated. These four parameters obtained for each data scan are summarzed w.r.t. temperature as shown in figures 4-16 through 4-21. In summarized information L represents the data points for left hand side peak and R represent the data points for right hand side peak. In crystallographic notation L and R represent (1 1 -6) and (1 1 6) peaks for (1 1 6) Bragg reflection and (1 0 6) and (1 0 -6) peaks for (1 0 6) Bragg reflection in accordance with the low temperature monoclinic structure of the parent FeTe compound. Next three pages contain the full data set for (1 1 6) peak followed by another three pages of data for (1 0 6) peak.

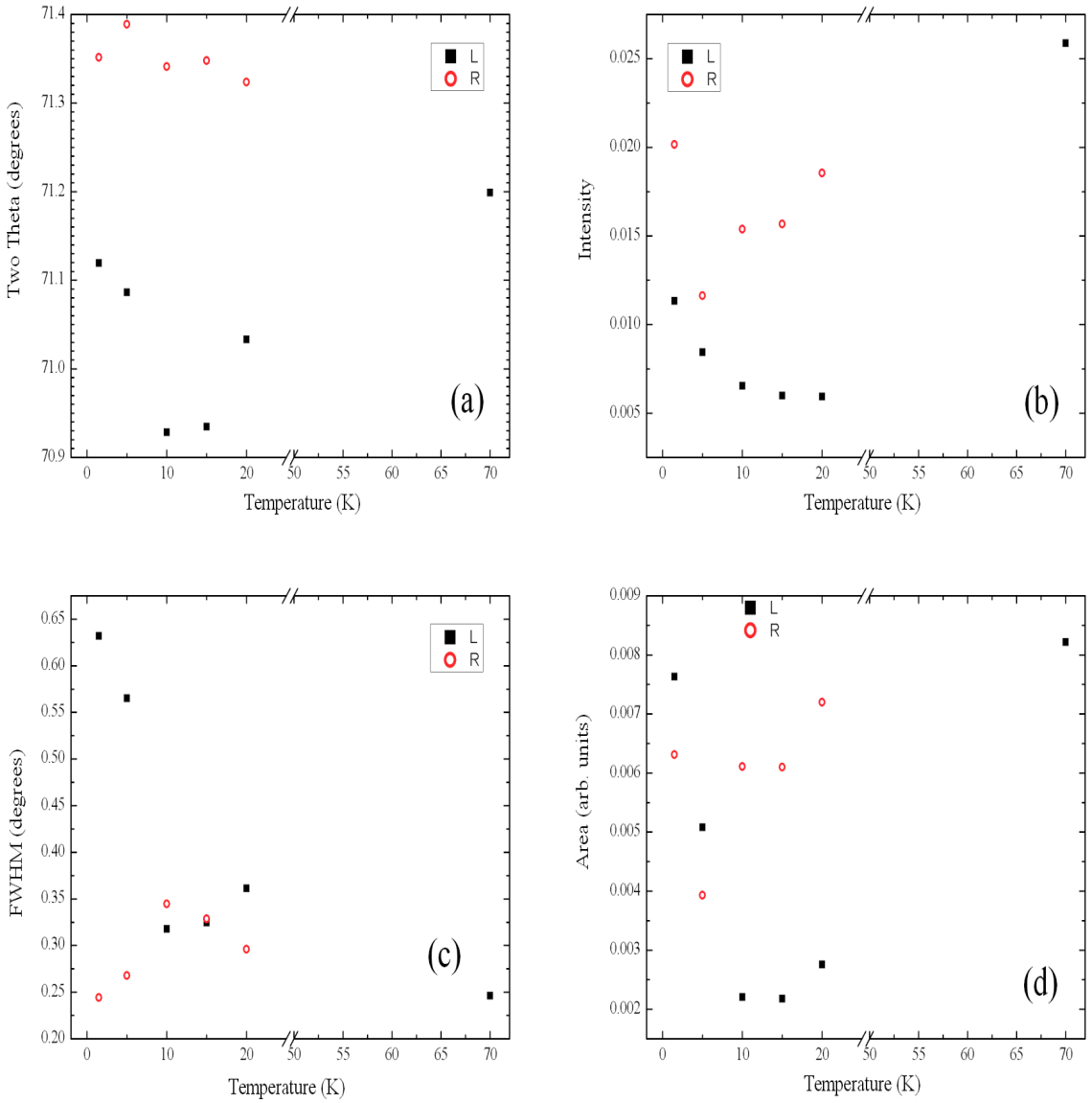

Figure 3-16 Temperature dependent variation of (1 1 6) and (1 1 -6) Bragg reflection in longitudinal theta/two-theta direction, (a) In position (b) In intensity (c) In FWHM (d) In area for superconducting $FeTeO_x$ film grown on MgO substrate.

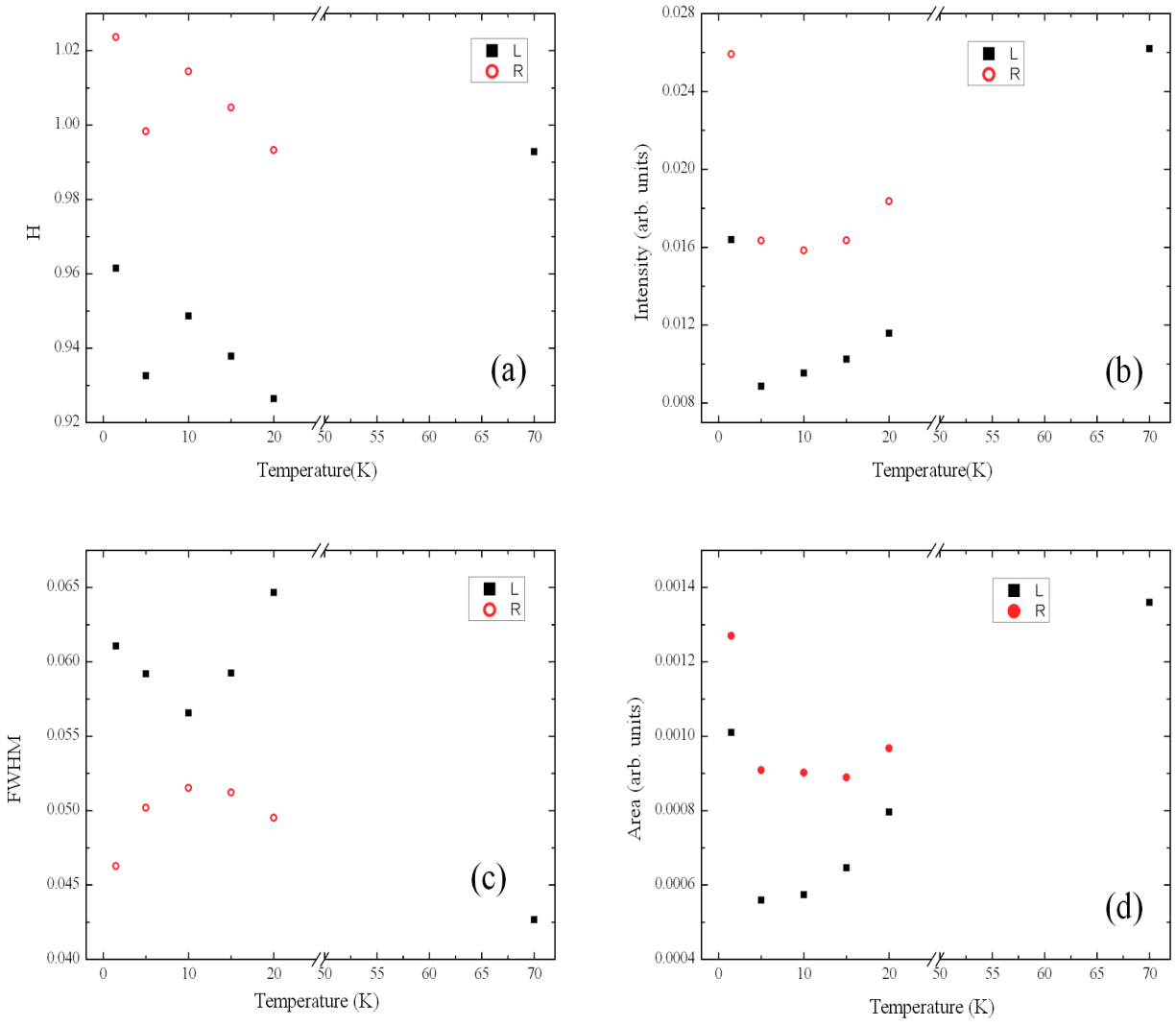

Figure 3-17 Temperature dependent variation of (1 1 6) and (1 1 -6) Bragg reflection in H direction, (a) In position (b) In intensity (c) In FWHM (d) In area for superconducting $FeTeO_x$ film grown on MgO substrate.

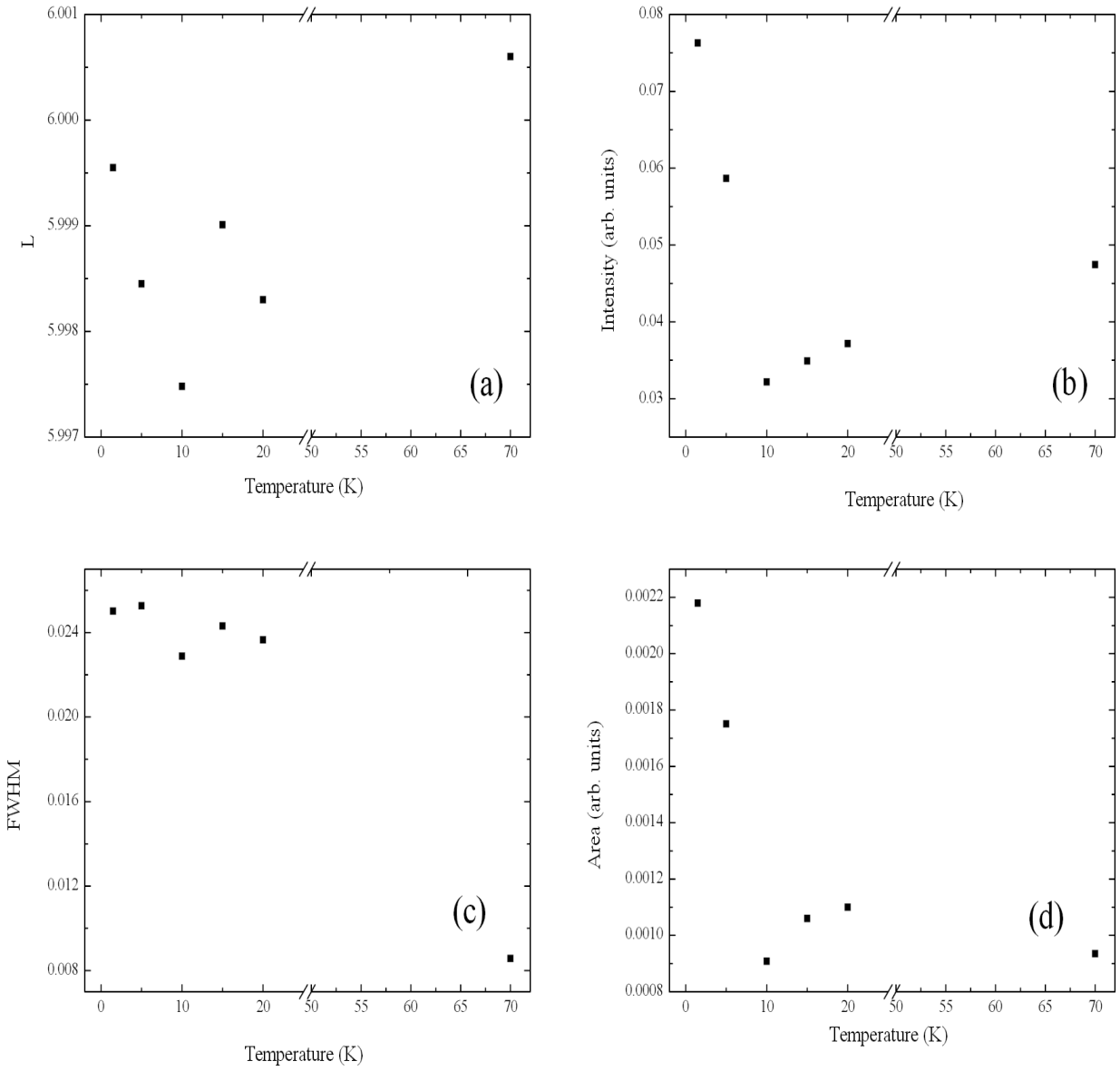

Figure 3-18 Temperature dependent variation of (1 1 6) and (1 1 -6) Bragg reflection in L direction, (a) In position (b) In intensity (c) In FWHM (d) In area for superconducting $FeTeO_x$ film grown on MgO substrate.

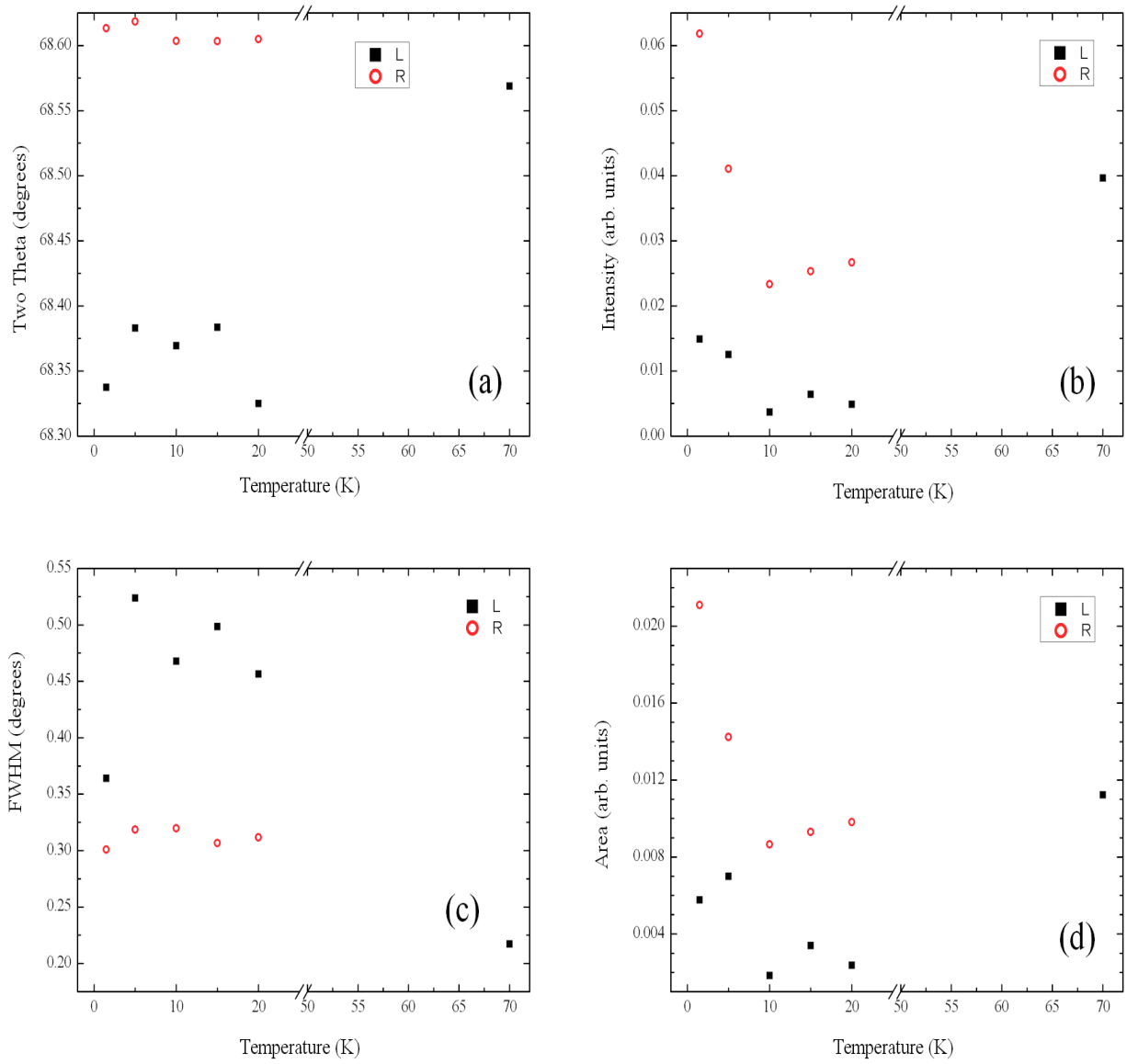

Figure 3-19 Temperature dependent variation of (1 0 6) and (1 0 -6) Bragg reflection in longitudinal theta/two-theta direction, (a) In position (b) In intensity (c) In FWHM (d) In area for superconducting $FeTeO_x$ film grown on MgO substrate.

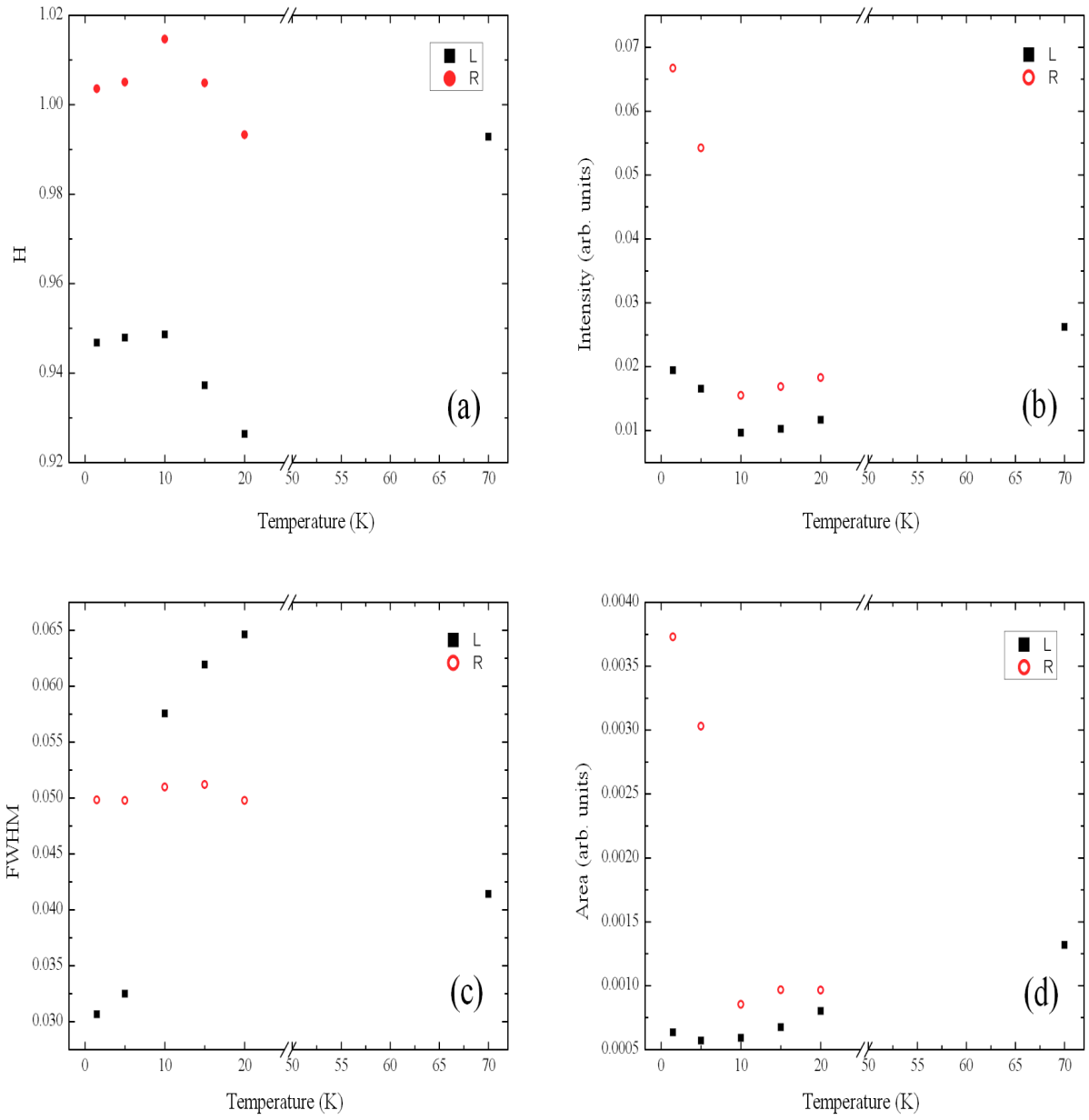

Figure 3-20 Temperature dependent variation of (1 0 6) and (1 0 -6) Bragg reflection in H direction, (a) In position (b) In intensity (c) In FWHM (d) In area for superconducting $FeTeO_x$ film grown on MgO substrate.

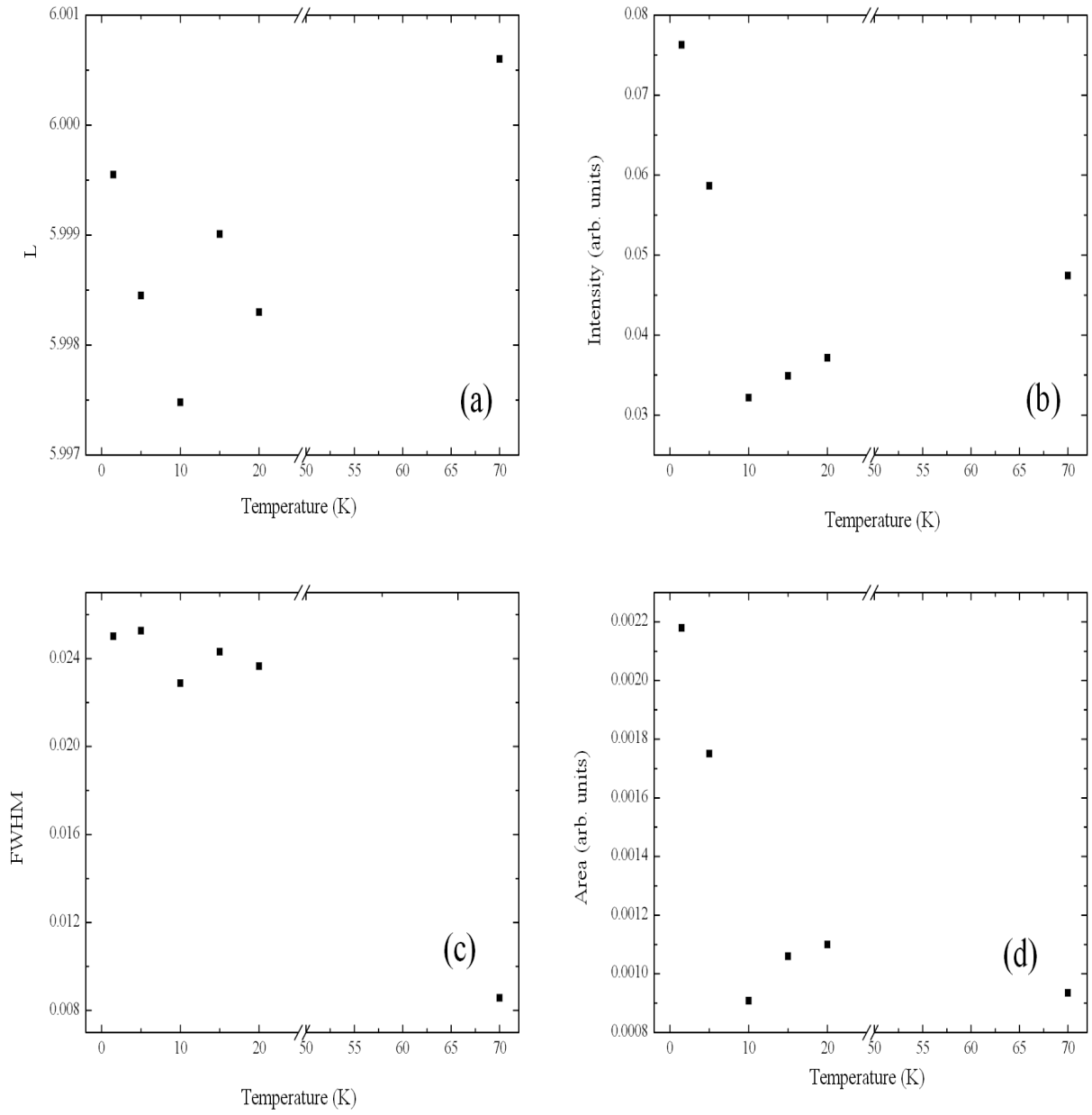

Figure 3-21 Temperature dependent variation of (1 0 6) reflection in L direction, (a) In position (b) In intensity (c) In FWHM (d) In area for superconducting $FeTeO_x$ film grown on MgO substrate.

Variation of intensity of peaks w.r.t temperature in theta/two-theta, H and L directions for (1 1 6) peak indicates that the intensity of right hand side peak goes to a maximum value at 1.5 K and goes to a minimum value at 10.0 K in the low temperature range(1.5 K-20.0 K). The intensity of right hand side peaks w.r.t temperature in two-theta and H directions for (1 0 6) peak

shows a clear increase in intensity at lower temperatures. At 1.5 K intensity is maximum and at 10.0 K intensity is minimum. Currently it is not clear whether these variations are an experimental artifact or a feature inherent to this particular sample or a feature inherent to superconducting $FeTeO_x$ films in general.

In order to find how the c-axis lattice parameter changes with temperature in this film grown on MgO substrate the temperature evolution of the $FeTeO_x$ (0 0 4) Bragg reflection was studied. Figure 4.18 shows a 'zoomed in' image of a partial theta/two-theta data scan of a (0 0 7) Bragg reflection and a (0 0 4) Bragg reflection.

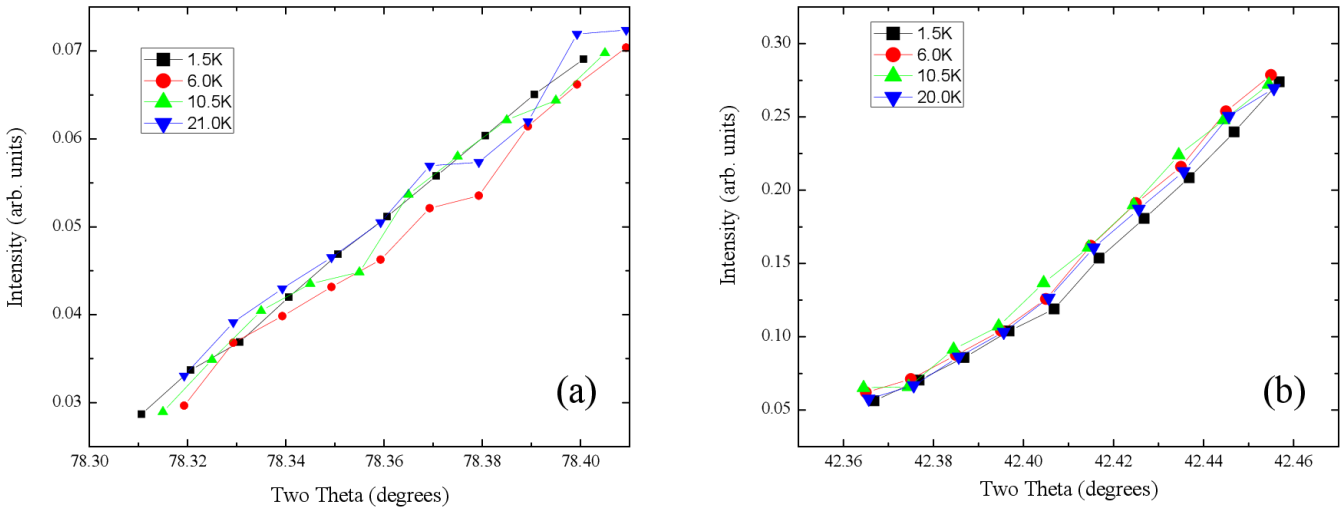

Figure 3-22 Zoomed in image of four temperature scans of (007) Bragg reflection in longitudinal theta/two-theta direction (a) (007) Bragg reflection (b) (004) Bragg reflection

In figure 4-22(b) a shift can be seen in $FeTeO_x$ (0 0 4) Bragg reflection in two-theta direction even though the shift is very small. But for $FeTeO_x$ (0 0 7) Bragg reflection the data scans are noisy and a clear shift cannot be observed. Therefore considering the combined effect of photon energy, resolution and intensities of the peaks in this experiment, $FeTeO_x$ (0 0 4) can

be considered as a better peak compared to $FeTeO_x$ (0 0 7) peak to identify any shift in two theta direction, hence to identify any change in the lattice parameter w.r.t. temperature.

The temperature evolution of the c-axis lattice parameter calculated using the $FeTeO_x$ (0 0 4) Bragg reflection in longitudinal theta/two-theta direction is shown in figure 4-23. The theta/two-theta data scans were fitted with a Voigt function.

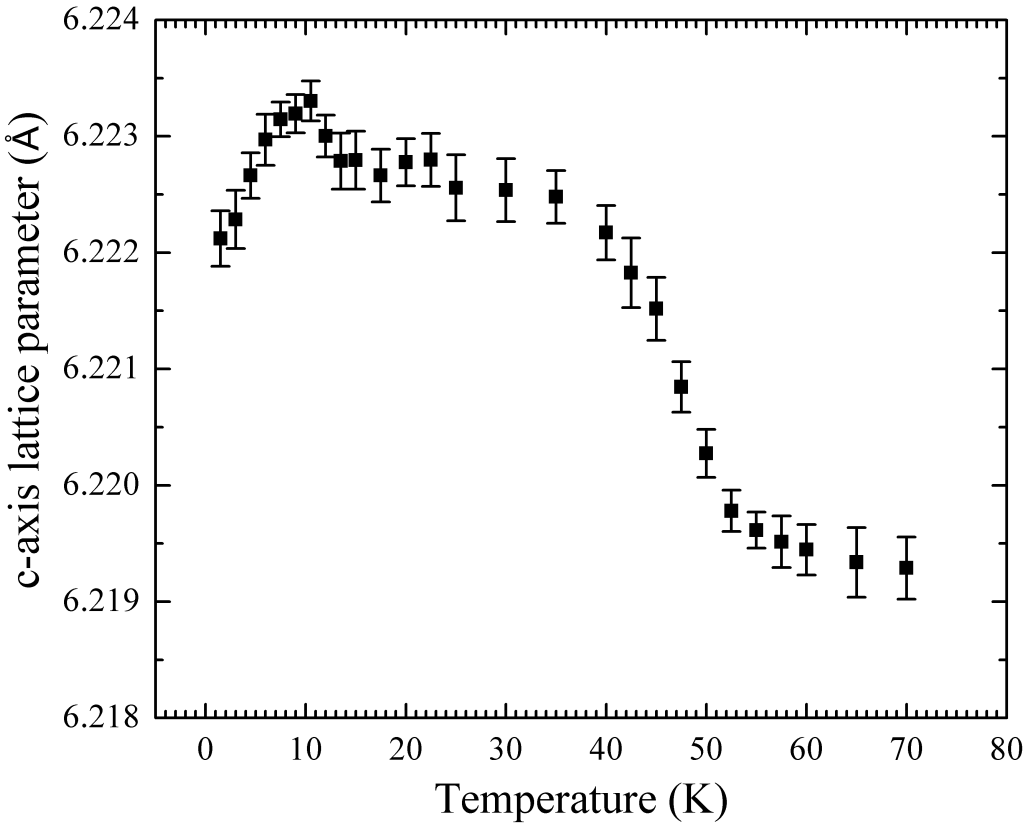

Figure 3-23 Temperature evolution of the c-axis lattice parameter calculated using the (0 0 4) Bragg reflection in longitudinal theta/two-theta direction

Compared to the previous superconducting thin films tested so far, in this superconducting sample a clear decrease in the c-axis lattice parameter could be seen at the vicinity of superconducting transition. One reason to get clear data is the use of (0 0 4) structural peak instead of (0 0 7) structural peak to obtain the c-axis lattice parameters. The other reason is the better crystalline quality of the $FeTeO_x$ film grown on MgO compared to a $FeTeO_x$ film

grown on $SrTiO_3$. The absolute change in the c-axis ($C_{10.5\,K} - C_{1.5\,K}$) is larger than the error bars associated with each data point. In addition in the temperature range from 14 K to 10.5 K a small increase in c-axis could be observed. The change in c-axis around 60 K at the vicinity of the structural transition couldn't be clearly observed in this particular data run due to a technical problem in the heater used in the cryostat. Due to the small heating rate used to protect the sample from over-heating, the sample couldn't achieve the higher temperatures. Anyway as described previously the structural transition associated with this sample around 60 K was well-established using (1 1 6) and (1 0 6) Bragg reflections. There may also be subtle changes in a- and b- axis lattice parameters in superconducting state but they are difficult to measure in thin films in reflection geometry.

In order to check the superconductivity of this sample after exposing to the x-ray beam the resistance of this superconducting $FeTeO_x$ film grown on MgO substrate was measured. The temperature dependent resistance of the sample before and after the beam exposure is shown in figure 4-24.

Even after the full exposure of the x-ray beam to the sample, sample was still superconducting and zero resistance was observed. Therefore it can be considered that the sample is more stable and enough oxygen remains in the film to make it superconducting even after the full exposure of x ray beam.

In order to examine whether the decrease in c observed in the above sample at the vicinity of superconductivity is a property inherent to superconducting $FeTeO_x$ the temperature evolution of the c-axis lattice parameter of a non-superconducting FeTe single crystal was studied.

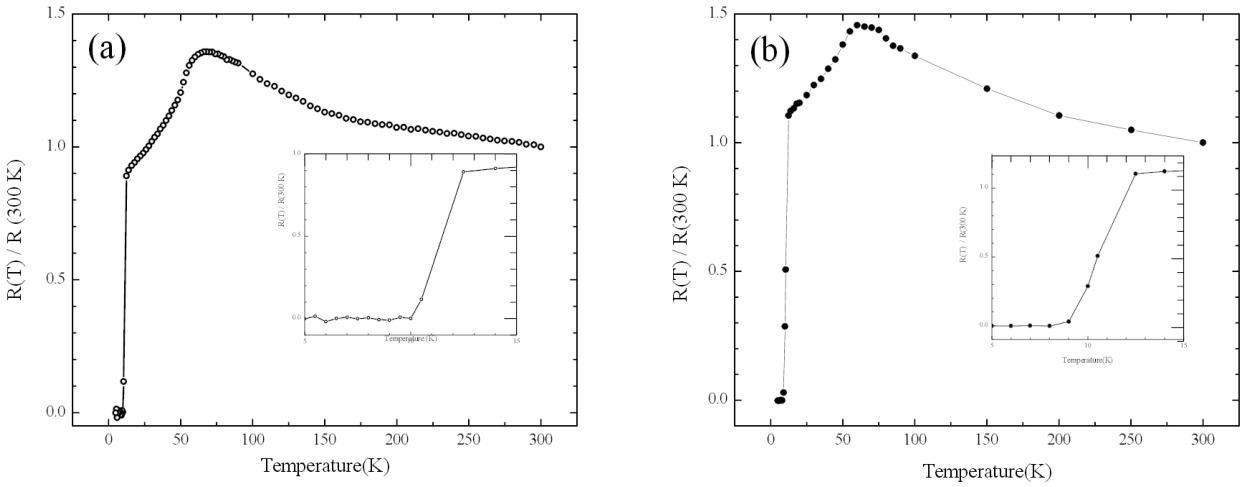

Figure 3-24 Temperature dependent resistivity of the third superconducting sample tested, $FeTeO_x$ grown on MgO substrate, (a) Before exposure to the higher-energy x-ray beam (b) After exposure to the higher-energy x-ray beam.

The single crystal was aligned to observe (0 0 4) Bragg reflection in longitudinal theta/two-theta direction at 1.5 K and the temperature dependent data scans were observed from 1.5 K to 120 K. Data scans were fitted by Gaussians as shown in figure 4-25. The temperature evolution of the theta/two-theta data scans at lower temperature range is shown in figure 4-26. Unlike that of the superconducting sample these scans doesn't show any shift in two-theta direction. These peaks are narrower compared to the data scans obtained for superconducting thin films. This indicates the better quality of the single crystal compared to the thin films. The temperature evolution of the c-axis lattice parameter calculated using the above data scans is shown in figure 4-27.

The c-axis lattice parameter remains almost as a constant in the lower temperature range for the non-superconducting single crystal. The change in c-axis lattice parameter observed around 60 K at the vicinity of the structural transition is much sharper compared to that of superconducting thin films.

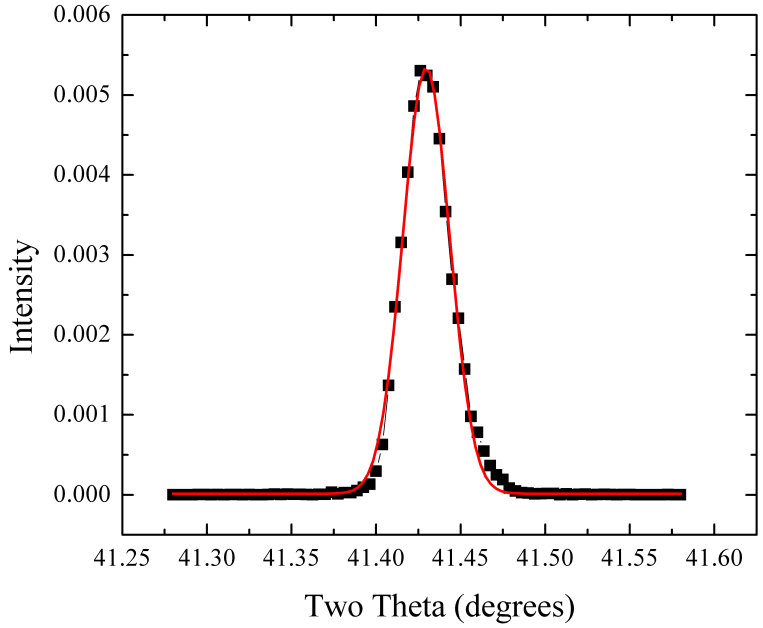

Figure 3-25 Bragg reflection (0 0 4) in the longitudinal theta/two-theta direction observed at 10.5 K for the non-supercondcuting single crystal. The data scan is fitted by a Gaussian.

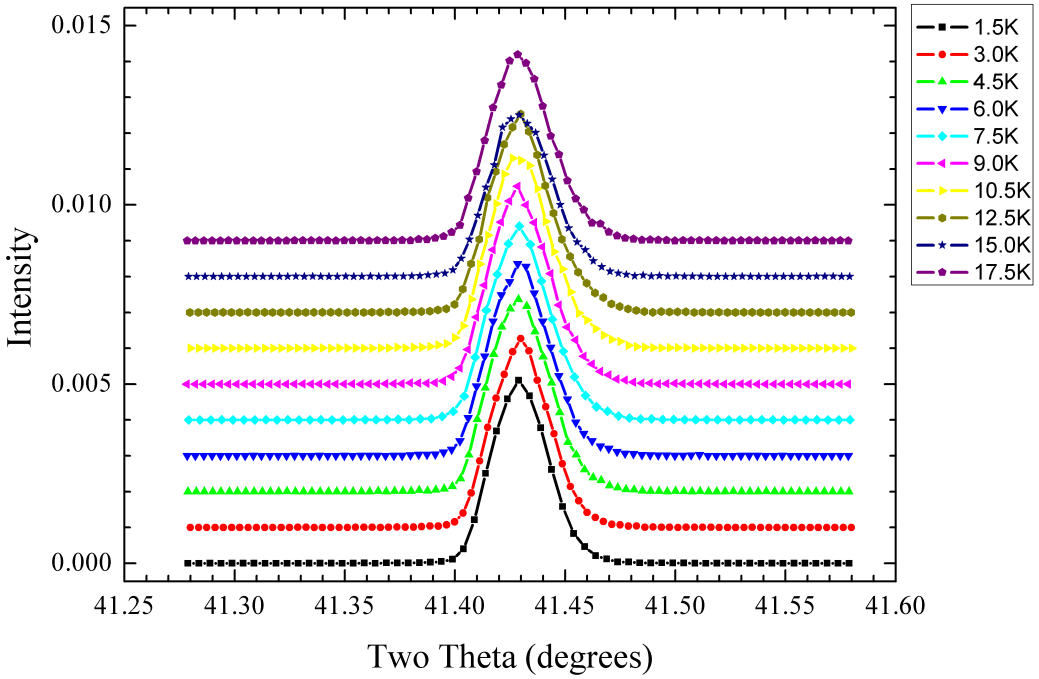

Figure 3-26 Temperature evolution of the Bragg reflection (0 0 4) in the longitudinal theta/two-theta direction observed for the non-superconducting single crystal.

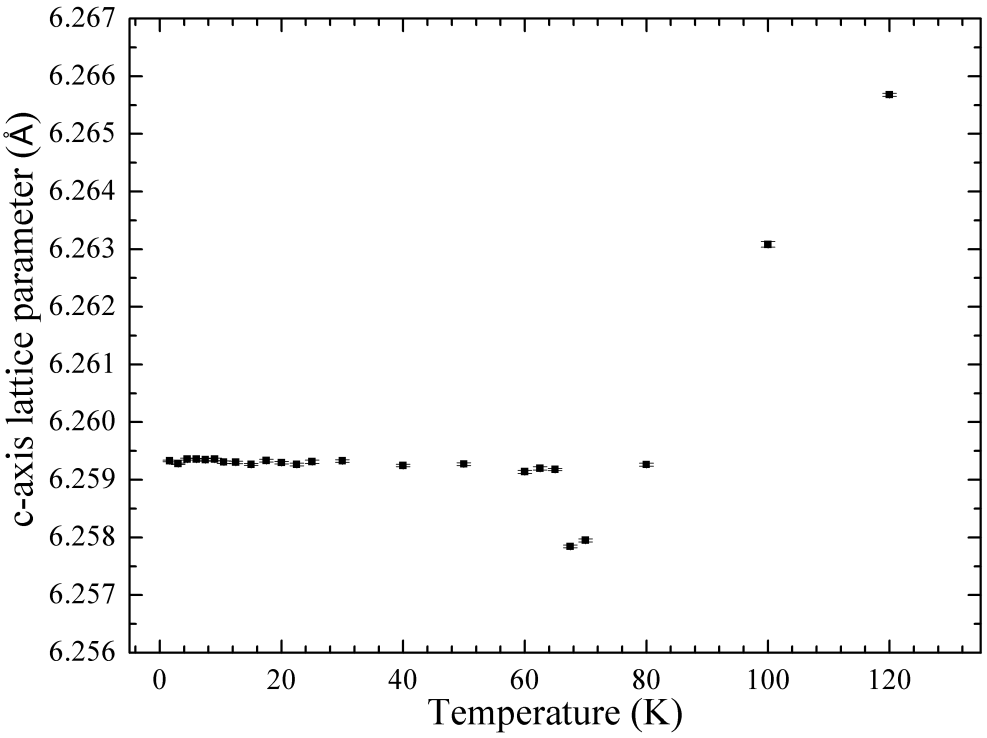

Figure 3-27 Temperature evolution of the c-axis lattice parameter calculated using the (0 0 4) Bragg reflection in longitudinal theta/two-theta direction for non-superconducting FeTe single crystal

In figure 4-28 the temperature evolution of c-axis lattice parameter observed in superconducting $FeTeO_x$ film is compared to that of the non-superconducting single crystal. For the superconducting film the absolute change in c-axis lattice parameter below 10.5 K ($C_{10.5\ K} - C_{1.5\ K}$) is 0.0012 Å ± 0.0002 Å. For the non-superconducting single crystal the c-axis lattice parameter at low temperature remains almost a constant with a variation less than 9×10^{-5} Å ± 1.5×10^{-5} Å. This behavior of the c-axis lattice parameter of FeTe is consistent with the result reported by Xiao.[60] The error bars associated with the non-superconducting single crystal is smaller compared to that of superconducting thin film due to both better statistics and a narrower peak related with better homogeneity. Both properties are inherent with single crystals compared to films.

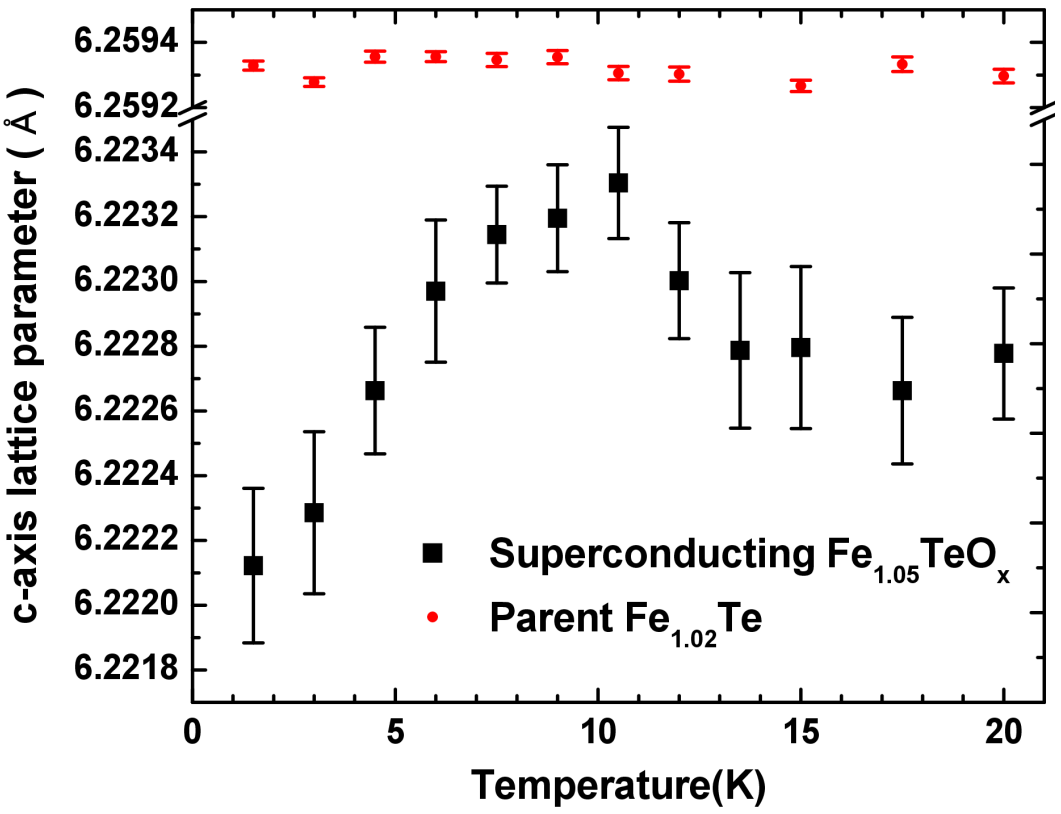

Figure 3-28 c-axis lattice parameter calculated using (0 0 4) Bragg reflection vs. temperature for a superconducting film (black solid squares) and for a non-superconducting single crystal (red solid circles).

3.4 Conclusion

We conclude that the large decrease in c-axis lattice parameter observed in superconducting $FeTeO_x$ film at the vicinity of superconducting transition is associated with the superconductivity of $FeTeO_x$. There are three observations that support the above statement: (1) the temperature where c-axis lattice parameter starts to change coincides with the superconducting transition temperature; (2) the change in c axis lattice parameter is only present in the superconducting sample; (3) we detect only a shift in the diffraction peak, not a broadening.

In general, this sort of change in lattice parameter measured by x-ray diffraction is not observed in superconductors. In the Fe-based superconductors structural transitions are

commonly observed above the superconducting transition temperature and they are associated with a change in crystallographic phase.[25,26] In contrast, $FeTeO_x$ doesn't show any change in symmetry compared to parent FeTe but only a sudden change in the temperature evolution of the lattice parameter setting in at the onset of superconductivity.

This behavior of the c-axis lattice parameter is quite similar to the lattice parameter changes reported in other iron-based superconductors[54–58] as well as in cuprates[59] using sensitive dilatometry technique. In these reports the change in lattice parameters at the vicinity of superconductivity is considered as a thermodynamic effect that requires a change in thermal expansivity. This kind of a discontinuity in thermal expansion is common to a normal to superconducting second order phase transitions. The main difference between other reports and our data is that in $FeTeO_x$, the change in lattice parameter is much larger allowing it to be seen in diffraction. To compare our data with the data reported in dilatometry literature the change in c-axis lattice parameter is shown as a relative change w.r.t temperature in figure 4-29. Based on figure 4-29, the calculated thermal expansivity w.r.t temperature is shown in figure 4-30. The discontinuity in thermal expansion at the superconducting transition temperature is approximately $8x10^{-5}K^{-1}$, about 10 times higher than the values shown for other Fe-based superconductors.[55]

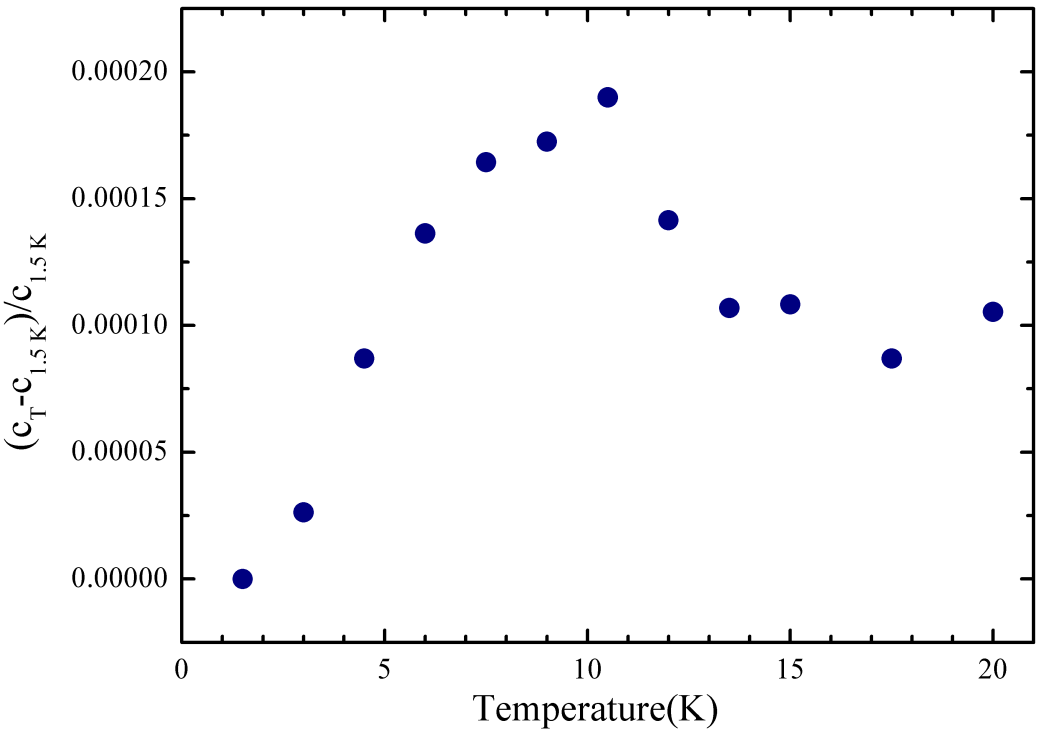

Figure 3-29 Fractional change in c-axis lattice parameter w.r.t. temperature calculated based on the change of c is figure 4-28.

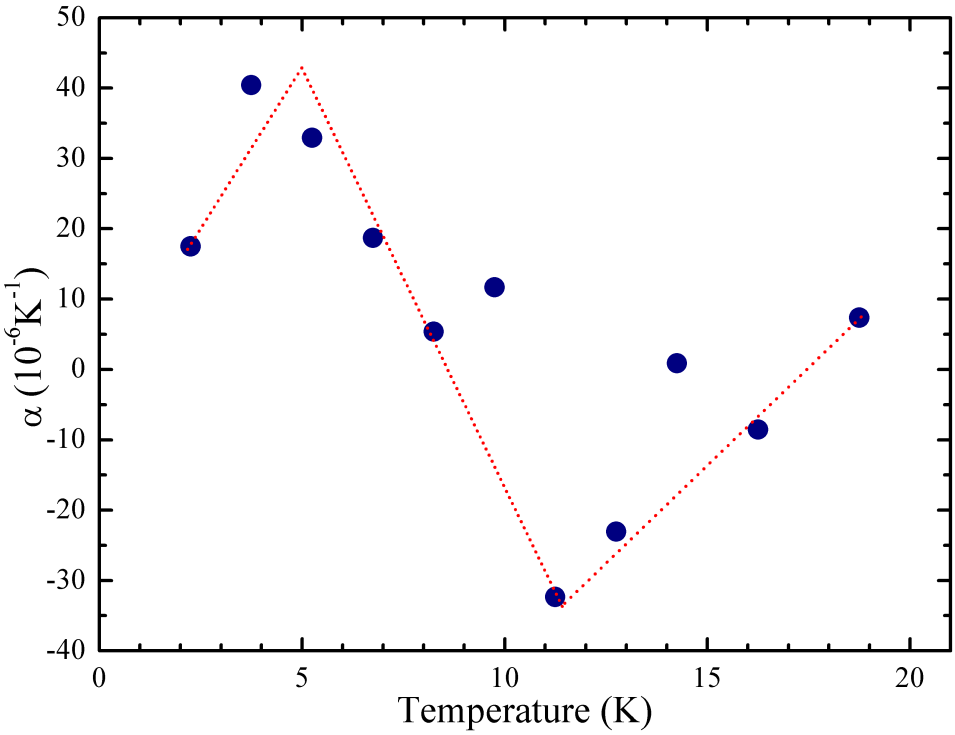

Figure 3-30 Thermal expansivity w.r.t temperature calculated based on the fractional change of c shown in figure 4.29 for a superconducting $FeTeO_x$ film.

As described in the introduction section of this chapter, Ehrenfest equation describes the thermodynamic relations between specific heat and derivatives of specific volume in second order phase transitions. These equations can be adopted to describe a relationship between the uniaxial pressure dependence of superconducting transition temperature, $\frac{dT_c}{dP_i}$, the discontinuity in specific heat at the phase transition ΔC_p and the discontinuity in thermal expansion at the phase transition $\Delta\alpha_i$ for a second order normal to superconducting phase transition as follows.[59]

$$\frac{dT_c}{dP_i} = V_m \frac{\Delta\alpha_i}{\Delta C_p / T_c}$$

The quantities needed to predict the dependence of T_c on uniaxial pressure along c-axis direction are the molar volume, the discontinuity in the thermal expansivity, and the discontinuity in the heat capacity. The molar volume is calculated from our structural studies to be 53.5cm^3/mol.[21] The discontinuity in the c-axis expansivity comes from the data of Figure 4.30 and is $8x10^{-5}K^{-1}$. We don't have the temperature dependent heat capacity of superconducting $FeTeO_x$, and determining the discontinuity in heat capacity in a film is difficult. In order to obtain an approximate value for $\frac{dT_c}{dP_i}$, we can use heat capacity of a related material with a similar T_c (as ΔC_p is known to vary with T_c),[61,62] and a similar layered structure. We believe that the best choice is the related superconductor $FeTe_{0.5}Se_{0.5}$, with the same basic crystal structure as $FeTeO_x$ and a similar T_c of 13.5 K.[23,24] Values of the discontinuity in heat capacity either reported or derived from published data for superconducting $FeTe_{0.5}Se_{0.5}$ range from 725 to 187 $mJmol^{-1}K^{-1}$.[54,63] Substituting the values listed leads us to predict a uniaxial pressure dependence of T_c of $\frac{dT_c}{dP_{c-axis}}$ = 43 to 160 K/GPa. The entire range is quite large compared to predicted values of

$\frac{dT_c}{dP_{c-axis}}$ in other iron-based superconductors, which typically range from 1 to 27 K/GPa in magnitude.[54,55] This is consistent with the fact that the observed change in c-axis lattice parameter is quite large compared to other reports in dialotametry literature.

Recently the effect of pressure on superconducting transition temperature in iron-based compounds has been experimentally measured using direct hydrostatic pressure.[27–31] But these measurements are not in good agreement with the predictions done using Ehrenfest relation[54–58] due to two major reasons. One of them is only individual uniaxial data can be obtained using the Ehrenfest prediction, which cannot directly apply to the isotropic pressure condition. Another reason is that performing hydrostatic pressure experiments on thin films is technically difficult. However by introducing strain during growth the pressure dependence of T_c on thin films can be tested. In films, the in-plane and out-of-plane strains are of different sign due to the Poisson ratio. Meingast used the in-plane/out-of-plane uniaxial expansivities predicted by Ehrenfest relation in the cuprates to explain the large changes in T_c [59] that were measured in highly strained films of $La_{2-x}Sr_xCuO_4$.[64]

The much larger lattice change at T_c thus leads us to predict that much higher superconducting transition temperatures can be expected from $FeTeO_x$ films by applying compressive strain along c axis. In films, this can be achieved by uniformly growing $FeTeO_x$ on a substrate with a larger lattice constant leading to in-plane tensile strain and out-of-plane compression. Such uniform growth can only be achieved up to a critical film thickness, which depends on the lattice mismatch between film and substrate. This is typically only tens of nanometers. For $FeTeO_x$ it is difficult to grow this kind of a thin film because the films tend to show island-like growth instead of a uniform growth. As described in the chapter about growth

conditions we are conducting experiments to grow uniform thin films by changing growth parameters of pulsed laser deposition technique.

In addition to the fact that the change in c-axis lattice parameter being larger in $FeTeO_x$ compared to other reports on thermal expansivity of other compounds, another major difference we observe in our data is an initial upturn of the c-axis lattice parameter near the superconducting transition, followed by the downturn. This two-part variation is not reported in other reports of the thermal expansion changes at T_c. The upturn, which starts to occur at a temperature slightly above the onset of superconductivity, might possibly be the result of another transition such as a magnetic to a non-magnetic state, which might be a key towards allowing $FeTeO_x$ to become superconducting. A careful investigation of the magnetic structure of superconducting $FeTeO_x$ at low temperature is necessary to clarify the observed upturn in c-axis lattice parameter. In addition, growing $FeTeO_x$ films compressed along c-axis will enable us to check if the superconducting transition temperature can be changed according to the predicted value we found using Eherenfest relation.

3.5 Summary

We concluded that superconducting $FeTeO_x$ undergoes a structural transition from tetragonal to monoclinic around 65 K similar to the parent compound FeTe. For $FeTeO_x$ there is no further change in symmetry associated with superconductivity; both magnetic FeTe and superconducting $FeTeO_x$ are monoclinic at low temperature. In addition to the crystal structure, the temperature dependent resistivity of superconducting $FeTeO_x$ is also similar to FeTe except below the superconducting transition temperature. Preliminary neutron diffraction measurements also indicate that the antiferromagnetic order still exists in superconducting $FeTeO_x$ below 65 K similar to parent FeTe. Even though we have previously reported a large change in Fe valence

for $FeTeO_x$, above T_c, $FeTeO_x$ behaves very similar to parent FeTe. Thus oxygen acts as an interesting dopant, having only a small effect on structure and normal state properties yet inducing superconductivity.

There is an unexpectedly large decrease in c-axis lattice parameter of $FeTeO_x$ below T_c associated with the second order nature of normal-to-superconducting phase transition. While such a change in the lattice is a standard, thermodynamic phenomenon, the magnitude of the effect is large in $FeTeO_x$; large enough to be seen in x-ray diffraction. The Ehrenfest relation for a second order phase transition allows us to predict a uniaxial pressure derivative of the superconducting transition temperature, which is consistent with the large change in the c- axis lattice parameter, is also larger than similar predictions for other Fe-based superconductors. This prediction for a large uniaxial pressure dependence on T_c can be best tested in very thin, strained films of $FeTeO_x$.

4 Low temperature Magnetic Structure of Superconducting $FeTeO_x$ films

4.1 Background and Motivation

For iron-based superconductors the relationship between superconducting and magnetic phases is believed to be a key to their physics but remains a puzzle in many ways. Parent compounds of iron-based superconductors are antiferromagnetic and upon doping antiferromagnetism at least partially suppressed and superconductivity emerges at a higher doping level. As a function of doping, iron based compounds show at least three different kinds of transformations from magnetic phase to superconducting phase. This behavior is quite different from cuprates where the transformation from antiferromagnetism to superconductivity happens in a unique way. One transformation in iron-based compounds roughly matches the cuprates where first the magnetic phase is destroyed and at a higher doping level bulk superconductivity occurs. An example is $FeTe_{1-x}Se_x$ system. In contrast in $LaO_{1-x}F_xFeAs$ system there is a sharp boundary between magnetic and superconducting phases at $x = 0.45$. In the third case as a function of doping while antiferromagnetism is suppressed and superconductivity emerges at a higher doping level, there is a considerable doping range where both superconductivity and magnetism are observed. An example is the doped $BaFe_2As_2$ system. The exact relationship between these different cases is not clear.

It will be interesting to know the interplay between magnetism and superconductivity in $FeTeO_x$ system. The aim of this chapter will be to investigate how magnetism interacts and compete with superconductivity in $FeTeO_x$ system.

The temperature dependent resistivity of superconducting $FeTeO_x$ shows a peak around 65 K similar to parent FeTe indicating that antiferromagnetic transition can still exist in $FeTeO_x$. The low temperature x-ray diffraction studies reveal that $FeTeO_x$ shows a structural transition

from tetragonal to monoclinic around 65 K while below the superconducting state there is no change in crystal symmetry compared to the normal state. Both low temperature resistivity and low temperature crystal structure indicate that superconducting $FeTeO_x$ behaves similar to parent FeTe above the superconducting transition but at T_c $FeTeO_x$ undergoes a transformation, which favors superconductivity. One possibility is that superconducting $FeTeO_x$ has electronically phase separated regions, one magnetic and the other superconducting. Above T_c, $FeTeO_x$ could be dominated by the phase that favors magnetism and below T_c it could be dominated by the phase that favors superconductivity. Alternatively, the whole material may transform in subtle ways at T_c. Further understanding would come from the low temperature magnetic structure, particularly the evolution of the magnetism through the superconducting transition. Low temperature x-ray diffraction studies further revealed a change in c-axis lattice parameter at the vicinity of superconducting transition temperature. The downturn of the c-axis is associated with superconductivity and it is speculated that the upturn can be due to a magnetic to non-magnetic transition.

So far $FeTeO_x$, which shows bulk superconducting properties, has been only made in film form. In general antiferromagnetism is difficult to study in films because the total magnetic moment result from a small mass, which contains in a thin film is not large enough to interpret reliable magnetic properties. However techniques such as neutron diffraction and Mossbauer spectroscopy can be used to observe the antiferromagnetic order in thin films. Several approaches had been taken so far to study the low temperature magnetic structure of superconducting $FeTeO_x$ films. To study the average magnetic structure neutron diffraction has been used. Mossbauer spectroscopy has been used as a local probe to study the local magnetic moment around iron nucleus in superconducting $FeTeO_x$

4.2 Neutron Diffraction

4.2.1 Experimental Details

The aim of this experiment was to check whether there exists any antiferromagnetic transition in superconducting $FeTeO_x$ similar to parent FeTe and what happens to magnetism below the superconducting transition temperature. We were also interested in studying the antiferromagnetic transition in non-superconducting FeTe films and compare it with the data in literature for bulk FeTe.

Neutron diffraction experiment was carried out using the triple axis spectrometer in RITA-2 beam line at SINQ, Paul Sherrer Institute in Switzerland. The neutrons with energy 4.6 meV and wavelength 4.217 Å were used in the experiment. One superconducting sample grown on $SrTiO_3$ substrate and one non-superconducting reference sample grown on CaF_2 substrate were used. For this particular experiment, very thick films with thickness around 600 nm and area of 100 mm^2 were used. The antiferromagnetism of these films were studied first by aligning the samples to observe the magnetic Bragg reflection (1/2 0 1/2) and by measuring the temperature dependent intensity of the above Bragg reflection.

4.2.2 Results and Discussion

For the non-superconducting film grown on CaF_2 substrate first the FeTe film was aligned to find (1 0 1) structural peak then it was adjusted to find (1/2 0 1/2) magnetic peak. The theta scan of the (1/2 0 1/2) magnetic Bragg reflection observed at 20 K is shown in figure 5.1.

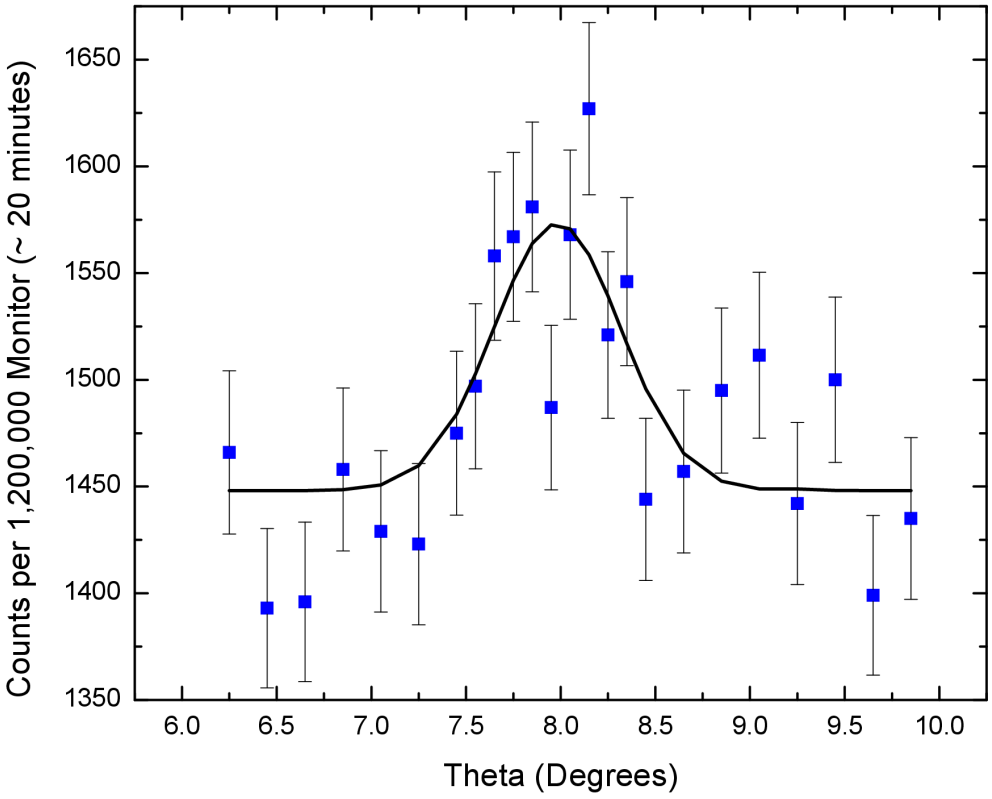

Figure 4-1 Theta scan of a (1/2 0 1/2) magnetic Bragg reflection of FeTe film grown on CaF_2 substrate observed at 20 K. The black solid line represents a Gaussian.

This magnetic peak was measured by varying the temperature from 10 K to 100 K in one point scans. Figure 5.2 shows the temperature dependent intensity of the (1/2 0 1/2) magnetic Bragg reflection. The peak disappears around 70 K indicating that antiferromagnetism sets in around 70 K similar to bulk FeTe. The black solid line in the figure is a guide to the eye representing the behavior of magnetic order parameter as a function of temperature. Below 70 K the magnetic order smoothly develops as a function of temperature.

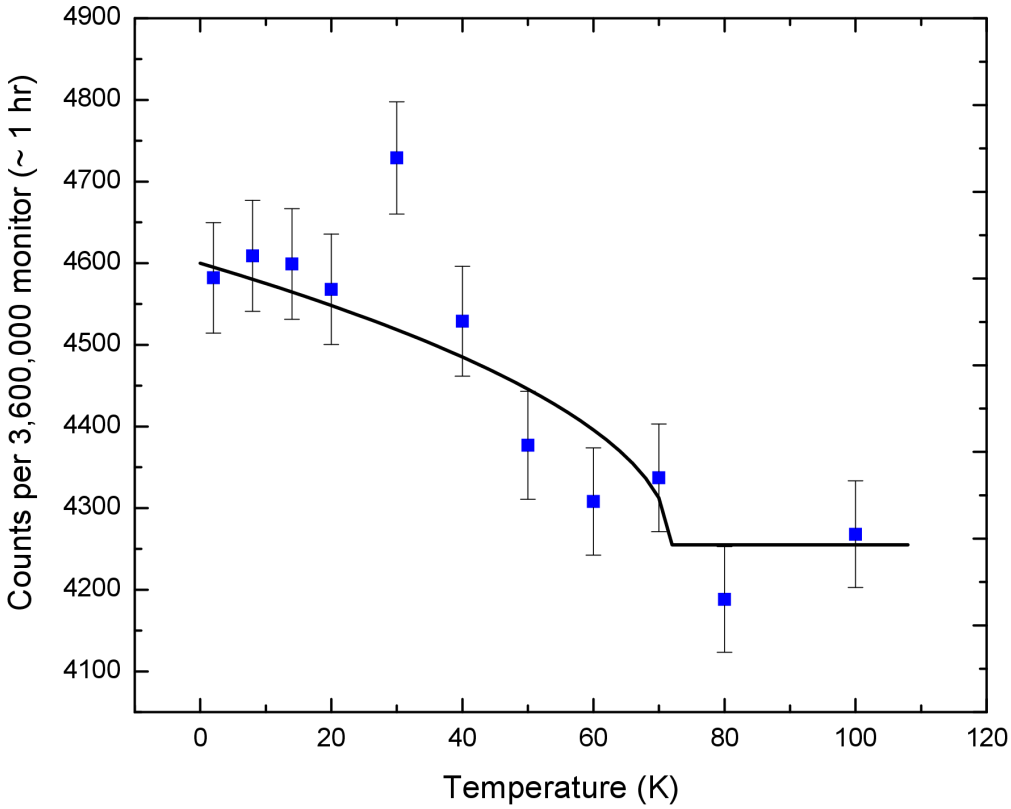

Figure 4-2 Temperature evolution of (1/2 0 1/2) Bragg reflection of FeTe film grown on CaF_2 substrate. The black solid line is a guide to the eye which represents the behavior of the order parameter as a function of temperature.

For the superconducting film grown on $SrTiO_3$ substrate first the $FeTeO_x$ film was aligned to find (1 0 1) structural peak. It was difficult to find the (1 0 1) structural peak hence (1/2 0 1/2) magnetic peak. It was assumed that the peaks were spread out too much due to the poor in-plane mosaic of the film grown on $SrTiO_3$ substrate. As explained in chapter 3, FeTe films grown on $SrTiO_3$ have strong c-axis texture compared to its in-plane orientation along the substrate. Therefore by observing a magnetic peak that has more contribution from c-axis compared to in-plane it was assumed that the angular spread of the intensity could be reduced. Hence $FeTeO_x$ film was aligned to find (1/2 0 3/2) magnetic Bragg reflection. The theta-two theta scan of (1/2 0 3/2) magnetic peak is shown in figure 5.3.

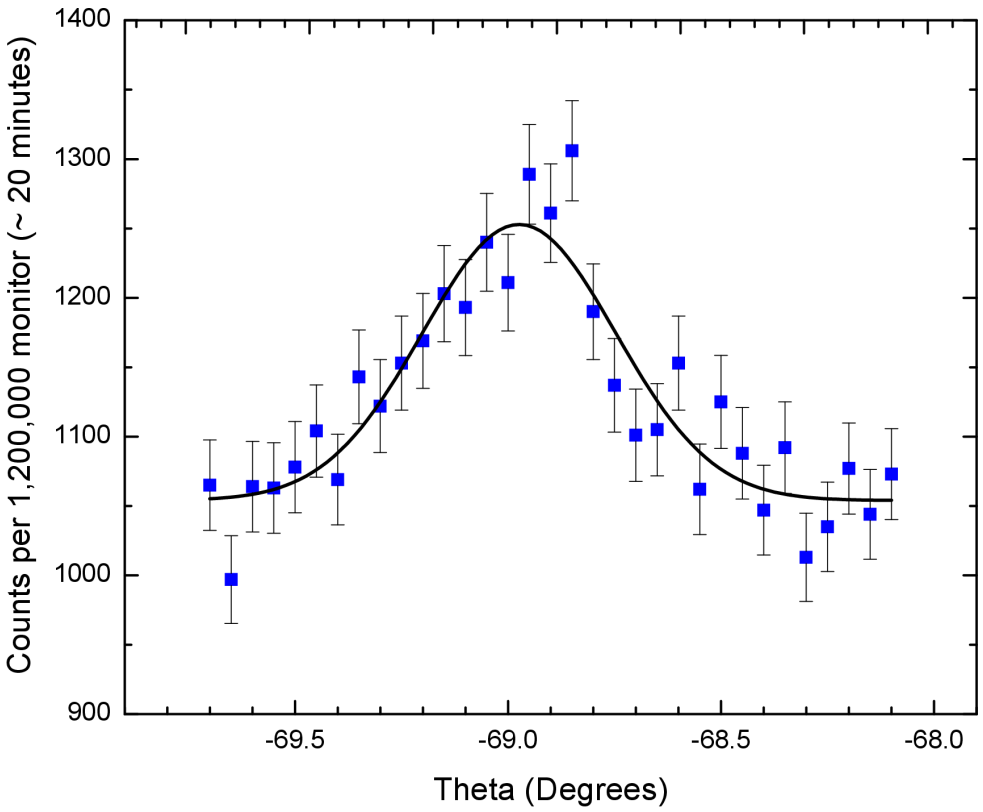

Figure 4-3 Theta-two theta scan of (1/2 0 3/2) Bragg reflection of $FeTeO_x$ film grown on $SrTiO_3$ substrate. The black solid line represents a Gaussian.

This magnetic peak was measured by varying the temperature from 5 K to 300 K in one point scans. The temperature dependent intensity of (1/2 0 3/2) magnetic Bragg peak of superconducting $FeTeO_x$ film is shown in figure 5.4. The black solid line is a guide to the eye representing the behavior of the order parameter with respect to temperature. Similar to non-superconducting film the antiferromagnetic order sets in around 70 K and develops as a function of temperature until around 17 K. Below 17 K a distinct reduction of the magnetic order could be observed indicating a suppression in magnetism at the onset of superconductivity. Despite of the uncertainty of the data set the black solid line is consistent with the data points and is suggestive of both co-existence of magnetism with superconductivity in but also some suppression of magnetic order in the superconducting state in $FeTeO_x$ films.

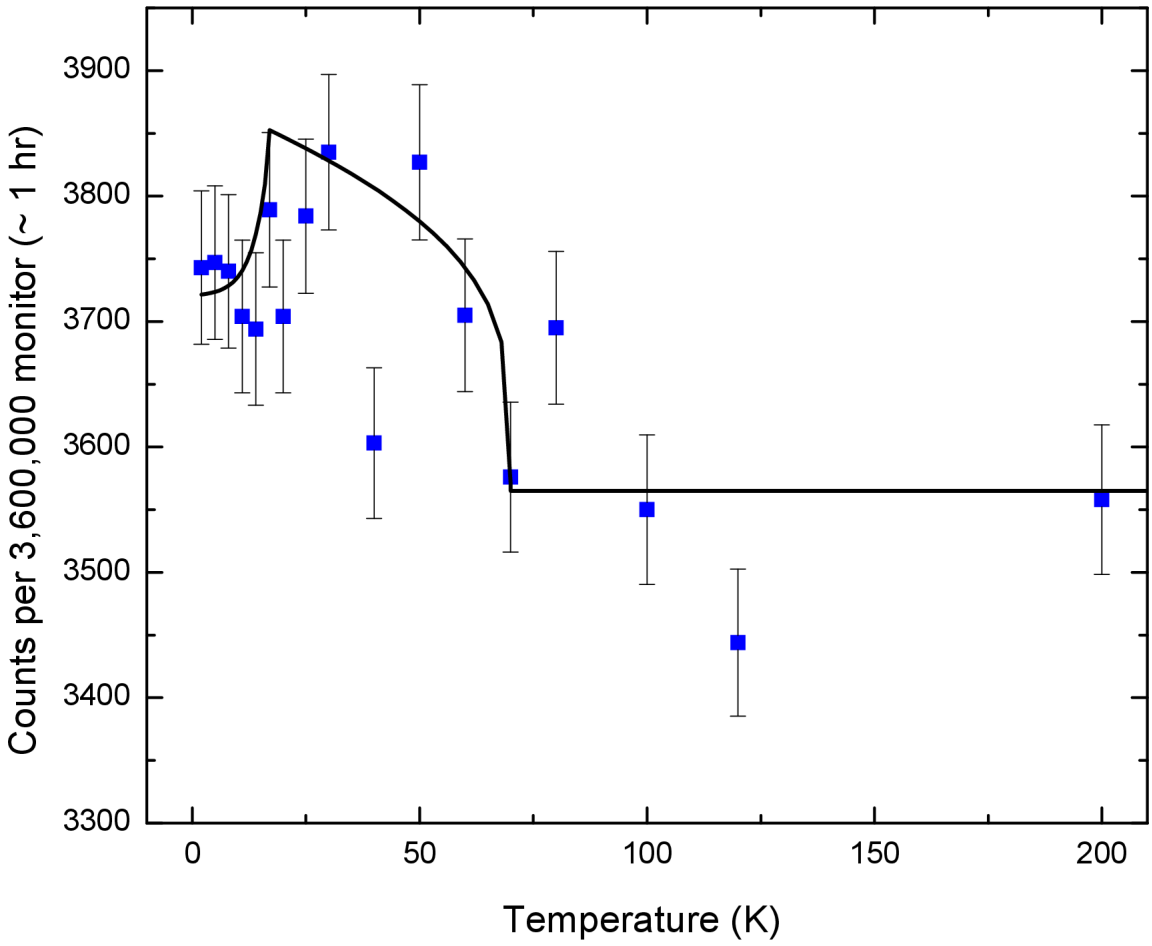

Figure 4-4 Temperature evolution of (1/2 0 3/2) Bragg reflection of a $FeTeO_x$ film grown on $SrTiO_3$ substrate. The black solid line is a guide to the eye, which represents the behavior of the order parameter as a function of temperature.

Both conventional and synchtrotron Mossbauer experiments were done on the 57Fe enriched $FeTeO_x$/FeTe films to identify the hyperfine fields associated with Fe nucleus in superconducting $FeTeO_x$/non-superconducting FeTe film system.

4.3 Mossbauer Spectroscopy

Mossbauer spectroscopy is a technique used to study the interactions between the nucleus and the local electromagnetic field produced by the electrons surrounding the nucleus, by the

recoil free absorption and re-emission of photons.[65] Recently this technique has been used as a local probe to get information about the local magnetism in iron-based superconductors due to the fact that 57Fe is a Mossbauer nucleus.[10,66–68]

Nuclei in a particular solid can be influenced by their surrounding electronic or magnetic environment. The resonant absorption and emission of gamma rays between two identical nuclei, a source nucleus and an absorber nucleus in a sample that we are interested in, has been used to study the environment around a particular nuclear site in the sample. In the case of 57Fe, radioactive 57Co decays into an excited state of 57Fe by electron capture. This provides the source nucleus for Mossbauer process. The 57Fe in excited state (I = 3/2) decays to its ground state (I = ½) by emitting a gamma ray with energy 14.41 keV. The life-time of the excited state is 98 ns. The decay of 57Fe with subsequent gamma ray emission is shown in figure 4-5.[69] Due to the very small line width of emitted gamma rays, these gamma rays can be used to detect energy differences associated with different states of the nuclei in the sample in neV range. These gamma rays emitting from the source nucleus can be absorbed by another 57Fe nucleus that we want to study. In order for resonance to occur the energy difference between the excited and ground state of source nucleus should be identical to that of absorber nucleus. But due to the difference in chemical environment of the absorber nucleus compared to the source nucleus there can be changes in the spin state and the quadrupole moment between the two. Therefore to exactly match the energy difference of the absorber and the source, the Doppler effect has been used to change the energy of the gamma rays emitting from the source nucleus. The source is moved in a certain velocity with respect to the absorber. At the velocities corresponding to the resonant energy levels of the sample a great portion of the emitted gamma rays will be absorbed by the sample resulting in the drop of the measured intensity of transmitted gamma rays.

Standard data sets are displayed as a graph of the intensity of transmitted gamma rays vs the velocity of the source. By studying this absorption spectrum we can get information about the local environment of the absorber nucleus.

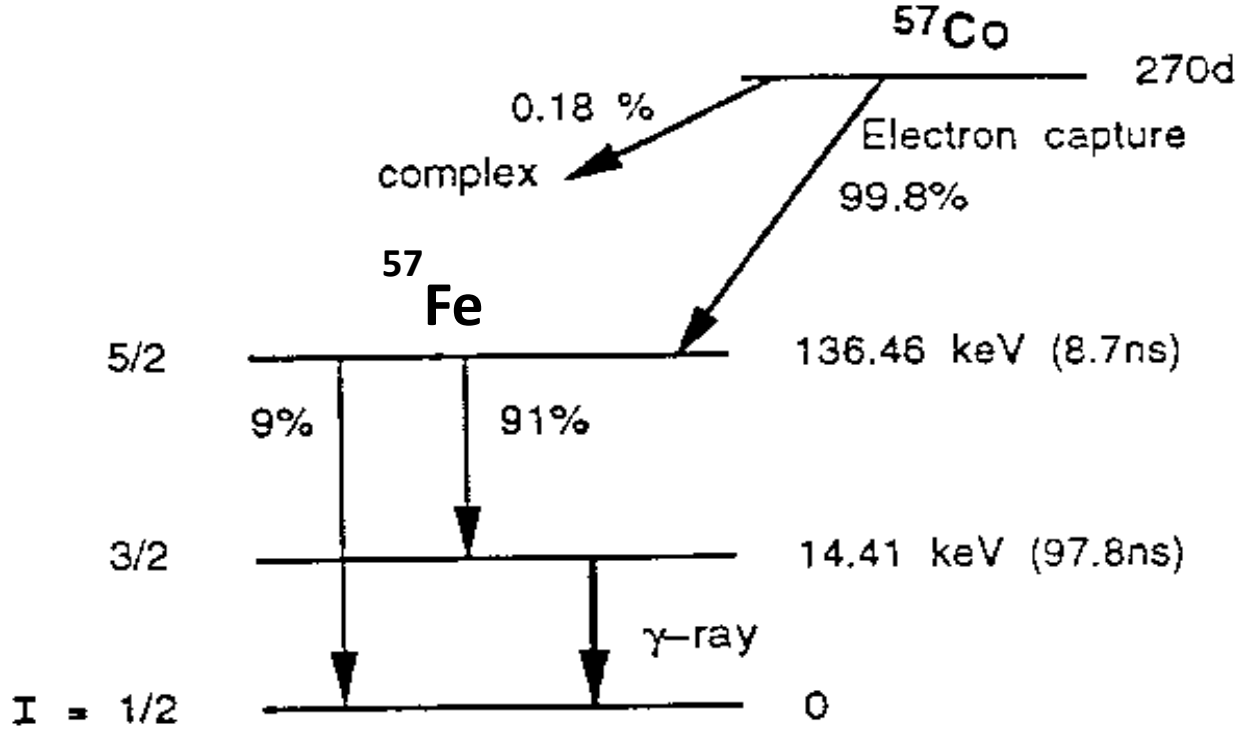

Figure 4-5 The schematic diagram representing the decay of radioactive 57Co with electron capture and the subsequent decay of 57Fe to its ground state by gamma ray emission.(adapted from ref. 69)

Hyperfine interactions are defined as the interactions between the nucleus and the surrounding electrons. In general three different hyperfine interactions can be observed. They are isomer shift, quadrupole interaction and magnetic interaction. The Isomer shift arises due to the interaction between the nuclear charge density and surrounding 's' electron charge cloud. Due to the isomer shift whole absorption spectrum will be shifted in either positive or negative direction depending on the 's' electron charge density of the sample compared to the source (see left hand

side of figure 4-6).[70] The Isomer shift can give information about the spin state as well as the co-ordination number.

Quadrupole splitting arises out of the interaction between the electric quadrupole moment of the nucleus and electric field gradient (EFG) created by electrons. The nuclei in states with angular momentum quantum numbers $I > ½$ have non-spherical charge distributions. This produces a nuclear quadrupole moment. This can interact with an inhomogeneous electric field produced by an asymmetric electrical charge distribution or ligand arrangement. As a result there can be nuclear states with different angular momentum states. In the case of 57Fe, I=3/2 excited state splits into two sub-states $m_I = \pm ½$ and $m_I = \pm 3/2$ as shown in right hand side of figure 4-6.[70] This results in two peaks in the absorption spectrum and commonly referred to as a 'doublet'.

Magnetic splitting arises due to the interaction between the nuclear spin moment and the local magnetic field produced by the electrons surrounding the nucleus. Due to the magnetic dipole interaction a nucleus with spin, I , splits into 2I + 1 sub energy states. In the case of 57Fe I =3/2 state will split into four sub-energy states and I =1/2 level into two sub-energy states. Due to six possible transitions in between these sub-states and ground state as shown in figure 4-8 the absorption spectrum will contain six peaks which is usually known as a sextet.[70]

When all above interactions are present in the sample between the nuclei and surrounding the resulting absorption spectrum will look complicated and asymmetric distribution of peaks could be seen as shown in figure 4-9. [71]

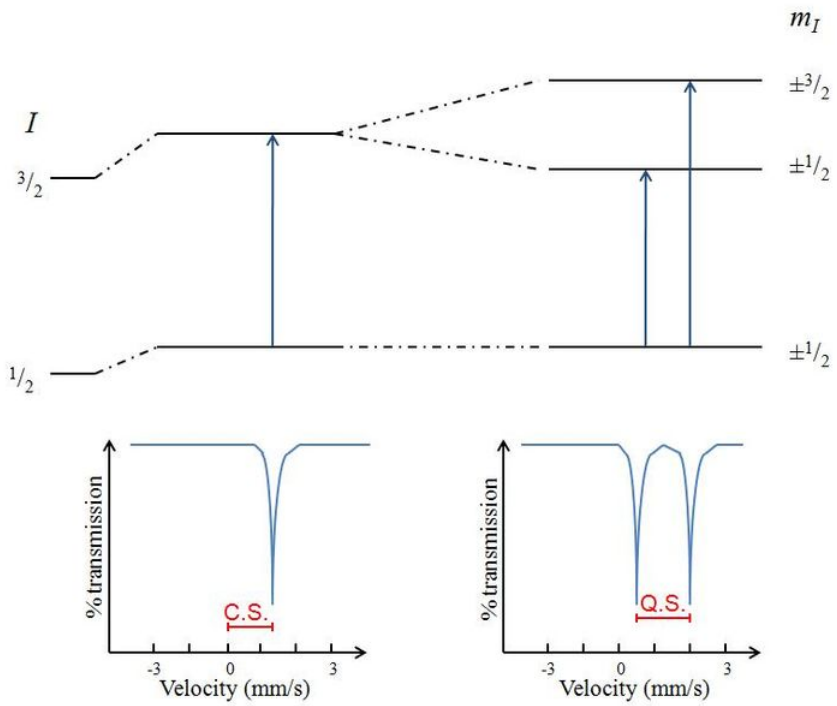

Figure 4-6 A schematic diagram of energy state splitting and the resulting absorption spectrum for a 57Fe nucleus which undergoes isomershift (chemical shift) and quadruple interaction.(adapted from ref.70)

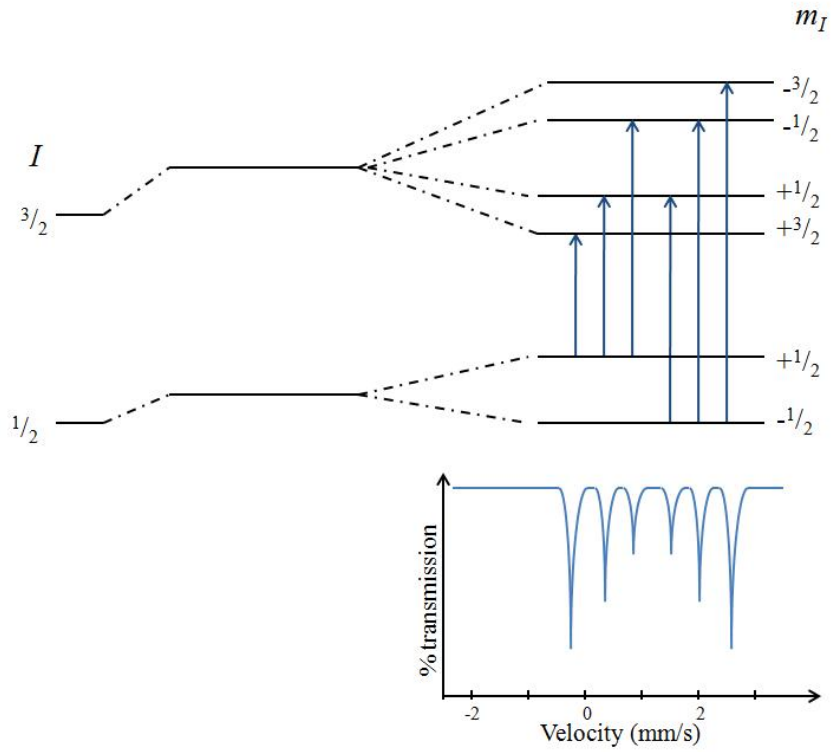

Figure 4-7 A schematic diagram of energy state splitting and the resulting absorption spectrum for a 57Fe nucleus which undergoes magnetic interaction.(adapted from ref. 70)

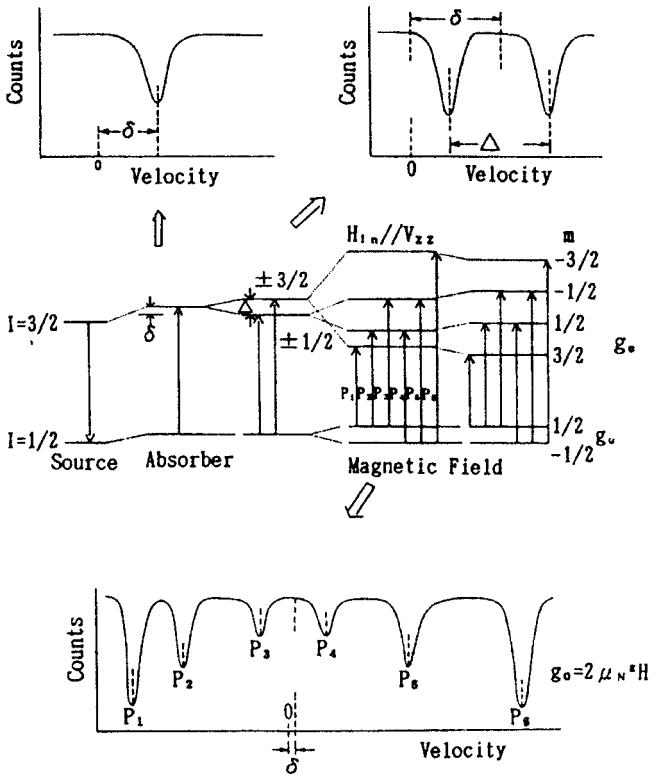

Figure 4-8 A schematic diagram of energy states splitting and the resulting absorption spectrum for a 57Fe nucleus which undergoes isomershift, quadrupole interaction and magnetic interaction. The figure at bottom shows an asymmetry in the dips of the transmission spectrum due to the combined effect. Please note that the energy transitions are not drawn in scale. (adapted from ref. 71)

4.3.1 Conventional Mossbauer Spectroscopy (CMS) vs Synchrotron Mossbauer spectroscopy(SMS)

Based on the Mossbauer effect, two different techniques have been developed to probe the electronic and magnetic structure of materials using hyperfine interactions. One is the conventional Mossbauer spectroscopy where a radioactive source has been used to obtain the gamma rays with correct energy in order to resonate the nuclei of the sample we are interested in. The second is a new technique that uses synchrotron radiation to observe nuclear resonant scattering (NRS).[72,73] Although both conventional Mossbauer spectroscopy and synchrotron Mossbauer spectroscopy share the same basic principle; resonant absorption of phonons by the

nuclear energy levels of excited Mossbauer atom, there are major differences in the scattering processes involved in the two techniques. In CMS, the gamma rays emitted from the source are absorbed by the nucleus in the sample as it transitions to an excited state. By measuring the intensity of the gamma rays transmitted through the sample, an absorption spectrum is obtained and this absorption spectrum is studied to get information about the system. Since the absorption is measured as a function of energy this process in known as the Mossbauer spectroscopy in the energy domain. After the absorption, the absorber nucleus in the excited state decays by emission of an internal conversion electron or a resonant fluorescence photon. In CMS, all the absorption events are measured without considering the subsequent decay paths. On the other hand in SMS, the synchrotron radiation tuned to the appropriate energy states of the sample nuclei is absorbed by the system and system decays later into the original state. Since SMS only measures events where the nucleus decays directly to the original ground state, SMS is known as a coherent scattering process.[74–76] Here the relaxation process from excited state to the ground state will be detected w.r.t. time instead of the absorption process w.r.t. energy.

In synchrotron Mossbauer spectroscopy, first one pulse of synchrotron radiation, which is tuned to the nuclear energy levels of the sample, will interact with the absorber nuclei. Then the coherent decay process from the excited state to ground state of the nuclei in the sample will be observed with respect to time. Once the decay process of the system is over another radiation pulse will be come and the above process will be repeated. This is also known as the nuclear forward scattering in the time domain or Mossbauer spectroscopy in the time domain. The major advantage in this technique compared to CMS is the low background. The synchrotron radiation is pulsed such that the time difference between two consecutive pulses (153.8 ns in advanced photon source) is larger than the lifetime of the nuclear excited state (97.8 ns for ^{57}Fe, I =3/2

state) and the duration of one pulse (0.1 ns) is much smaller than the lifetime of the nuclear excited state. Therefore the effect of incoming synchrotron radiation will be minimum during the decay process. Only the radiation emitting from the excited nuclei will be detected resulting in a low background. Hence this technique can be considered as a powerful probe, which can provide very subtle details of the system without any influence from the background. Therefore to study samples like thin films that have smaller amount of material this technique is more appropriate than the CMS.[77,78]

The resulting spectra from SMS in time domain show major differences compared to the absorption spectrum obtained in CMS. CMS is based on the method of resonance absorption and the transmitted radiation from the sample after absorption is measured as a function of energy. SMS is based on the scattering of nuclear signals. In SMS, when the nuclear energy levels in the sample are changed or split due to the hyperfine interactions, during the decay process instead of one transition from excited state to ground state, several transitions with slightly different energies will occur due to the splitting of energy levels. The superposition of these transitions will result in constructive and destructive interference between nuclear scattering signals. In terms of time domain, these transitions are analogous to a set of oscillators with slightly different frequencies. The superposition of these oscillators will result in " beating" with each other. The resulting oscillatory pattern in the time scale can be used to study the hyperfine interactions and hence the electronic or magnetic structure around the nucleus in a material.[74,79] A diagram of intensity vs time of a pulsed synchrotron radiation source at advanced photon source at Argonne, is shown in figure 4-10(a). Figure 4-10(b) represents the synchrotron Mossbauer spectra obtained in the time domain representing the isomershift between EuS and Eu_2O_3 and figure 4-10(c) shows the analogous of this spectrum in energy domain. [78]

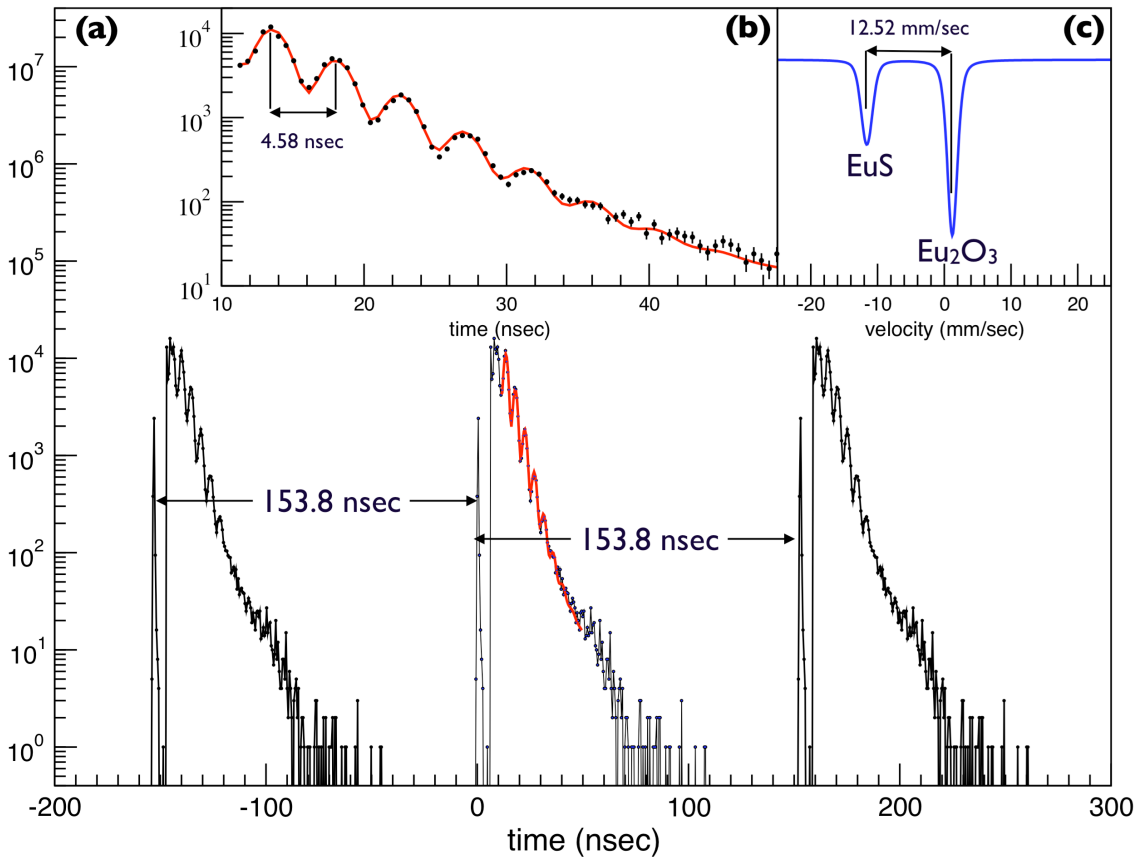

Figure 4-9 A schematic diagram of (a) Pulsed synchrotron radiation plotted in intensity vs time (b) The Mossbauer spectrum in time domain representing the isomer shift between Eus and Eu_2O_3 compounds. (c) The stimulated spectrum in energy domain using spectrum in (b). The superposition of two decay signals which are 12.52 mm/sec (~ 602 neV) differ in energy would result in a beating pattern 4.58 nsec apart in time. (figure adapted from ref. 79).

4.4 Conventional Mossbauer Spectroscopy

4.4.1 Experimental Details

The conventional Mossbauer spectroscopy experiment was carried out in Dr. Erchan Alp's laboratory at Argonne. The aim of this experiment was to identify any local magnetic moment associated with the Fe sites in superconducting $FeTeO_x$ films below the antiferromagnetic and structural transition and to check how the local moment changes at the onset of superconductivity. It was also interesting to identify the hyperfine fields associate with

Fe nucleus in the non-superconducting FeTe films and compare with the data in the literature. For this experiment 57Fe enriched very thick films of thickness around 500 nm were used.

A radioactive 57Co was driven towards and away from the sample to emit gamma rays with appropriate energy. The phonons emitted from the sample were collected by a Ge detector. The experiment was done in transmission geometry.

4.4.2 Results and Discussion

Figure 5-11 shows the different Fe sites identified in FeTe and $FeTeO_x$ unit cells using the information published using x-ray and neutron and diffraction techniques.[23,24,80] The occupancy for each site was predicted by the values given in literature and from the known information so far about superconducting $FeTeO_x$. Figure 5-12 shows the absorption spectrum of a 57Fe enriched superconducting $FeTeO_x$ film, which is denoted by "SC-1". The raw data were fitted by "Mossbauer Conventional Program" to obtain hyperfine parameters. The observed parameters for several samples are summarized in table 5-1. For "SC-1" a clear signal could be observed at room temperature without any magnetic sextets.

In order to get the best cumulative fit, which matches with the raw data, raw data were fitted as a contribution from two different iron sites with comparable occupancy. So far this result is somewhat consistent with the different iron sites suggested for superconducting $FeTeO_x$ unit cell as shown in figure 4-11. The two iron sites with comparable occupancy can be considered as Fe-(1) and Fe-(3) and it is possible that the contribution from the excess iron site (Fe-(2) site) could not be seen in this data set due to its low occupancy. To verify this result another superconducting $FeTeO_x$ film enriched with ^{57}Fe (SC-2) was tested at room temperature and the result is shown in figure 4-13. This superconducting sample also shows a similar result to

that of previous sample. To confirm that the two iron sites with comparable occupancy arises due to superconductivity a non-superconducting film enriched with ^{57}Fe was tested.

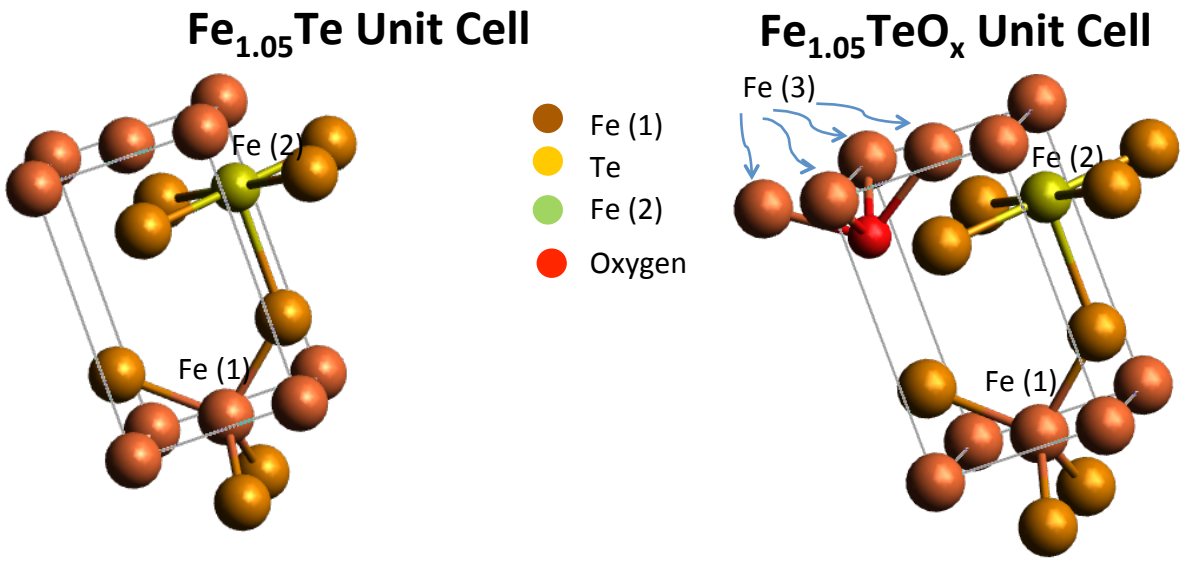

Fe Site	Occupancy	Coordination Number
Fe (1)	1.00	4
Fe (2)	0.05	5

Fe Site	Occupancy	Coordination Number
Fe (1)	0.60	4
Fe (2)	0.05	5
Fe (3)	0.40	5

Figure 4-10 Schematic diagram of different iron sites and their occupancy in $FeTeO_x$ and FeTe predicted by x-ray and neutron diffraction studies. [23,24,80]

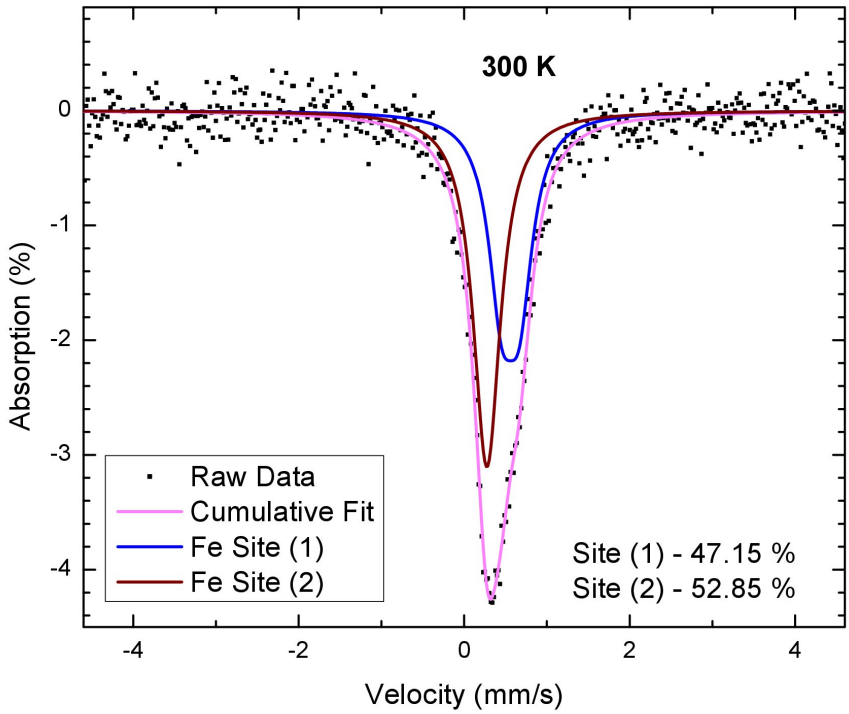

Figure 4-11 Mossbauer spectra of a superconducting $FeTeO_x$ film (SC-1) obtained at room temperature. The raw data is fitted by two iron sites.

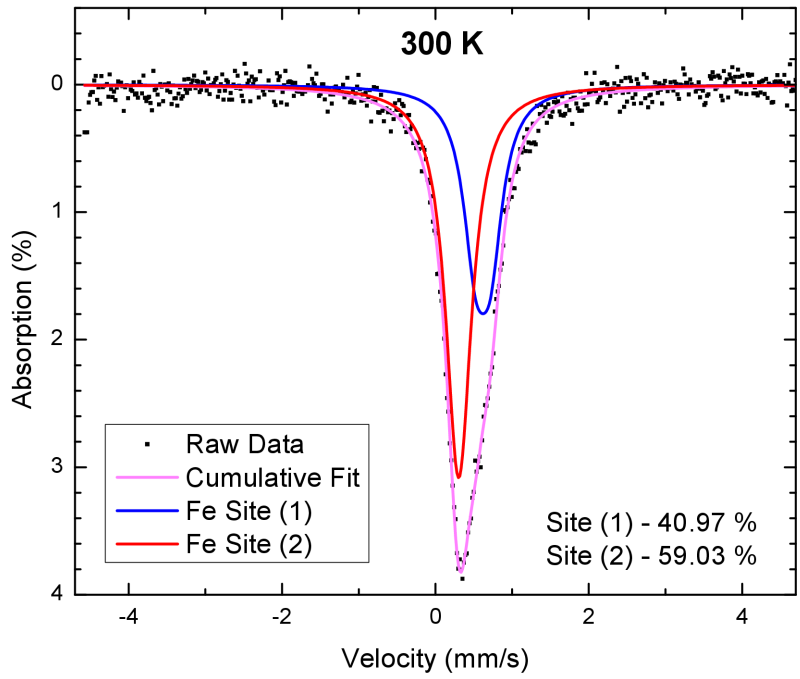

Figure 4-12 Mossbauer spectra of a superconducting $FeTeO_x$ film (SC-2) obtained at room temperature. The raw data is fitted by two iron sites.

The absorption spectrum of a non-superconducting film is shown in figure 4-13. Surprisingly this spectrum could also be fitted by two iron sites with comparable occupancy rather than a single site with very high occupancy. This result indicates that the two iron sites with comparable occupancy is not associated with superconductivity but common to $FeTeO_x$ and FeTe films. This result is quite different from the reports in the literature for FeTe where the second site is assumed to be due to excess iron in the FeTe unit cell (Fe-(2) according to figure 4-11) and the occupancy of the second site is very small compared to that of the first site. To check whether this effect is inherent to $FeTeO_x$/FeTe films, a bulk single crystal of $Fe_{1.05}Te$ was tested and the relevant absorption spectrum is shown in figure 4-14. This also can be fit by two Fe sites with comparable occupancy. All the absorption spectrums from 4-11 to 4-14 indicate that superconducting $FeTeO_x$ and non-superconducting FeTe shows two different iron sites with nearly equal occupancy. The room temperature spectrums don't show any hyperfine magnetic fields. This rules out the possibility of existence of any iron oxides or unreacted iron in considerable amounts in the FeTe/$FeTeO_x$ films. Hence the second iron site should be in paramagnetic environment in FeTe lattice. Since diffraction techniques indicate only one tetrahedrally coordinated Fe site in the FeTe lattice, the occurrence of two different iron sites with comparable occupancy is a puzzle. As shown in table 5-1 the isomershift (~ 0.3 mm/s) and quadrupole splitting (0 mm/s) of second site suggest that the second site can be in a 3+ valence state and the isomershift (~ 0.54 - 0.65 mm/s) and quadrupole splitting (~ 0.22 mm/s) of first site suggests that it can be in a state between 3+ and 2+. It is possible that electron hopping can occur between some iron sites.

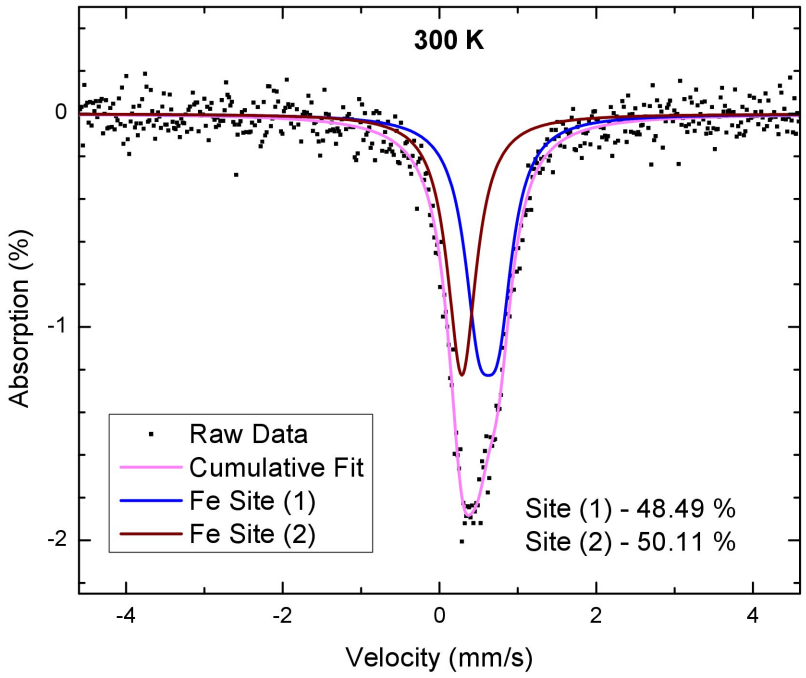

Figure 4-13 Mossbauer spectra obtained at room temperature for a non-superconducting FeTe film grown on CaF_2 substrate. The raw data is fitted by two iron sites.

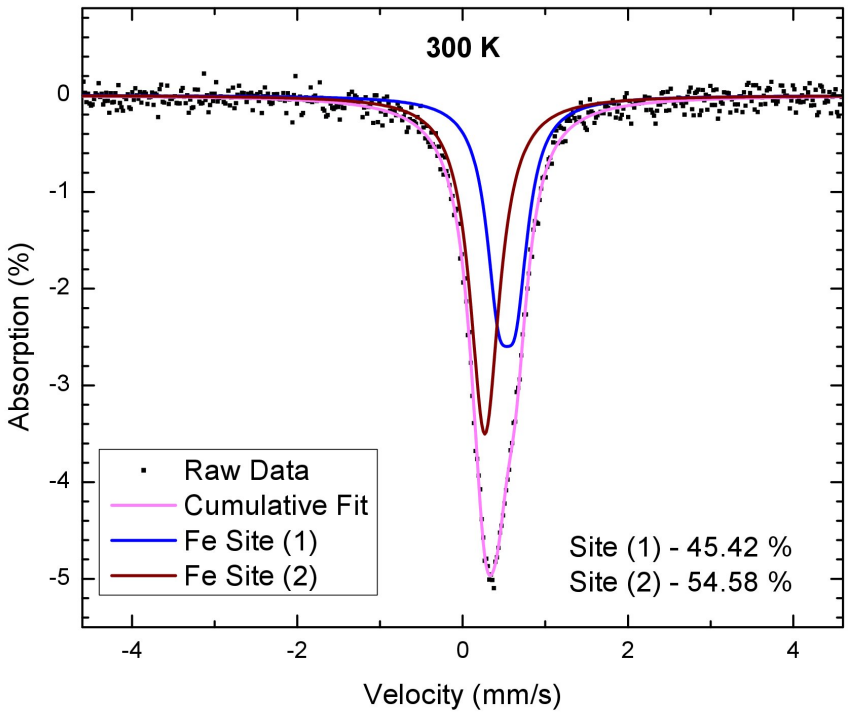

Figure 4-14 Mossbauer spectra of bulk single crystal of $Fe_{1.05}Te$ obtained at room temperature. The raw data is fitted by two different iron sites.

Table 4-3 shows the Mossbauer parameters reported in literature for parent FeTe at room temperature. The isomershifts and quadrupole splitting values reported in literature are somewhat consistent with the values obtained for the Fe-(1) site of superconducting $FeTeO_x$ and non-superconducting FeTe. The major difference between our data and the reported data is that for our non-superconducting FeTe films and bulk single crystals we could observe two iron sites with comparable occupancy but reported data doesn't show iron sites with comparable occupancies.

In order to track down any hyperfine magnetic fields associated with Fe nucleus in superconducting $FeTeO_x$ the conventional Mossbauer spectroscopy experiment was done upon cooling another 57Fe enriched $FeTeO_x$ film (SC-2) in a cryostat and taking absorption spectra at 300 K, 90 K, 50 K, 10 K and 5 K. Figure 4-16 and 4-17 show the Mossbauer spectra obtained for superconducting film at these temperatures, with Fig 4-16 contains data from above the magnetic transition and Fig 4-17 below. Table 4-2 summarizes the hyperfine parameters in the whole temperature range obtained for superconducting $FeTeO_x$ film grown on MgO (SC-2).

At room temperature a clear signal can be seen and there is no magnetic order associated with the sample. The raw data can be fit by two iron sites with relative occupancy of 40 : 60, roughly similar to the previous samples. The isomershift and quadrupole splitting values indicate that the first site is in a mixed valence state between 3+ and 2+ and second iron site is in 3+ valence state. By the quadrupole splitting value of 1^{st} site it can be assumed that the first iron site experiences a larger electric field gradient, hence it is in a less symmetrical environment compared to the second site. At 90 K quadrupole splitting can be seen in both iron sites indicating that as the temperature decreases both iron sites experience more asymmetrical environment

The Hyperfine parameters of Conventional Mossbauer Spectra at 300 K						
Temperature	**Site**	**Isomer Shift (mm/s)**	**Quadrupole Splitting (mm/s)**	**Hyperfine Field (T)**	**Occupancy (%)**	**Width (mm/s)**
A superconducting film grown on MgO substrate (SC 1)						
300 K	Fe (1)	0.56±0.02	0.22±0.03	0	47.15	0.385
	Fe (2)	0.277±0.009	0	0	52.85	0.398
A superconducting film grown on MgO substrate (SC 2)						
300 K	Fe (1)	0.62±0.01	0.19±0.02	0	40.97	0.39
	Fe (2)	0.303±0.006	0	0	59.03	0.41±0.01
A Non-Superconducting FeTe Film grown on CaF2 substrate (NSC 1)						
300 K	Fe (1)	0.65±0.02	0.22±0.03	0	49.89	0.45
	Fe (2)	0.30±0.01	0	0	50.11	0.47±0.02
A Bulk single crystal $Fe_{1.05}$ Te						
300 K	Fe (1)	0.54±0.02	0.21±0.01	0	45.42	0.37±0.02
	Fe (2)	0.271±0.008	0	0	54.58	0.431±0.009

Table 4-1 The hyperfine parameters of Mossbauer spectrums at room temperature for $FeTeO_x$ and FeTe

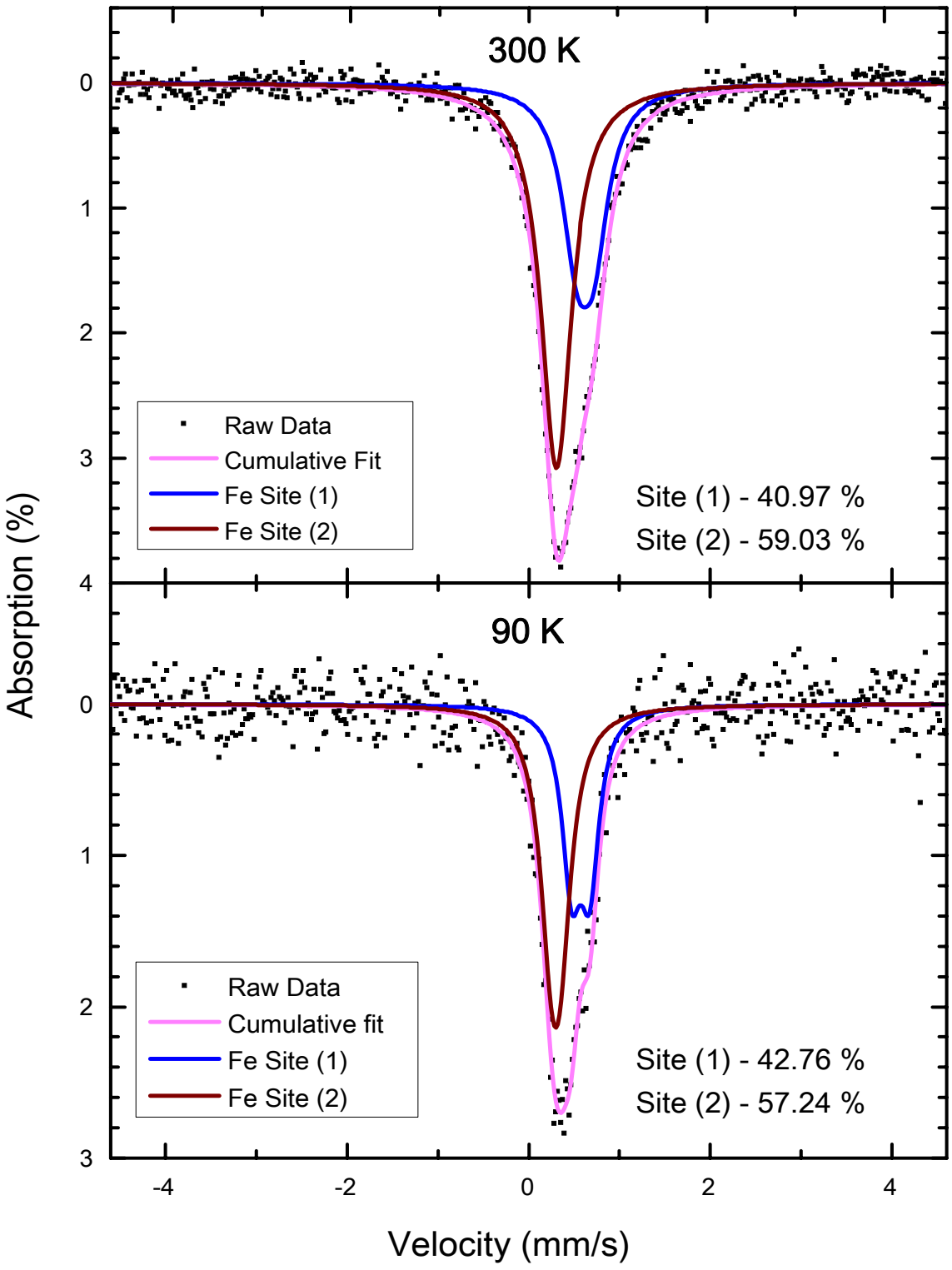

Figure 4-15 Mossbauer spectra obtained for superconducting $FeTeO_x$ film grown on MgO substrate (SC-2) at 300 K and 90 K.

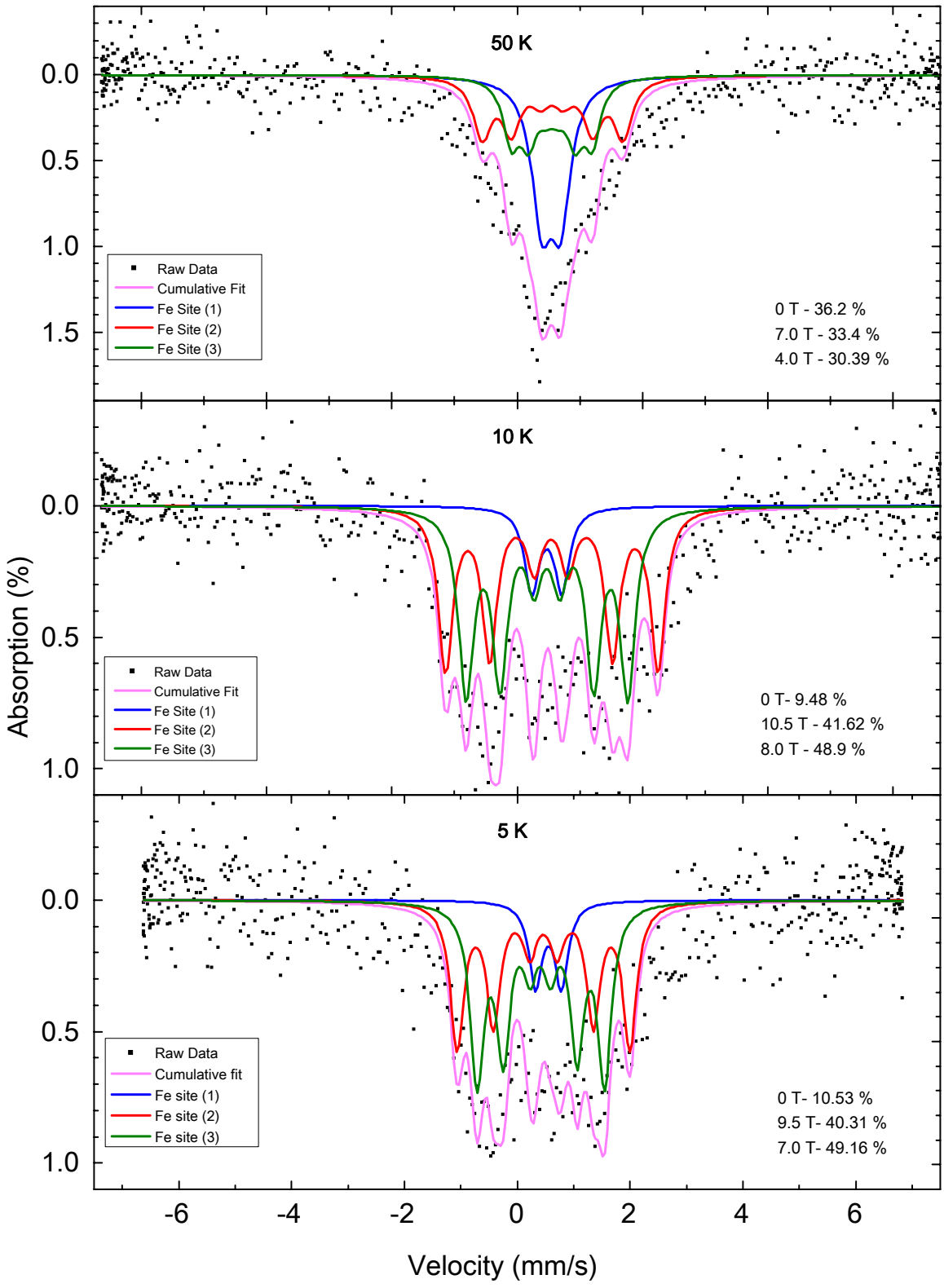

Figure 4-16 Mossbauer spectra for superconducting $FeTeO_x$ film grown on MgO substrate (SC-2) at low temperature.

The Hyperfine parameters of conventional Mossbauer Spectra for Superconducting $FeTeO_x$ film

A Superconducting $FeTeO_x$ Film grown on MgO substrate (SC 2)						
Temperature	**Site**	**Isomer Shift (mm/s)**	**Quadrupole Splitting (mm/s)**	**Hyperfine Field (T)**	**Occupancy (%)**	**Width (mm/s)**
5 K	Fe (1)	0.56 ± 0.03	0.46±0.04	0	10.53	0.28±0.07
	Fe (2)	0.47 ± 0.01	0	9.48±0.08	40.31	0.29±0.03
	Fe (3)	0.42	0.01	7.01	49.16	0.29
10 K	Fe (1)	0.48±0.02	0.48±0.04	0	9.48	0.28±0.07
	Fe (2)	0.56	0.01	10.5	41.62	0.28
	Fe (3)	0.484±0.008	0	8.00±0.06	48.9	0.29±0.02
50 K	Fe (1)	0.55±0.01	0.30±0.07	0	36.2	0.38±0.08
	Fe (2)	0.57±0.02	0.01	7.0±0.1	33.4	0.35±0.06
	Fe (3)	0.56±0.03	0	4.0±0.2	30.39	0.35±0.08
90 K	Fe (1)	0.58±0.02	0.20±0.02	0	42.76	0.25±0.02
	Fe (2)	0.30±0.01	0.10±0.04	0	57.24	0.30±0.01
300 K	Fe (1)	0.62±0.01	0.19±0.02	0	40.97	0.39
	Fe (2)	0.303±0.006	0	0	59.03	0.41±0.01

Table 4-2 The hyperfine parameters extracted from the fitted Mossbauer spectra for a superconducting $FeTeO_x$ film grown on MgO substrate (SC-2).

At a temperature of 50 K clear magnetic sextets could be observed as a result of hyperfine magnetic fields experienced by iron sites. This indicates superconducting $FeTeO_x$ shows magnetic order below 50 K similar to parent FeTe. This result is consistent with the

neutron diffraction data obtained for a superconducting film at low temperature. At 50 K the raw data can be fit using three different iron sites, two with magnetic sextets of 7 T and 4 T and one with a non-magnetic site. The relatively high occupancy of the non-magnetic site indicates that at 50 K this particular sample becomes partially magnetic. From 50 K to 10 K, just below the superconducting transition temperature of 12.5 K, the hyperfine magnetic fields of the two iron sites increase and the occupancy of the non-magnetic component decreases. From 50 K to 10 K almost certainly we are seeing an increase in the hyperfine fields as magnetic order fully develops. This is typical of second order phase transitions. Strictly speaking it would be better to have data at a temperature just above T_c, but we know superconductivity sets in gradually (see Meissner data for example) so probably T = 10 K is a decent stand for T = T_c.

At a temperature of 5 K, a temperature well below the superconducting transition, a small decrease in the hyperfine magnetic fields (10 % decrease for one site and 12.5 % decrease for the other site) could be observed compared to the values at 10 K. It is somewhat less clear if the drop in hyperfine fields from 10 K to 5 K is necessarily due to superconductivity, but that is at least a reasonable inference roughly compatible with the reduction in average magnetic moment observed from neutron diffraction data for superconducting $FeTeO_x$. The reported temperature evolution of hyperfine magnetic fields of superconducting $FeTe_{0.8}S_{0.2}$ (fig. 5 in reference 79) by sklyarova shows a somewhat similar behavior to the temperature evolution of hyperfine fields of superconducting $FeTeO_x$ where the hyperfine field increases with decreasing temperature and shows a reduction at T_c of superconducting $FeTe_{0.8}S_{0.2}$.[81] The magnitude of these hyperfine fields are also consistent with the magnitude of those observed for superconducting $FeTeO_x$.

The reported Mossbauer parameters for parent FeTe at low temperature are given in the table 4-4. The hyperfine magnetic fields obtained for superconducting $FeTeO_x$ are consistent in

magnitude with the reported hyperfine magnetic fields for FeTe at low temperature for low excess iron concentration.

The conventional Mossabuer spectra obtained on superconducting $FeTeO_x$ at low temperature allow us to conclude that superconducting $FeTeO_x$ undergoes an antiferromagnetic transition. The small decrease in hyperfine magnetic fields observed at 5 K compared to 10 K suggests that there can be a small reduction in local magnetic fields around Fe sites due to superconductivity.

Below 50 K a large quadrupole splitting is observed in the non-magnetic iron site. This can be a result of the structural transition from tetragonal to monoclinic that occurs in this compound. Since the monoclinic structure is less symmetric compared to tetragonal structure large electric field gradients can be expected for the iron sites in the sample.

Publication	Material	Different Iron Sites	Room Temperature Data			
			Relative Contribution (%)	Isomershift (mm/s)	Quadrapole Splitting (mm/s)	Line width (mm/s)
Physica C 470 (2010) S338-S339	$Fe_{1.08}Te$ (polycrystalline)	Fe (1)	100	0.452	0.315	
Mizuguchi et. al.		Fe (2)		Minor effect	Minor effect	
J. Phys.: Condens. Matter 24 (2012) 386006	$Fe_{1.06}Te$ (single crystal)	Fe (1)	84	0.495	0.315	0.21
Blachowski et. al.		Fe (2)	12	0.28	0	0.21
		Fe (3)	4	0.22	0.84	0.21
	$Fe_{1.10}Te$ (single crystal)	Fe (1)	87	0.462	0.32	0.27
		Fe (2)	6	0.29	0	0.27
		Fe (3)	7	0.36	1.03	0.27
J Supercond Nov Magn 23, 551-557 (2010)	FeTe (polycrystalline)	Fe (1)	93.6	0.46	0.32	
Gomez et. al.		$FeTe_2$ phase	6.4	0.29	0.99	
J. Phys. C, Solid State Phys. 12, 873-879 (1979)	FeTe	Fe (1)	0.62	0.462	-0.255	0.173
Ward et. al.		Fe (2)	0.3	0.458	0.406	0.164
		Fe (3)	0.09	0.45	0.6	0.16
Phys. Rev. B, 16 3908-3912 (1977)	FeTe	Fe(1)		0.224	0.428	
Aggarwal et. al.						

Table 4-3 Reported Mossbauer parameters for FeTe at room temperature

Publication	Material	Different Iron Sites	Low Temperature Data							
			20 K				4.2 K			
			Relative Contribution (%)	Hyperfine field (kG)	Isomer Shift (mm/s)	Quadrupole Splitting (mm/s)	Relative Contribution (%)	Hyperfine field (kG)	Isomer Shift (mm/s)	Quadrupole Splitting (mm/s)
Physica C 470 (2010) S338-S339	$Fe_{1.08}Te$ (polycrystalline)	Fe (1)					100	103.4kOe		
Mizuguchi et. al.		Fe (2)						Minor effect		
J. Phys.: Condens. Matter 24 (2012) 386006	$Fe_{1.06}Te$ (single crystal)	Fe (1)	92	99	0.578	0.122	93	101	0.577	0.118
Blachowski et. al.		Fe (2)	4	156			4	158		
		Fe (3)	3	212			2	211		
			1	480			1	486		
	$Fe_{1.10}Te$ (single crystal)	Fe (1)	86	97	0.593	0.112	84	97	0.584	0.11
		Fe (2)	5	153			6	151		
		Fe (3)	5	209			5	211		
			4	471			5	480		

Table 4-4 Reported Mossbauer parameters for FeTe at low temperatures

In order to detect any subtle changes in the hyperfine fields associated with Fe nucleus occurs due to superconductivity in $FeTeO_x$, synchrotron Mossbauer technique was used. As explained in a section 4.3.1, due to the high signal to background and other advantages, this technique can reveal more information about $FeTeO_x$/FeTe thin film system compared to the conventional Mossbauer technique. To get an idea about how the synchrotron Mossbauer beating pattern looks like for superconducting $FeTeO_x$ a simulation was done using the conventional Mossbauer spectroscopy data obtained for $FeTeO_x$. The simulated Mossbauer spectrum in time domain is shown in figure 4-11.

4.5 Synchrotron Mossbauer Spectroscopy

4.5.1 Experimental Details

The Synchrotron Mossbauer experiment was performed at beam-line 3ID-D at the Advanced Photon Source in Argonne National Laboratory. The energy of synchrotron radiation was tuned to the resonant energy of ^{57}Fe nucleus using three monochromators. A beam of 1 mm in width and 0.5 mm in height was used. The experiment was done in transmission geometry. For the superconducting sample grown on MgO substrate data were taken at the temperatures, 120 K, 70 K, 40 K, 20 K, 10 K, 5 K and 3.3 K. For this sample an average of around 100 nuclear forward scattering counts per second were obtained at 120 K. In order to get better statistics data were taken for 3 hours at each temperature point. For the non-superconducting sample grown on CaF_2 substrate data were taken at temperatures of 120 K, 70 K and 5 K. For this sample only 10 average nuclear forward scattering counts per second could be observed at 120 K. The reason that fewer counts were detected was that the transmission of 14.4 KeV photons through CaF_2 is relatively low compared to MgO. For a 0.5 mm thick substrate the estimated transmission coefficient of 14.4 KeV photons through MgO was 0.415 where through CaF_2 it was 0.054.

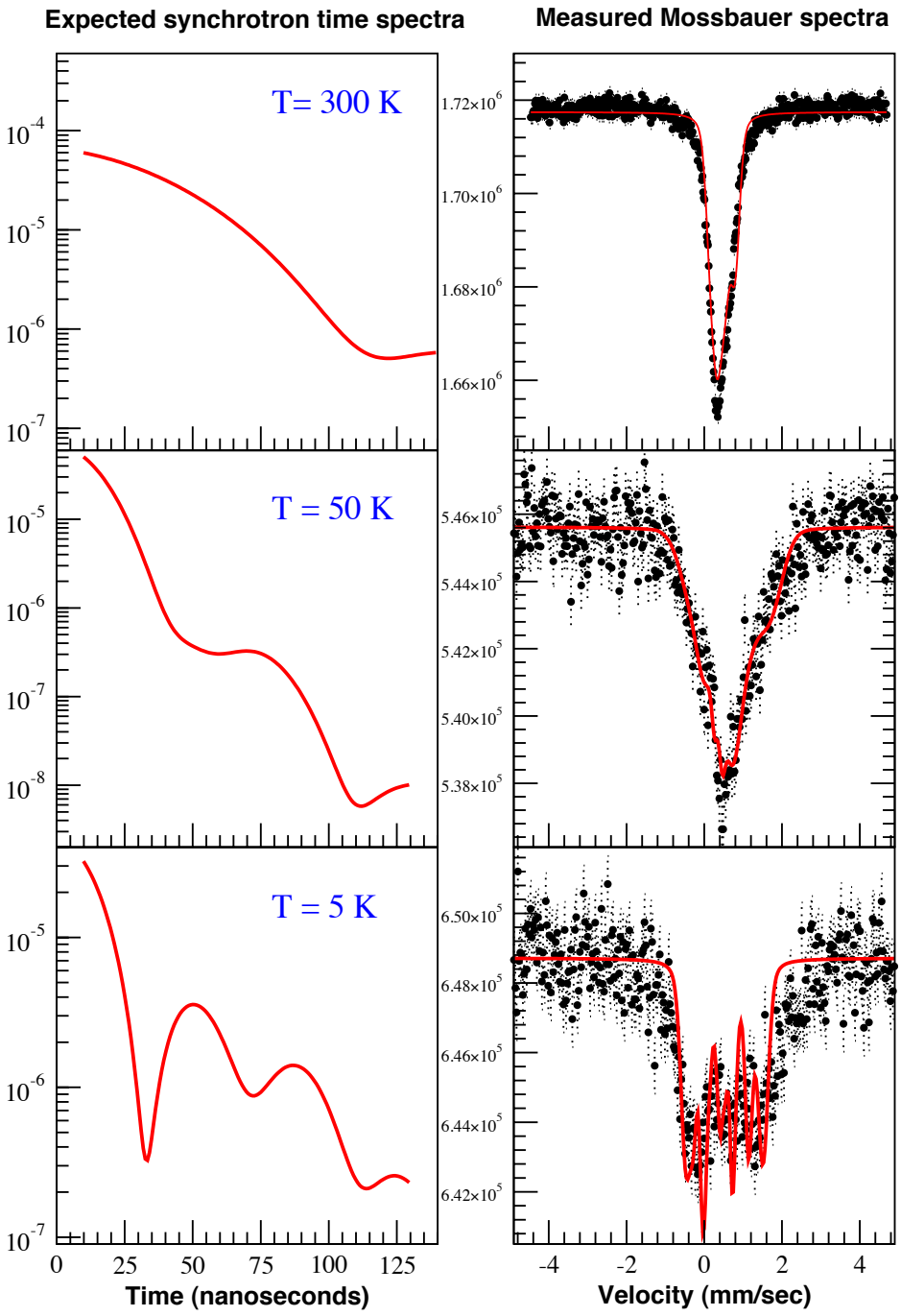

Figure 4-17 Schematic diagram of the simulated time spectra done using conventional Mossbauer spectroscopy data obtained in energy domain for superconducting $FeTeO_x$.

4.5.2 Results and Discussion

Figure 4-19 shows the temperature dependent nuclear forward scattering counts obtained with respect to time for the superconducting $FeTeO_x$ film grown on MgO. At 120 K a clear nuclear decay signal could be observed and there is no trace of magnetism. There are isomer shifts and quadrupole interactions experienced by iron sites in $FeTeO_x$ at this temperature but the resulting beating pattern due to above transitions have very small frequencies. Therefore those frequencies cannot be clearly seen in this data set. The data at 70 K also look similar to that of 120 K. At 40 K a fast beating pattern could be observed indicating the hyperfine magnetic fields associated with Fe sites in $FeTeO_x$. This is evidence that superconducting $FeTeO_x$ undergoes the antiferromagnetic transition at a temperature below 70 K. At temperatures below superconducting transition temperature the data looks very similar to the data at 40 K. From this data set a significant difference could not be observed in the hyperfine fields of the $FeTeO_x$ film in superconducting state compared to the normal state. The time spectrum at 5 K for superconducting $FeTeO_x$ looks somewhat similar to the simulated spectrum at 5 K (as shown in Fig. 4-18). But the actual time spectrum at 5 K (as shown in Fig. 4-19) can be considered as a superposition of several hyperfine magnetic fields with different occupancies similar to the figure 2(b) in ref. 75. [76] The spectrum at 5 K can be fit by four hyperfine magnetic fields, 7.5 T, 4.38 T, 2.9 T and 50.5 T with relative occupancies, 17 %, 39 %, 43 % and 1 % respectively. 50.5 T field indicates that some iron oxides are present as impurities in superconducting $FeTeO_x$ sample in a very small amount (1 %). This kind of small impurities could not be detected by the conventional Mossbauer method in superconducting $FeTeO_x$ films. Hence synchrotron Mossbauer spectroscopy can be considered as a powerful probe, which can detect large hyperfine magnetic fields present in small quantities in samples.

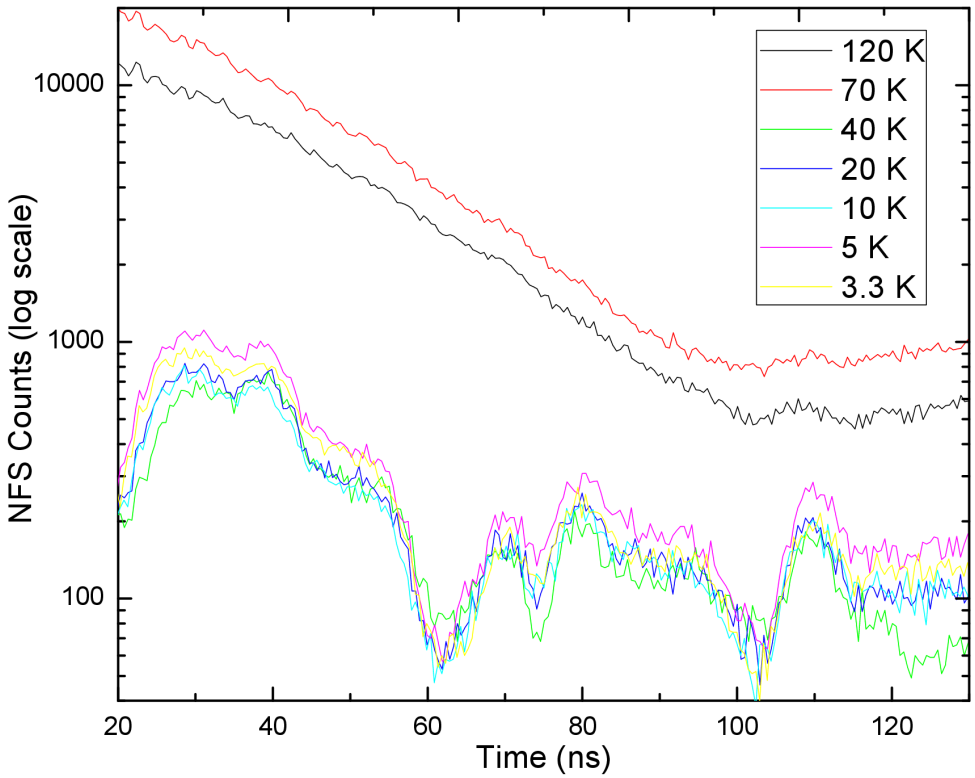

Figure 4-18 Temperature evolution of the nuclear forward scattering time spectra for a superconducting $FeTeO_x$ grown on MgO substrate.

Figure 4-20 shows the temperature dependent nuclear forward scattering counts obtained with respect to time for the non-superconducting reference sample. Compared to the data at 120 K for superconducting sample, the data at 120 K for this sample shows some beating pattern with small amplitude indicating the presence of some magnetic impurities. At 5 K a strong beating pattern could be observed indicating large magnetic hyperfine fields with high occupancies are associated with the iron sites in the reference sample. The time spectrum at 5 K for reference sample can be fit by three hyperfine magnetic fields 19 T, 4 T and 6 T with relative occupancies, 72 %, 27 % and 0.24 % respectively. Compared to the superconducting sample, reference sample is associated with larger hyperfine magnetic fields at 5 K indicating that some magnetic impurities are present in the reference sample. Blachowski[82] reported a magnetic field of 21.2 T (see table 4-4) for parent $Fe_{1.06}Te$ at 4.2 K but the relative occupancy (2 %) is much smaller than

that of our reference sample (72 %). It is possible that this particular reference sample contains some magnetic impurities in large quatities.

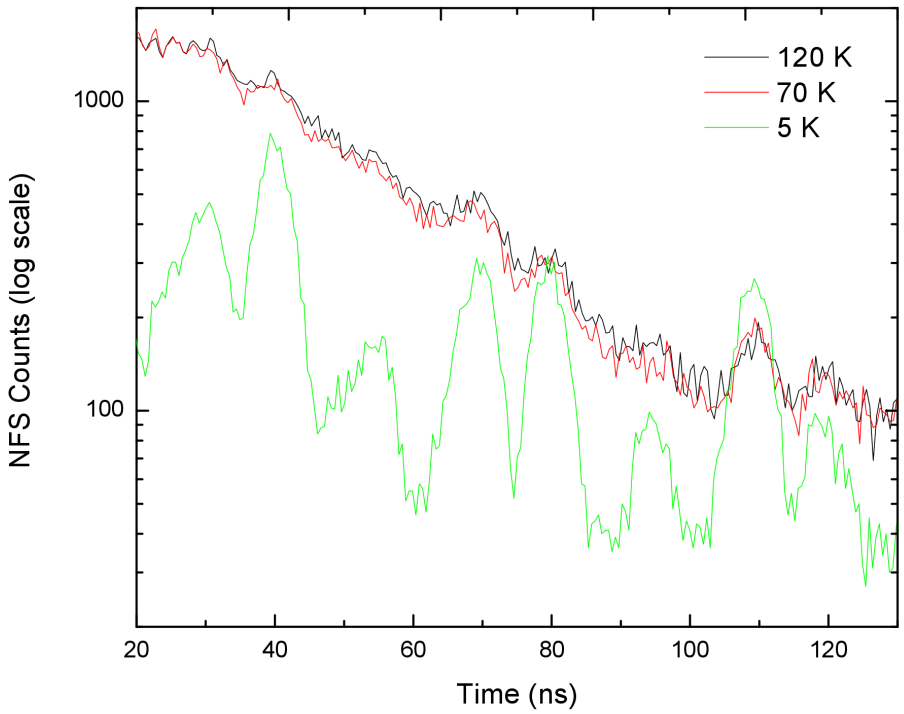

Figure 4-19 Temperature evolution of the nuclear forward scattering time spectra for non-superconducting sample grown on CaF_2 substrate.

During this experiment another interesting result was discovered. A significant reduction in the average number of nuclear forward scattering counts per second could be observed at 40 K compared to 70 K for both samples. For superconducting sample the average number of counts were reduced from 100 (at 70 K) to 10 (at 40 K). For the non-superconducting sample the average number counts were reduced from 10 (at 70 K) to 2 (at 40 K).

The reduction in nuclear forward scattering count rate can be related to a reduction in Lamb Mossbauer factor. The Lamb Mossbauer factor is defined as the recoil-free fraction to total nuclear resonance absorption in Mossbauer spectroscopy. When an ensemble of nuclei absorbs a gamma ray or synchrotron radiation of 14.4 KeV there is a probability that the nucleus can recoil back to conserve momentum. As a result, some fraction of energy of the radiation absorbed by

the nucleus can be lost. When the nucleus is in a crystal it is believed that the energy lost due to the recoil of nucleus can be a minimum since the crystal as a whole rather than a single nucleus contributes to momentum conservation. But due to the phonons interacting with nucleus there is a possibility for a recoil process that transfers energy to excite phonons. Compared to low temperatures, at room temperature the probability of exciting phonons is much higher due to the thermal energy associated with the crystal. It can be considered that the recoil free fraction during nuclear resonant absorption at room temperature is less than at low temperatures. Hence the Lamb Mossbauer factor is small at room temperature compared to low temperatures for solids in general.

But in this experiment as the temperature decreased, a significant reduction in nuclear forward scattering count rate, and hence the Lamb Mossbauer factor, could be observed indicating unusual behavior. To get more information about this behavior, the average nuclear forward scattering counts per second was carefully measured with respect to temperature for both samples. Typically during the experiment the energy of the incident radiation fluctuated from the resonant energy of 14.4 KeV over a range of several meV. Therefore the angles of the three monochromators were tuned manually in order to keep the incident energy of synchrotron radiation at resonance. To avoid this energy fluctuation issue and to get more accurate nuclear forward scattering count rate, at each temperature a scan of count rate vs energy of incident radiation was done and the area under the curve of the energy scan was calculated at each temperature for both samples.

Figure 4-21 shows the energy scan done at 100 K for superconducting $FeTeO_x$ while cooling down.

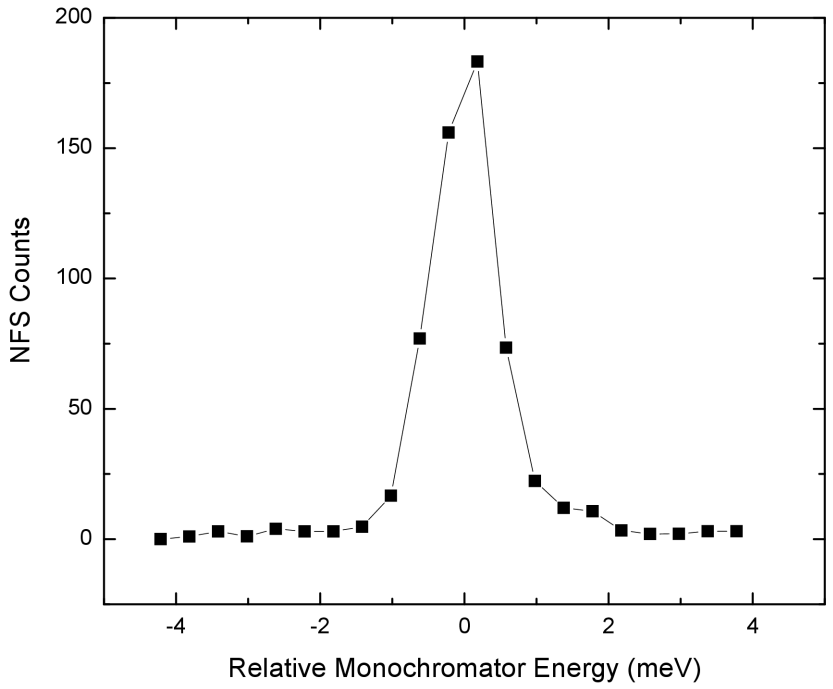

Figure 4-20 Energy scan done for superconducting $FeTeO_x$ at 100 K while cooling the sample.

Figure 4-22 shows the area of the energy scan of nuclear forward scattering counts observed with respect to temperature for the superconducting $FeTeO_x$ film grown on MgO. From 100 K to 70 K the count rate remains almost as a constant with small fluctuations. From 70 K to 50 K a distinct reduction in the count rate could be observed and below 50 K count rate remains almost as a constant. To figure out whether this effect is associated with superconductivity the nuclear forward scattering count rate was measured as a function of temperature for the non-superconducting FeTe film grown on CaF_2 substrate. Figure 4-23 shows the area of the energy scan of nuclear forward scattering counts observed with respect to temperature for the non-superconducting FeTe film grown on CaF_2.

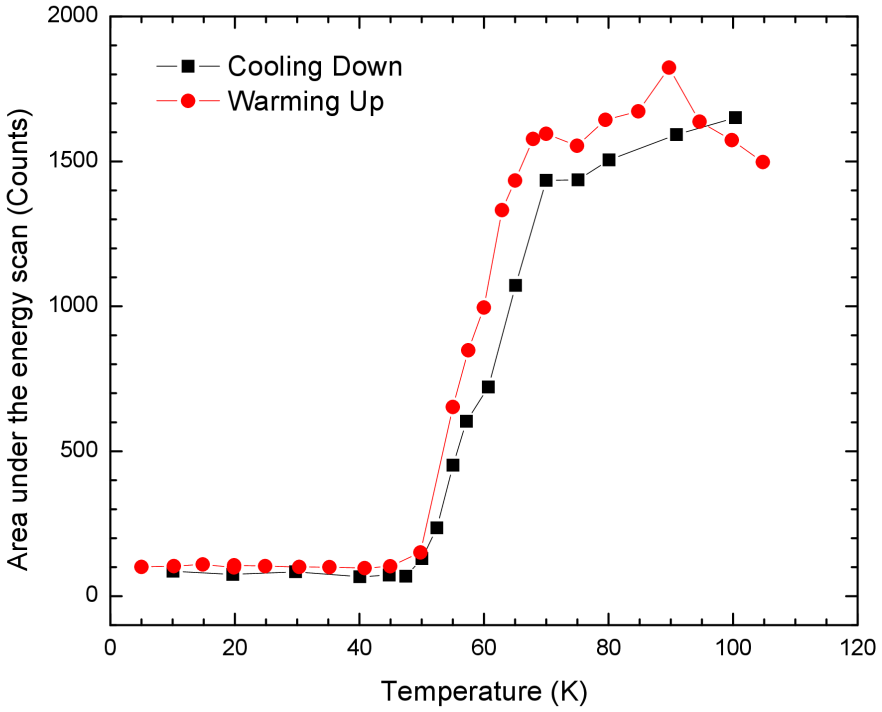

Figure 4-21 Nuclear forward scattering count rate with respect to temperature obtained for a superconducting $FeTeO_x$ film grown on MgO substrate.

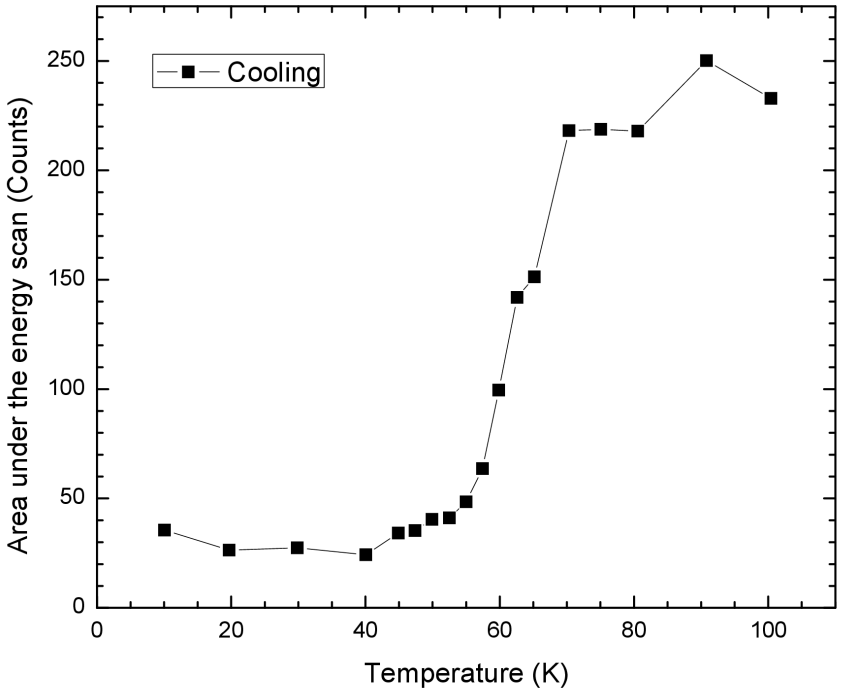

Figure 4-22 Nuclear forward scattering count rate with respect to temperature obtained for a superconducting FeTe film grown on CaF_2 substrate.

For FeTe film behavior similar to superconducting $FeTeO_x$ could be observed. A distinct reduction in the count rate could be seen at temperatures below 40 K. Since both superconducting $FeTeO_x$ and non-superconducting FeTe show a decrease in count rate at low temperature we rule out the possibility that this behavior is associated with superconductivity. At the moment the most logical explanation would be that this reduction is associated with the structural and antiferromagnetic transition, which occurs in both superconducting $FeTeO_x$ and non-superconducting FeTe. The strongest evidence that supports this is the temperature at which the change in count rate occurs. This temperature coincides with the temperature that structural and magnetic transition occurs in $FeTeO_x$/FeTe film system.

In the literature there are several reports, which describe anomalies in the temperature dependent Lamb Mossbauer factor in iron-based compounds. A decrease in the absorption area of the conventional Mossbauer spectrum, hence Lamb Mossbauer factor at the vicinity of superconducting transition has been observed in FeSe[83], $FeSe_{0.5}Te_{0.5}$[84] and LiFeAs[85]. This is related to a softening in lattice at T_c in these reports. Since these experimental data were reported in units of area covered by the conventional Mossbauer absorption spectrum or in arbitrary units, it is difficult to compare the change in area at T_c observed in these reports to the change in nuclear forward scattering counts we observed at antiferromagnetic and structural transition temperature in our samples. A sudden change in Lamb Mossbauer factor was reported in $CaFe_2As_2$ near the structural and antiferromagnetic transition.[86] This report claims that an increase in Lamb Mossbauer factor could be observed due to the magnetic and structural transition occurs in $CaFe_2As_2$ around 165 K. To compare our results with the results shown in fig. 5 of this reference (85), the graph shown in fig. 4-22 for superconducting $FeTeO_x$ was re-plotted as the negative value of logarithm of relative area of NFS counts w.r.t the area of NFS

counts at 5 K vs temperature for warming-up cycle, following a procedure described in ref. 86.[87] The resulting graph is shown in figure 4-24.

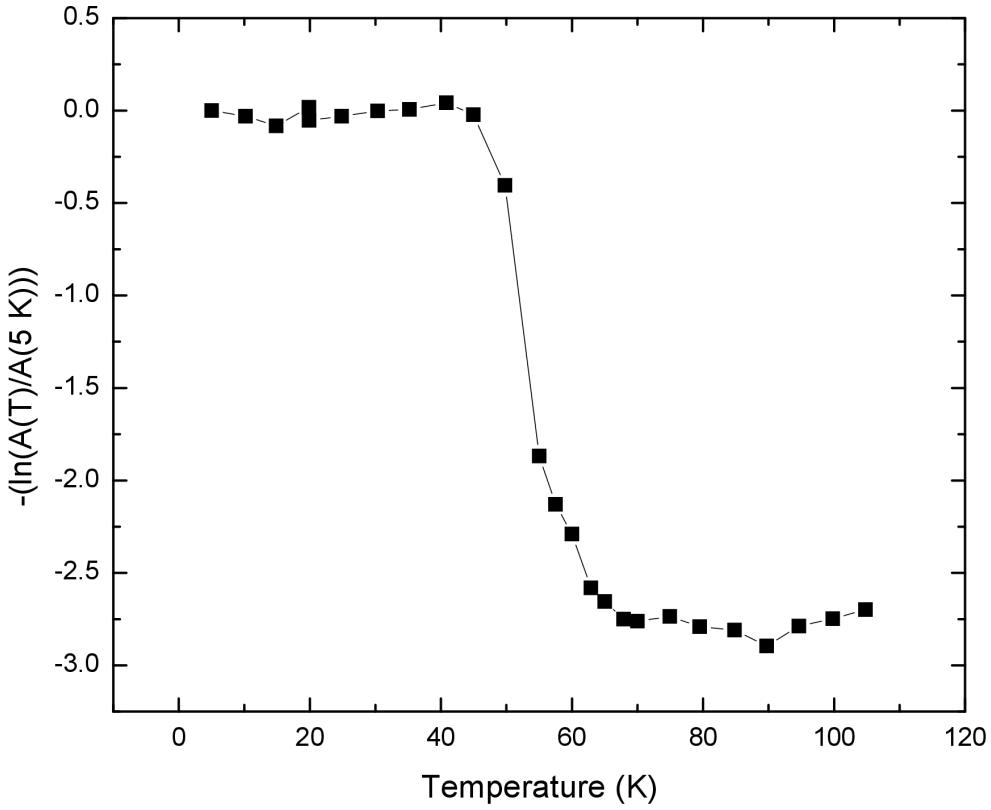

Figure 4-23 Temperature dependent nuclear forward scattering counts observed for superconducting $FeTeO_x$ represented as the negative value of logarithm of relative area of NFS counts w.r.t the area of NFS counts at 5 K.

It can be concluded that the anomaly in Lamb Mossbauer factor, observed for superconducting $FeTeO_x$ around 50 K behaves in the opposite direction compared to the effect observed for $CaFe_2As_2$ around 165 K. Due to the different techniques that had been used to do the above two experiments it is not possible to compare the magnitude of the effect between the two.

It is possible that a softening in lattice can occur in superconducting $FeTeO_x$/non-superconducting FeTe system due to the structural and magnetic transition which undergoes in these compounds around 65 K.

4.6 Conclusion

The low temperature magnetic structure of superconducting $FeTeO_x$/non-superconducting FeTe was investigated using neutron diffraction, conventional Mossbauer spectroscopy and synchrotron Mossbauer spectroscopy. From all above techniques it was revealed that both superconducting $FeTeO_x$ and non-superconducting FeTe films undergo an antiferromagnetic transition similar to parent FeTe. The neutron diffraction and conventional Mossbauer spectroscopy experiments suggest that there is a distinct reduction in magnetism at the vicinity of superconducting transition. Such a distinct reduction was not clear from the results of synchrotron Mossbauer spectroscopy that whether there exists a reduction in local magnetic fields in $FeTeO_x$ in superconducting state compared to normal state. Synchrotron Mossbauer spectroscopy doesn't show an obvious reduction in magnetism. In addition to a reduction in average ordered magnetic moment (by neutron diffraction), a reduction in local magnetic moment (by conventional Mossbauer spectroscopy) was also detected for superconducting $FeTeO_x$ at the vicinity of superconducting transition. This indicates that whole material transforms to a partial non-magnetic state rather than some portion of the material. The results from all techniques suggest that magnetism co-exists with superconductivity in superconducting $FeTeO_x$.

From the synchrotron Mossbauer spectroscopy experiment a significant reduction in nuclear forward scattering count rate, hence the Lamb Mossbauer factor could be observed around the temperature where structural and magnetic transition occurs. It is possible that a soft phonon mode can exist in superconducting $FeTeO_x$/non-superconducting FeTe system as a result of structural and magnetic transition.

5 Summary, Conclusion and Future Work

In this thesis we have described the effect of pulsed laser deposition growth parameters on superconducting $FeTeO_x$ film growth. We have also reported the low temperature crystal structure and magnetic structure of superconducting $FeTeO_x$ films. In this final chapter we will provide a summary of main discoveries we discussed for each section in this thesis and provide guidance for future work on these projects.

We introduced a new growth mode to produce $FeTeO_x$ films with better surface morphology and stable oxygen concentration. The key changes in growth parameters we found to obtain optimized quality films were, shorter target to substrate distance, high laser power and a dense polycrystalline target. Superconductivity could be obtained in $FeTeO_x$ films grown on substrates which contain oxygen (MgO, $SrTiO_3$, LAO, SLAO and LSAT) but it was very difficult to incorporate oxygen into films grown on a CaF_2 substrate. The much better surface morphology and crystallinity of the films grown on CaF_2 substrates is the major reason behind this issue. This is somewhat analogous to the difficulty which arises in incorporating oxygen into single crystalline bulk FeTe to get bulk superconductivity in this material. More understanding about the underlying chemistry about the surface layer between FeTe film and CaF_2 substrate is necessary to resolve this issue. It seems like non-uniformity in the film up to a certain degree is needed to incorporate oxygen into the FeTe lattice. Among films grown on oxide substrates, $FeTeO_x$ films grown on MgO substrate have a better crystalline quality compared to films grown on other substrates. The rotation of the FeTe lattice with respect to MgO substrate (to obtain a smaller lattice mismatch) can be the reason behind above observation.

We concluded that superconducting $FeTeO_x$ undergoes the structural transition from tetragonal to monoclinic around 65 K similar to parent FeTe. We couldn't observe any change in crystal symmetry of $FeTeO_x$ in superconducting state compared to its normal state. We saw a large change in c-axis lattice parameter (upturn and downturn) at the vicinity of superconducting transition temperature for superconducting $FeTeO_x$ but not for parent FeTe. We associated the downturn with superconductivity. Using this large change in c-axis lattice parameter and Ehrenfest relation we predicted that a compression along c-axis in $FeTeO_x$ would lead to high superconducting transition temperatures. This suggests an important interplay between lattice and superconductivity in superconducting $FeTeO_x$ system. In order to compress $FeTeO_x$ films along c-axis, very thin films can be grown on appropriate substrates such that tensile strain applies along a-b plane of the film. So far, growing very thin films of $FeTeO_x$ has been a challenge due to the formation of islanding structure. Further extensive study on the effect of different growth parameters for pulsed laser deposition on very thin film growth will be helpful in solving this issue.

Using low temperature neutron diffraction and Mossbauer experiments we concluded that superconducting $FeTeO_x$ undergoes the antiferromagnetic transition around 65 K similar to parent FeTe. Results obtained from both above techniques suggest a distinct reduction in magnetism in $FeTeO_x$ upon entering the superconducting state. Due to the uncertainty in the data sets, particularly a limited signal to noise ratio, we couldn't come to a firm conclusion about this reduction in magnetism. More experiments should be done to clarify this reduction. For conventional Mossbauer studies, the use of a more powerful gamma ray source can improve the data quality. For neutron diffraction, improvement of crystal quality of superconducting $FeTeO_x$

films and the use of a higher flux neutron source with a low background diffractometer will be helpful in obtaining more reliable data.

The temperature dependent resistance, the low temperature crystal structure and low temperature magnetic structure of superconducting $FeTeO_x$ show a remarkable similarity to the properties of parent FeTe above the superconducting transition temperature. Oxygen acts as an interesting dopant making only a small change in structure and normal state properties yet inducing superconductivity. Therefore there should be some transformation which favors superconductivity that undergoes in $FeTeO_x$ at T_c. We don't think $FeTeO_x$ has chemically phase separated regions, one superconducting and the other non-superconducting, because we didn't observe any broadening in the temperature evolution of the $FeTeO_x$ (0 0 4) structural peak. The whole material transforms to a superconductor at T_c. We speculate that there exists a magnetic to a partial non-magnetic transition at T_c which drives $FeTeO_x$ to a superconductor. The upturn in c-axis lattice parameter we observed just above T_c and the reduction in magnetism we detected near T_c lead us to above hypothesis. In superconducting $FeTeO_x$, magnetism is not completely suppressed but it co-exists with superconductivity in superconducting state. At this point, we are not clear whether magnetism favors superconductivity or whether magnetism competes with superconductivity but our observations suggest that there is a strong coupling between magnetism and superconductivity in $FeTeO_x$. Using inelastic neutron scattering, John Tranquada's group[88] reports that for superconducting $Fe_{1+y}Te_{1-x}Se_x$ system "while static magnetic order around the reciprocal lattice position (0.5, 0) competes with superconductivity, spin excitations centered around (0.5,0.5) are closely coupled to the materials'superconductivity." [88] For the superconducting $FeTeO_x$ system in addition to (1/2, 0, ½) magnetic peak it is worthwhile to study the temperature evolution of (1/2, ½, ½) magnetic peak via elastic neutron

scattering or to check for spin fluctuations of this system via inelastic neutron scattering. This study will be helpful in understanding the interplay between magnetism and superconductivity in $FeTeO_x$ system.

Using conventional Mossbauer spectroscopy studies we were able to detect two iron sites with comparable occupancy in FeTe unit cell for both superconducting $FeTeO_x$ and parent FeTe. This is inconsistent with the reported information about the crystal structure of this system determined by neutron and x-ray diffraction studies. More experiments should be done to identify the reasons behind this observation. A careful analysis of structural refinement of both FeTe and $FeTeO_x$ will be helpful in determining whether there are extra iron sites in FeTe structure, which was not identified so far or to detect any charge ordering in the system. Resonant x-ray diffraction can be also used to study any charge ordering in this system.

We could observe a significant reduction in nuclear forward scattering count rate hence the Lamb Mossbauer factor for both superconducting $FeTeO_x$ and non-superconducting FeTe around 65 K suggesting that it is possible to have a soft phonon mode coupled with the magnetic and structural transition at 65 K in this system. This observation does not directly suggest a relation between a soft phonon mode and superconductivity. But it is worthwhile to do a more careful study about the temperature evolution of Lamb Mossbauer factor paying special attention around T_c using better quality $FeTeO_x$ films. Synchrotron inelastic x-ray scattering technique can be used to identify any soft phonon mode associated with this superconducting $FeTeO_x$ / non-superconducting FeTe system.

We made an attempt to study the location of oxygen and amount of oxygen in FeTe structure using extended x-ray absorption fine structure (EXAFS). Our aim was to investigate the

EXAFS at the Fe absorption edge expecting oxygen to be the nearest neighbor. We couldn't detect any significant change in the EXAFS data of superconducting $FeTeO_x$ film compared to the data of non-superconducting FeTe film. In future studying the oxygen absorption edge of very thick $FeTeO_x$ films and the use of density functional calculations to model the x-ray absorption data at oxygen edge will be helpful in determining the local electronic structure about the oxygen and location and amount of oxygen in the FeTe structure.

The experiments we have done so far to study superconducting $FeTeO_x$ can be extended to study the $FeTe_{(1-x)}Se_xO_y$ film system. It would be interesting to explore the combined effect of both charge doping (oxygen incorporation) and isovalent substitution (Se doping) on parent FeTe. This will give new insights into understanding what critical parameter changes when a superconductor is created from parent FeTe.

References

[1] C.P. Poole Jr., F.A. Horacio, R.J. Creswick, and P. Ruslan, *Superconductivity*, Second Edi (Academic Press, Elsevier, Netherlands, 2007).

[2] Y. Kamihara, T. Watanabe, M. Hirano, and H. Hosono, J. Am. Chem. Soc. **130**, 3296 (2008).

[3] F.-C. Hsu, J.-Y. Luo, K.-W. Yeh, T.-K. Chen, T.-W. Huang, P.M. Wu, Y.-C. Lee, Y.-L. Huang, Y.-Y. Chu, D.-C. Yan, and M.-K. Wu, Proc. Natl. Acad. Sci. U. S. A. **105**, 14262 (2008).

[4] R. Zhi-An, L. Wei, Y. Jie, Y. Wei, S. Xiao-Li, C. Guang-Can, D. Xiao-Li, S. Li-Ling, Z. Fang, and Z. Zhong-Xian, Chinese Phys. Lett. **25**, 2215 (2008).

[5] J. Paglione and R.L. Greene, Nat. Phys. **6**, 645 (2010).

[6] K. Ishida, Y. Nakai, and H. Hosono, J. Phys. Soc. Japan **78**, 062001 (2009).

[7] D. Johnston, Adv. Phys. **59**, 803 (2010).

[8] E. Dagotto, Rev. Mod. Phys. **66**, 763 (1994).

[9] T.J. Liu, J. Hu, B. Qian, D. Fobes, Z.Q. Mao, W. Bao, M. Reehuis, S. a J. Kimber, K. Prokeš, S. Matas, D.N. Argyriou, a Hiess, a Rotaru, H. Pham, L. Spinu, Y. Qiu, V. Thampy, a T. Savici, J. a Rodriguez, and C. Broholm, Nat. Mater. **9**, (2010).

[10] H. Luetkens, H.-H. Klauss, M. Kraken, F.J. Litterst, T. Dellmann, R. Klingeler, C. Hess, R. Khasanov, a Amato, C. Baines, M. Kosmala, O.J. Schumann, M. Braden, J. Hamann-Borrero, N. Leps, a Kondrat, G. Behr, J. Werner, and B. Büchner, Nat. Mater. **8**, 305 (2009).

[11] P. Canfield, S. Bud'ko, N. Ni, J. Yan, and a. Kracher, Phys. Rev. B **80**, 060501 (2009).

[12] K. Sasmal, B. Lv, B. Lorenz, A.M. Guloy, F. Chen, Y.-Y. Xue, and C.-W. Chu, Phys. Rev. Lett. **101**, 107007 (2008).

[13] J.H. Tapp, Z. Tang, B. Lv, K. Sasmal, B. Lorenz, P.C.W. Chu, and A.M. Guloy, Phys. Rev. B **78**, 3 (2008).

[14] S. Jiang, H. Xing, G. Xuan, C. Wang, Z. Ren, C. Feng, J. Dai, Z. Xu, and G. Cao, J. Phys. Condens. Matter **21**, 382203 (2009).

[15] M.H. Fang, H.M. Pham, B. Qian, T.J. Liu, E.K. Vehstedt, Y. Liu, L. Spinu, and Z.Q. Mao, Phys. Rev. B **78**, 224503 (2008).

[16] C. de la Cruz, Q. Huang, J.W. Lynn, J. Li, W. Ratcliff, J.L. Zarestky, H. a Mook, G.F. Chen, J.L. Luo, N.L. Wang, and P. Dai, Nature **453**, 899 (2008).

[17] C. Day, Phys. Today **August**, 36 (2009).

[18] a J. Drew, C. Niedermayer, P.J. Baker, F.L. Pratt, S.J. Blundell, T. Lancaster, R.H. Liu, G. Wu, X.H. Chen, I. Watanabe, V.K. Malik, a Dubroka, M. Rössle, K.W. Kim, C. Baines, and C. Bernhard, Nat. Mater. **8**, 310 (2009).

[19] W. Si, S.J. Han, X. Shi, S.N. Ehrlich, J. Jaroszynski, A. Goyal, and Q. Li, Nat. Commun. **4**, 1347 (2013).

[20] Y. Mizuguchi, F. Tomioka, S. Tsuda, T. Yamaguchi, and Y. Takano, Appl. Phys. Lett. **94**, 012503 (2009).

[21] Y.F. Nie, D. Telesca, J.I. Budnick, B. Sinkovic, and B.O. Wells, Phys. Rev. B **82**, 020508(R) (2010).

[22] W. Si, Q. Jie, L. Wu, J. Zhou, G. Gu, P.D. Johnson, and Q. Li, Phys. Rev. B **81**, 092506 (2010).

[23] W. Bao, Y. Qiu, Q. Huang, M.A. Green, P. Zajdel, M.R. Fitzsimmons, M. Zhernenkov, S. Chang, M. Fang, B. Qian, E.K. Vehstedt, J. Yang, H.M. Pham, L. Spinu, and Z.Q. Mao, Phys. Rev. Lett. **102**, 247001 (2009).

[24] S. Li, C. de la Cruz, Q. Huang, Y. Chen, J.W. Lynn, J. Hu, Y.-L. Huang, F.-C. Hsu, K.-W. Yeh, M.-K. Wu, and P. Dai, Phys. Rev. B **79**, 054503 (2009).

[25] S. Margadonna, Y. Takabayashi, M.T. McDonald, K. Kasperkiewicz, Y. Mizuguchi, Y. Takano, A.N. Fitch, E. Suard, and K. Prassides, Chem. Commun. (Camb). 5607 (2008).

[26] T. McQueen, A. Williams, P. Stephens, J. Tao, Y. Zhu, V. Ksenofontov, F. Casper, C. Felser, and R. Cava, Phys. Rev. Lett. **103**, 057002 (2009).

[27] Y. Mizuguchi, F. Tomioka, S. Tsuda, T. Yamaguchi, and Y. Takano, Appl. Phys. Lett. **93**, 152505 (2008).

[28] S. Margadonna, Y. Takabayashi, Y. Ohishi, Y. Mizuguchi, Y. Takano, T. Kagayama, T. Nakagawa, M. Takata, and K. Prassides, Phys. Rev. B **80**, 064506 (2009).

[29] S. Medvedev, T.M. McQueen, I. a Troyan, T. Palasyuk, M.I. Eremets, R.J. Cava, S. Naghavi, F. Casper, V. Ksenofontov, G. Wortmann, and C. Felser, Nat. Mater. **8**, 630 (2009).

[30] K. Horigane, N. Takeshita, C.-H. Lee, H. Hiraka, and K. Yamada, J. Phys. Soc. Japan **78**, 063705 (2009).

[31] N.C. Gresty, Y. Takabayashi, A.Y. Ganin, M.T. McDonald, J.B. Claridge, D. Giap, Y. Mizuguchi, Y. Takano, T. Kagayama, Y. Ohishi, M. Takata, M.J. Rosseinsky, S. Margadonna, and K. Prassides, J. Am. Chem. Soc. **131**, 16944 (2009).

[32] Y. Mizuguchi and Y. Takano, J. Phys. Soc. Japan **79**, 102001 (2010).

[33] Y. Han, W.Y. Li, L.X. Cao, X.Y. Wang, B. Xu, B.R. Zhao, Y.Q. Guo, and J.L. Yang, Phys. Rev. Lett. **104**, 017003 (2010).

[34] D. Telesca, Y. Nie, J.I. Budnick, B.O. Wells, and B. Sinkovic, Phys. Rev. B **85**, 214517 (2012).

[35] I.W. Boyd, Ceram. Int. **22**, 429 (1996).

[36] H.-U. Krebs, M. Weisheit, J. Faupel, E. Suske, T. Scharf, C. Fuhse, M. Stormer, K. Sturm, M. Seibt, H. Kijewski, D. Nelke, E. Panchenko, and M. Buback, Adv. Solid State Phys. **43**, 505 (2003).

[37] M. Frumar, B. Frumarova, P. Nemec, T. Wagner, J. Jedelsky, and M. Hrdlicka, J. Non. Cryst. Solids **352**, 544 (2006).

[38] D.P. Norton, Annu. Rev. Mater. Sci. **28**, 299 (1998).

[39] Z.T. Zhang, Z.R. Yang, W.J. Lu, X.L. Chen, L. Li, Y.P. Sun, C.Y. Xi, L.S. Ling, C.J. Zhang, L. Pi, M.L. Tian, and Y.H. Zhang, Phys. Rev. B **88**, 214511 (2013).

[40] I. Tsukada, M. Hanawa, T. Akiike, F. Nabeshima, Y. Imai, A. Ichinose, S. Komiya, T. Hikage, T. Kawaguchi, H. Ikuta, and A. Maeda, Appl. Phys. Express **4**, 053101 (2011).

[41] M. Zheng, H. Hu, C. Zhang, B. Mulcahy, J. Zuo, and J. Eckstein, arXiv:1301.4696 (unpublished) (2013).

[42] J.W. Lynn and P. Dai, Phys. C Supercond. **469**, 469 (2009).

[43] J. Zhao, W. Ratcliff, J.W. Lynn, G.F. Chen, J.L. Luo, N.L. Wang, J. Hu, and P. Dai, Phys. Rev. B **78**, 140504 (2008).

[44] T. Nomura, S.W. Kim, Y. Kamihara, M. Hirano, P. V Sushko, K. Kato, M. Takata, a L. Shluger, and H. Hosono, Supercond. Sci. Technol. **21**, 125028 (2008).

[45] a. Goldman, D. Argyriou, B. Ouladdiaf, T. Chatterji, a. Kreyssig, S. Nandi, N. Ni, S. Bud'ko, P. Canfield, and R. McQueeney, Phys. Rev. B **78**, 100506 (2008).

[46] Y. Su, P. Link, a. Schneidewind, T. Wolf, P. Adelmann, Y. Xiao, M. Meven, R. Mittal, M. Rotter, D. Johrendt, T. Brueckel, and M. Loewenhaupt, Phys. Rev. B **79**, 064504 (2009).

[47] M. Rotter, M. Pangerl, M. Tegel, and D. Johrendt, Angew. Chem. Int. Ed. Engl. **47**, 7949 (2008).

[48] J. Zhao, Q. Huang, C. de la Cruz, S. Li, J.W. Lynn, Y. Chen, M. a Green, G.F. Chen, G. Li, Z. Li, J.L. Luo, N.L. Wang, and P. Dai, Nat. Mater. **7**, 953 (2008).

[49] N. Ni, M.E. Tillman, J.-Q. Yan, a. Kracher, S.T. Hannahs, S.L. Bud'ko, and P.C. Canfield, Phys. Rev. B **78**, 1 (2008).

[50] S. Nandi, M.G. Kim, a. Kreyssig, R.M. Fernandes, D.K. Pratt, a. Thaler, N. Ni, S.L. Bud'ko, P.C. Canfield, J. Schmalian, R.J. McQueeney, and a. I. Goldman, Phys. Rev. Lett. **104**, 1 (2010).

[51] S. Margadonna, Y. Takabayashi, M. McDonald, M. Brunelli, G. Wu, R. Liu, X. Chen, and K. Prassides, Phys. Rev. B **79**, 1 (2009).

[52] R. Khasanov, M. Bendele, A. Amato, P. Babkevich, A.T. Boothroyd, A. Cervellino, K. Conder, S.N. Gvasaliya, H. Keller, H.-H. Klauss, H. Luetkens, V. Pomjakushin, E. Pomjakushina, and B. Roessli, Phys. Rev. B **80**, 140511(R) (2009).

[53] Y.F. Nie, D. Telesca, J.I. Budnick, B. Sinkovic, R. Ramprasad, and B.O. Wells, J. Phys. Chem. Solids **72**, 426 (2011).

[54] S. Bud'ko, P. Canfield, a. Sefat, B. Sales, M. McGuire, and D. Mandrus, Phys. Rev. B **80**, 134523 (2009).

[55] F. Hardy, P. Adelmann, T. Wolf, H. v. Löhneysen, and C. Meingast, Phys. Rev. Lett. **102**, 187004 (2009).

[56] S. Bud'ko, N. Ni, S. Nandi, G. Schmiedeshoff, and P. Canfield, Phys. Rev. B **79**, 054525 (2009).

[57] M. da Luz, J. Neumeier, R. Bollinger, a. Sefat, M. McGuire, R. Jin, B. Sales, and D. Mandrus, Phys. Rev. B **79**, 214505 (2009).

[58] S.L. Bud'ko, Y. Liu, T. a. Lograsso, and P.C. Canfield, Phys. Rev. B **86**, 224514 (2012).

[59] C. Meingast, in *Handb. Supercond. Mater. Charact. Appl. Cryog. Vol. 2*, edited by D. Cardwell and D. Ginley (Institute of Physics Publishing, London, 2003), p. 1513.

[60] Y. Xiao, Y. Su, C.M.N. Kumar, C. Ritter, R. Mittal, S. Price, J. Perßon, and T. Brückel, Eur. Phys. J. B **82**, 113 (2011).

[61] S.L. Bud'ko, N. Ni, and P.C. Canfield, Phys. Rev. B **79**, 220516(R) (2009).

[62] J.S. Kim, G.R. Stewart, S. Kasahara, T. Shibauchi, T. Terashima, and Y. Matsuda, J. Phys. Condens. Matter **23**, 222201 (2011).

[63] V. Tsurkan, J. Deisenhofer, a. Günther, C. Kant, M. Klemm, H. -a. Krug von Nidda, F. Schrettle, and a. Loidl, Eur. Phys. J. B **79**, 289 (2011).

[64] J. Locquet, J. Perret, J. Fompeyrine, and E. Mächler, Nature **394**, 453 (1998).

[65] F.E. Fujita, U. Gonser, R.W. Grant, P. Gutlich, S.S. Hafner, and C.E. Johnson, *Mossbauer Spectroscopy*, First Edit (Springer-Verlag New York Heidelberg Berlin, 1975).

[66] H.H. Hamdeh, M.M. El-Tabey, R. Asmatulu, J.C. Ho, T.W. Huang, K.W. Yeh, and M.K. Wu, EPL (Europhysics Lett. **89**, 67009 (2010).

[67] V. Ksenofontov, G. Wortmann, S. Medvedev, V. Tsurkan, J. Deisenhofer, A. Loidl, and C. Felser, Phys. Rev. B **84**, 180508 (2011).

[68] Y. Mizuguchi, T. Furubayashi, K. Deguchi, S. Tsuda, T. Yamaguchi, and Y. Takano, Phys. C Supercond. **470**, S338 (2010).

[69] D. Ryan, http://www.physics.mcgill.ca/~dominic/lab/fe57moss.html (n.d.).

[70] Hokur, http://en.wikipedia.org/wiki/M%C3%B6ssbauer_spectroscopy (n.d.).

[71] P.A. de Souza, Lab. Robot. Autom. **11**, 3 (1999).

[72] J.B. Hastings, D.P. Siddons, U. van Burck, R. Hollatz, and U. Bergmann, Phys. Rev. Lett. **66**, 770 (1991).

[73] G.V. Smirnov, Hyperfine Interact. **97/98**, 551 (1996).

[74] Y.-L. Chen and D.-P. Yang, in *Mossbauer Eff. Lattice Dyn. Exp. Tech. Appl.* (John Wiley & Sons, 2007), pp. 253–304.

[75] H. Grunsteudel, V. Rusanov, H. Winkler, W. Meyer-Klaucke, and A.X. Trautwein, Hyperfine Interact. **122**, 345 (1999).

[76] N. Planckaert, R. Callens, J. Demeter, B. Laenens, J. Meersschaut, W. Sturhahn, S. Kharlamova, K. Temst, and a. Vantomme, Appl. Phys. Lett. **94**, 224104 (2009).

[77] E.E. Alp, W. Sturhahn, and T.S. Toellner, Hyperfine Interact. **135**, 295 (2001).

[78] E.E. Alp, W. Sturhahn, T.S. Toellner, J. Zhao, and B.M. Leu, in *Rudolf Mössbauer Story His Sci. Work Its Impact Sci. Hist.*, edited by M. Kalvius and P. Kienle (Springer-Verlag Berlin Heidelberg, 2012), pp. 339–358.

[79] W. Sturhahn, J. Phys. Condens. Matter **16**, S497 (2004).

[80] R. Viennois, E. Giannini, D. van der Marel, and R. Černý, J. Solid State Chem. **183**, 769 (2010).

[81] A. Sklyarova, J. Lindén, E.-L. Rautama, and M. Karppinen, J. Magn. Magn. Mater. **329**, 129 (2013).

[82] A. Błachowski, K. Ruebenbauer, P. Zajdel, E.E. Rodriguez, and M.A. Green, J. Phys. Condens. Matter **24**, 386006 (2012).

[83] J.K.M. Lindén, E.-L. Rautama, M. Karppinen, and H. Yamauchi, Hyperfine Interact. **208**, 133 (2012).

[84] J. Lindén, J.-P. Libäck, M. Karppinen, E.-L. Rautama, and H. Yamauchi, Solid State Commun. **151**, 130 (2011).

[85] W.B. Gao, J. Lindén, X.C. Wang, C.Q. Jin, T. Tohyama, M. Karppinen, and H. Yamauchi, Solid State Commun. **150**, 1525 (2010).

[86] Z. Li, X. Ma, H. Pang, and F. Li, J. Phys. Condens. Matter **23**, 255701 (2011).

[87] K. Sharma, V.R. Reddy, A. Gupta, S.D. Kaushik, and V. Siruguri, J. Phys. Condens. Matter **24**, 376001 (2012).

[88] J. Wen, G. Xu, G. Gu, J.M. Tranquada, and R.J. Birgeneau, Reports Prog. Phys. **74**, 124503 (2011).